APPLICATIONS OF SPECTRAL MANAGEMENT IN OPTOELECTRONIC DEVICES

Nathaniel J. L. K. Davis

St John's College

Optoelectronics Group

Cavendish Laboratory - Department of Physics

University of Cambridge

This dissertation is submitted for the degree of Doctor of Philosophy

March 2017

To my family and friends.

“If you only do what you can do, you'll never be more than what you are now”

Master Shifu – Kung Fu Panda 3

DECLARATION

This dissertation is the result of my own work and includes nothing which is the outcome of work done in collaboration except where specifically indicated in the text. The use of the first person plural is strictly a matter of style. It has not been previously submitted, in part or whole, to any university of institution for any degree, diploma, or other qualification.

In accordance with the Department of Physics guidelines, this thesis does not exceed 60,000 words.

Signed:____

Date:____

Nathaniel J. L. K. Davis B.Sc. (Adv) Hons H1M

Cambridge

ABSTRACT

The application and efficiency of optoelectronic devices depends on the ability to control the absorption and emission processes of photons in semiconductors. This thesis looks at three different applications of spectral management across a broad range of optoelectronic devices: photovoltaics (PVs), luminescent solar concentrators (LSCs) and light-emitting diodes (LEDs).

Multiple excitation generation (MEG) – a process in which multiple charge-carrier pairs are generated from a single optical excitation - is a promising way to improve the photocurrent in photovoltaic devices and offers the potential to break the Shockley-Queisser limit. Here we present solar cells fabricated from PbSe nanorods which show external quantum efficiencies exceeding 100 %. This demonstrates the potential for substantial improvements in PV device performance due to MEG.

Through spatial and spectral concentration, LSCs have the potential to reduce the cost of photovoltaic energy production and are attractive prospects for photobioreactors and building-integrated applications. Here we introduce versatile star-shaped donor-acceptor molecules based on a central BODIPY acceptor with oligofluorene donor side units. We perform comprehensive device measurements and Monte Carlo ray tracing simulations of LSCs. We find that the measured structures permit waveguide propagation lengths on a par with state-of-the-art nanocrystalline emitters, while proposed hypothetical structures can be seen as viable candidates for photobioreactor and energy production roles and should be synthesized.

The efficiency of nanocrystal-based LEDs is inherently limited by the types of crystals used. Cesium lead halide perovskite nanocrystals exhibit photoluminescence quantum efficiencies approaching 100%. However, due to the large surface areas and anion mobility halogen exchange between perovskite nanocrystals of different compositions occurs rapidly, limiting applications. Here, we report significantly reduced halide exchange between chloride and iodide $CsPbX_3$ (X= Cl, I) perovskite nanocrystals. We investigate perovskite-based multi-crystal component samples and their resulting optical and electrical interactions in bulk heterojunction LEDs. Efficient photon reabsorption from $CsPbCl_3$ to $CsPbI_3$ nanocrystals was found to improve LED device performance.

ACKNOWLEDGEMENTS

I would firstly like to thank my supervisor Professor Neil Greenham for providing material resources, ideas, feedback, support and teaching throughout what has been a thoroughly enjoyable time.

Many thanks go to all my collaborators and their helpful discussions, practical training and, in some instances, direct assistance: Professor Peter Skabara, Dr. Dan Credgington, Dr. Caterina Ducati, Dr. Marcus Böhm, Dr. Felix Deschler, Dr. Bruno Ehrler, Dr. James Griffiths, Dr. Rowan MacQueen, Dr. Matt Menke, Dr. Rupert Taylor, Dr. Francisco de la Peña Manchon, Mr. Edward Booker, Mr. Tom Jellicoe, Mr. Robin Lamboll, Mr. Johannes Richter, Mr. Saul Jones, Mr. Maxim Tabachnyk, Mrs. Florencia Wisnivesky-Rocca-Rivarola and Mr. James Xiao. My research would not have gone nearly as smoothly without the members of these research groups, whose immense help cannot be overstated.

I thank the Cambridge Australian Scholarships, The Cambridge Commonwealth European and International Trust and Mr. Charles K Allen for the Cambridge Australia Bragg Scholarship, without which I wouldn't be here.

On a personal note, I would like to thank my friends in the Optoelectronics group, St John’s College and Cambridge for their encouragement and friendship. My Ph.D. would have been far more stressful and much less productive without the calm and measured support that I received from these people.

Most of all, I thank my family (Mum, Dad, Amanda, Wacky, Eben, Kirsten, Rosalind, Hera and Quinn) and my friends back in Australia for their unending support.

CONTENTS

LIST OF ABBREVIATIONS

1,2-Ethanedithiol	EDT
1,3-benzene dithiol	BDT
Acceptor	A
Acceptor concentration	C_A
Activation threshold	$\hbar\omega_{th}$
Atomic force microscopy	AFM
Auger recombination	AR
Avogadro's number	N_A
Bandgap	Eg
Bis(diethylamido)phosphorous acid	BDPA
Bohr exciton radius	αB
Boron-dipyrromethene	BODIPY
Charge transport layer	CTL
Colloidal quantum dot	CQD
Conduction band	CB
Copper indium gallium selenide	CIGS
Current	I
Current density	J
Current maximum	Jm
Depletion region	WD
Diffusion voltage	VD
Donor concentration	C_D
Excited acceptor	A*

Excited sensitizer	S*
Energy dispersive X-ray	EDX
Energies of photoexcited electron	E_e
Energies of photoexcited hole	E_h
Effective mass of electron	m_e
Effective mass of hole	m_e
Efficiency	η
Effective mass approximation	EMA
Electron	e
Electron energy loss spectroscopy	EELS
Electron-hole pair creation energy	$\varepsilon_{\mathrm{eh}}$
Ethylene glycol dimethacrylate	EGDM
External quantum efficiency	EQE
Fermi energy	E_F
Fill factor	*FF*
Flux gain	F
Förster radius	R_0
Förster resonance energy transfer	FRET
Geometric ratio	*G*
High angle annular dark field	HAADF
Highest occupied molecular orbital	HOMO
High resolution transmission electron microscopy	HRTEM
Hole	*h*
Impact ionization	II

Incident photon energy	$\hbar\omega$
Indium tin oxide	ITO
Internal quantum efficiency	IQE
Lauryl methacrylate	LMA
Light-emitting diode	LED
Lowest un-occupied molecular orbital	LUMO
Luminescent solar concentrator	LSC
Methylammonium	MA
Multiple exciton generation	MEG
Nanocrystal	NC
Nanocrystal diameter	D
Nanocrystal length	L
Nanorod	NR
Nanorod aspect ratio	ρ
Nanowire	NW
Near infrared	NIR
Octadecene	ODE
Oleic acid	OA
Oligofluorene-BODIPY molecules	OFBM
Open circuit voltage	V_{oc}
Optical power emitted from the active region of a light-emitting diode	P_{int}
Overall power efficiency of a light-emitting diode	η_{int}
Photo-luminescent quantum efficiency	PLQE
Photovoltaics	PV

Principal component analysis	PCA
Principal quantum number	n
Poly(3,4-ethylenedioxythiophene) polystyrene sulfonate	PEDOT:PSS
Polyhedral oligomeric silsesquioxane	POSS
Polymethylmethacrylate	PMMA
Polyvinylcarbazole	PVK
Poly crystalline silicon	c-Si
Power	P
Power conversion efficiency	PCE
Power efficiency of the cell	η_{PV}
Power efficiency of the concentrator	η_{LSC}
Power density	P_s
Quantum dot	QD
Quantum dot light-emitting diode	QD-LED
Quantum efficiency	QE
Quantum yield	QY
Rate constant for cooling	k_{cool}
Rate constant for multiple exciton generation	k_{MEG}
Refractive index	n
Renewable Energy Policy Networks for the 21st Century	REN21
Sensitizer	S
Scanning transmission electron microscopy	STEM
Short circuit current	J_{sc}
Silicon drift detectors	SDD

Source measure unit	SMU
Spherical angle of the light emitted by the solar cell	Ω_{sun}
Spherical angle of the light absorbed by the solar cell	Ω_{emit}
Tetrachloroethylene	TCE
Tetradecylphosphonic acid	TDPA
Time correlated single photon counting	TCSPC
Tris(diethylamino)phosphine	TDP
Trioctylphosphine	TOP
Transmission electron microscopy	TEM
Ultraviolet	UV
Ultraviolet photoelectron spectroscopy	UPS
Valence band	VB
Voltage	V
Voltage maximum	Vm
X-ray diffraction	XRD
X-ray photoelectron spectrometer	XPS

LIST OF PUBLICATIONS SUBMITTED DURING DEGREE

- **Nathaniel J. L. K. Davis**, Marcus L. Böhm, Maxim Tabachnyk, Florencia Wisnivesky-Rocca-Rivarola, Tom C. Jellicoe, Caterina Ducati, Bruno Ehrler and Neil C. Greenham, Multiple Exciton Generation in Lead Selenide Nanorod Solar Cells with External Quantum Efficiencies Exceeding 120%, Nat. Comm. 2015, 6, 8259.
- **Nathaniel J. L. K. Davis**, Rowan W. MacQueen, Derrick A. Roberts, Sabrina Dehn, Sébastien Perrier and Timothy W. Schmidt, Energy Transfer in Pendant Perylene Diimide Copolymers , J. Mat. Chem. C.2016, 4, 8270-8275.
- **Nathaniel J. L. K. Davis**, Francisco de la Peña Manchon, Maxim Tabachnyk, Johannes Richter, Robin D. Lamboll, Edward P. Booker, Florencia Wisnivesky-Rocca-Rivarola, James T. Griffiths, Caterina Ducati, S. Mathew Menke, Felix Deschler and Neil Greenham. Photon reabsorption in mixed CsPbCl3:CsPbI3 perovskite nanocrystal films for light-emitting diodes, J. Phys. Chem. C, 2017, 121 (7), 3790–3796.
- **Nathaniel J. L. K. Davis**, Rowan MacQueen, Saul T. E. Jones, Clara Orofino, Diego Cortizo-Lacalle, Rupert Taylor, Dan Credgington, Peter J Skabara and Neil Greenham. Star shaped oligomers to minimize reabsorption losses in luminescent solar concentrators, J. Mater. Chem. C, 2017,5, 1952-1962
- Guangru Li, Florencia Wisnivesky Rocca Rivarola, **Nathaniel J. L. K. Davis**, Sai Bai, Tom C. Jellico, Shaocong Hou, Francisco de la Peña, Caterina Ducati, Feng Gao, Richard H. Friend, Neil C. Greenham and Zhi-Kuang Tan, Highly-Efficient Perovskite Nanocrystal Light-emitting Diodes Enabled By Universal Cross-Linking Method, Advanced Materials, 2015, 28, 3528-3534 .
- Claire L. Armstrong, Michael B. Price, David Muñoz-Rojas**, Nathaniel J. K. L. Davis**, Mojtaba Abdi-Jalebi, Richard H. Friend, Neil C. Greenham, Judith L. MacManus-Driscoll, Marcus L. Böhm and Kevin P. Musselman, The influence of an inorganic interlayer on exciton separation in hybrid solar cells, ACS Nano, 2015, 9 (12), 11863–11871
- Marcus L. Böhm, Tom C. Jellicoe, Jasmine P.H. Rivett, Aditya Sadhanala, **Nathaniel J.L.K. Davis**, Frederik S.F. Morgenstern, Karl C. Gödel, Jayamurugan Govindasamy, Callum G.M. Benson, Neil C. Greenham and Bruno Ehrler, Size and Energy Level Tuning of Quantum Dot Solids via a Hybrid Ligand Complex, J. Phys. Chem. Lett 2015, 6(17), 3510 - 3514.
- Marcus L. Boehm , Tom Jellicoe , Maxim Tabachnyk, **Nathaniel J. L. K. Davis**, Florencia Wisnivesky Rocca Rivarola , Caterina Ducati, Bruno Ehrler, Artem Bakulin and Neil C. Greenham, Lead Telluride Quantum Dot Solar Cells Displaying External Quantum Efficiencies Exceeding 120%, Nano. Lett. 2015, 15 (12), pp 7987–7993.
- Florencia Wisnivesky-Rocca-Rivarola, **Nathaniel J. L. K. Davis**, Marcus L. Bohm and Caterina Ducati, Morphological and Compositional (S) TEM Analysis of Multiple Exciton Generation Solar Cells, 2015, Journal of Physics: Conference Series, 644 (1), 012025

1 INTRODUCTION

1.1 Renewable and Sustainable Energy

Recently there has been an increasing demand for affordable and sustainable sources of renewable energy. This drive stems not only from the finite supply of fossil fuels, but also through an increased public awareness of the global effects arising from the use of such energy sources[1]. This shift in energy investment can be seen by looking at the Renewable Energy Policy Networks for the 21st Century (REN21) 2016 global status report on renewable energy, which shows that in 2015 renewable and sustainable sources of energy accounted for approximately 20% of the global energy capacity[2]. The aspects of the natural environment that can be exploited as renewable energy sources are diverse, with notable examples including wind, wave, tidal, biomass and photovoltaics (PV). The potential size of the energy production attributed to renewable energy is large and it has been predicted that they could exceed current and future world energy needs[3]. Out of the current renewable energy sources under development, it is the PV industry that appears to offer the greatest potential for long term cost reduction through market growth and innovation over the next 10-20 years[2,3].

1.2 Photovoltaics

One of the main driving forces for the potential of the PV market is the quantity of solar energy incident on the Earth's surface. The U.S. Energy Information Administration's International Energy Outlook 2011 states that the world's average power consumption in 2008 was 16.8 TW[4]. The sun radiates about 120000 TW of power to the planet's surface[5]; this far exceeds not only our current, but also predicted rates of future energy consumption. The main problem faced is how to draw substantial energy from this source in a cost-effective manner.

The demand for PV technology has increased by an average of 30% per annum over the past two decades, and PV continues to be the world's fastest growing power-generation technology[6]. There has been a parallel decline in PV manufacturing cost per installed watt due to economies of scale in the growing industry[7]. Consumer demand for PV technology is driven by many factors including incentive programs led by governments, local electricity tariffs, and consumer enthusiasm for renewable energy[6]. Even so, global energy production attributed to solar energy is only estimated at 274 GW, ≈ 2% of the estimated total global power consumption in 2015[2]. For PV to become a viable source of renewable energy, a decrease in not only the cost per watt of the PV module but also installation cost is required such that it can be deployed on a much larger, global scale. This decrease in cost per watt could come from improvements to solar cell efficiencies however PV cells are starting to approach the Shockley-Quiesser limit[8,9]. To further improve PV power conversion efficiencies new generation PV cells that can surpass the 32% Shockley-Queisser limit for single bandgap cells set are required[9]. New PV technology with the potential to beat the Shockley-Queisser limit include multiple exciton generation, intermediate-band cells, hot carrier cells and spectrum management technologies (up-, down-conversion)[10].

1.3 Luminescent Solar Concentrators

Research and development into PV technologies has been driven by the attempts to attain higher conversion efficiencies at lower costs. Currently widespread deployment of PV technology is still expensive and generally needs to be coupled to financial support schemes to enable installation[11,12]. It has been calculated that buildings account for about 40% of the total energy use, 70% of total electricity use and 40% of greenhouse emissions in economically-developed countries[13]. In total buildings account for about 25% of energy use globally[14]. The European commission has decreed that all new buildings be near-zero-energy by 2020[14]. If we are to bring solar energy systems to the built environment we need a PV technology specifically suited for small scale distribution. Luminescent solar concentrators (LSCs) are plastic or glass devices with luminescent species embedded within them; they absorb light through the top surface and concentrate it to the edges[15]. LSCs were developed as an alternative approach to lowering the cost of PV energy production. Light is concentrated without the need for expensive tracking, allowing small area PV devices and the option of using more expensive semiconductors becomes viable[12]. This not only reduces the cost and size of the overall PV cell but also the weight of the module. LSCs also allow color tuning for use as windows or colored plates. LSCs absorb diffuse and scattered light making them ideal for built-up environments where the light is reflected off large objects such as building and trees[13,15].

1.4 Light-Emitting Diodes

Even without looking at new ways to generate electricity, a major decrease in use of electricity can decrease the overall need for energy sources. Lighting is one of the largest uses of energy in today’s society[16]. It is reported that 1.7 billion people living in developed countries do not have access to electrical lighting[17]. These people rely on oil lamps, which are expensive, inefficient, hazardous and contribute to the release of greenhouse gases[16]. Electrical lighting is more efficient and safe compared to oil-based lighting. That said, around 33% of our total electricity produced is attributed to lighting systems. This is because the majority of lighting systems are inefficient; such as tungsten filament bulbs (≈5% efficient) and fluorescent lamps (≈25% efficient)[16,18.]

Power savings can now be achieved through solid-state lighting in the form of light-emitting diodes (LEDs). This technology promises superior attributes such as longer lifespans, and higher energy power conversion efficiencies[19]. In general, LEDs are extremely thin, light-weight and cheap, and can vary in shape and color. New lighting sources for developing countries can lead to economical improvements, as effective lighting extends the number of commercial/productive hours in a day. Also, efficient lighting sources such as solid state lighting can dramatically reduce the global electricity energy consumption by nearly 50%[19].

1.5 Spectral Management in Optoelectronics

The application and efficiency of optoelectronic devices depends on the ability to efficiently harness the energy and photons of the electromagnetic spectrum, particularly that of the near ultraviolet, visible and infrared regions. Whether it is the absorption or emission of photons, improvements to current optoelectronic devices can be made through improvements to the way the solar spectrum and emitted photons are managed. This thesis looks at three different application of spectral management across a broad range of optoelectronic devices: PVs, LSCs and LEDs.

Following a chapter on the theoretical background information of the discussed work, three results chapters and a conclusion chapter are presented. The experimental methods associated with each results chapter are included at the beginning of each results chapter. A more detailed structure of this thesis is as follows:

1.5.1 Chapter 2: Background

Chapter 2 describes the theoretical framework and relevant background necessary to understand the physics and chemistry described in the following chapters. The chapter covers: inorganic and organic semiconductors; the operation and physics of PV, LSC and LED devices; the synthesis and morphological control of nanocrystals; details of the Shockley-Queisser limit along with a method to surpass it - multiple exciton generation; and the use of Förster resonance energy, as a method for exciton concentration in photo-active antenna complexes.

1.5.2 Chapter 3: Multiple Exciton Generation in Photovoltaic Devices

Chapter 3 looks at a way to circumvent the Shockley-Queisser limit[9], an approximately 32% limit of single-junction PV device power conversion efficiencies. The Shockley-Queisser limit is based on the principle that one photon leads to the generation of a single charge carrier. This means that the excess energy of photons above the bandgap is lost due to thermalization. Multiple excitation generation (MEG), a process in which multiple charge-carrier pairs are generated from a single optical excitation, is a promising way to improve the photocurrent in photovoltaic devices and offers the potential to break the Shockley-Queisser limit. Multiple exciton generation is demonstrated in PV devices fabricated using PbSe nanorods, demonstrating the potential for substantial improvements in device performance due to MEG.

1.5.3 Chapter 4: Antenna Complexes for Luminescent Solar Concentrators

Chapter 3 explores the potential of star shaped oligofluorenes in LSCs. The use of star-shaped oligofluorene molecules containing a central boron-dipyrromethene (BODIPY) core is explored through device measurements and Monte Carlo simulations. These molecules funnel excitations into a central core for emission and thus act as a class of synthetic antennae complexes. It is shown that these oligofluorenes and their analogues have potential as emitter species in LSCs.

1.5.4 Chapter 5: Photon Reabsorption in Light-Emitting Diodes

Chapter 4 investigates the interaction between two different cesium lead halide perovskite nanocrystals. The work explores a method to limit halogen exchange between these perovskite nanocrystals, which enables the subsequent photo-physical measurements to be carried out on mixed samples. Photon reabsorption was found to be a dominant form of energy exchange between $CsPbCl_3$ and $CsPbI_3$ nanocrystals in solution, in films and as part of bulk heterojunction quantum-dot polymer LEDs.

1.5.5 Chapter 6: Conclusion

Chapter 5 presents a summary of the presented work and concludes this thesis

1.6 References

(1) Ballabrera-poy, J.; Garcia, E.; Turiel, A.; Garcia, A. *Sol. Energy* **2012**, *41*, 561–574.

(2) REN21. *Renewable 2011 Global Status Report*; 2016.

(3) Gross, R.; Leach, M.; Bauen, A. *Environ. Int.* **2003**, *29*, 105–122.

(4) Energy Information Administration, U. S. *International Energy Outlook 2011*; Department of Energy: Washington.

(5) Grätzel, M. *Acc. Chem. Res.* **2009**, *42*, 1788–1798.

(6) Solarbuzz. *Solar energy market growth*; Solarbuzz and NPD Group Company, 2010.

(7) Fu, R.; James, T. L.; Woodhouse, M. *IEEE J. Photovoltaics* **2015**, *5*, 524.

(8) Hamaker, H. C.; Ford, C. W.; Werthen, J. G.; Virshup, G. F.; Kaminar, N. R.; King, D. L.; Gee, J. M. *Appl. Phys. Lett.* **1985**, *47*, 762.

(9) Shockley, W.; Queisser, H. J. *J. Appl. Phys.* **1961**, *32*, 510.

(10) Brown, G. F.; Wu, J. *Laser Photonics Rev.* **2009**, *3*, 394–405.

(11) van Sark, W. G. J. H. M.; Brandsen, G. W.; Fleuster, M.; Hekkert, M. P. *Energy Policy* **2007**, *35*, 3121–3125.

(12) van Sark, W. G. J. H. M.; Barnham, K. W. J.; Slooff, L. H.; Chatten, A. J.; Buechtemann, A.; Meyer, A.; McCormack, S. J.; Koole, R.; Farrell, D. J.; Bose, R.; Bende, E. E.; Burgers, A. R.; Budel, T.; Quilitz, J.; Kennedy, M.; Meyer, T.; De, M. D. C.; Meijerink, A.; Vanmaekelbergh, D. *Opt. Express* **2008**, *16*, 21773–21792.

(13) Judkoff, R. *MRS Bull.* **2008**, *33*, 449–454.

(14) The European Parliament and The Council of the European Union. *Off. J. Eur. Union* **2010**, 13–35.

(15) Debije, M. G.; Verbunt, P. P. C. *Adv. Energy Mater.* **2012**, *2*, 12–35.

(16) Ahemen, I.; Dilip, K. De; Amah, A. N. *Appl. Phys. Res.* **2014**, *6*, 95–108.

(17) Mills, E. *Proc. 5th Int. Conf. Energy-Efficient Light.* **2002**, pp. 368–385.

(18) Thejo Kalyani, N.; Dhoble, S. J. *Renew. Sustain. Energy Rev.* **2012**, *16*, 2696–2723.

(19) I., A.; De, D. K.; N., A. A. *Appl. Phys. Res.* **2014**, *6*, 95–108.

2 BACKGROUND

2.1 Semiconductor Physics

2.1.1 Inorganic semiconductors

Many emerging technologies such as PVs, LEDs and thermoelectronics rely on the use of crystalline semiconducting materials[1]. Ideal crystalline materials are characterized by an orderly, periodic arrangement of atoms. The act of bringing so many atoms within close proximity brings about a change in electronic structure allowing the formation of a semiconductor. Electrons associated with isolated atoms have a well-defined set of discrete energy levels available to them. As several atoms are brought closer together, as in a crystal, the original levels blend into bands of allowed energy[2]. When a pair of atoms is brought together in a molecule, their atomic orbitals combine to form pairs of molecular orbitals arranged slightly higher and slightly lower in energy than the original atomic orbitals. As a very large number of atoms come together in a solid, each atomic orbital splits into a very large number of levels which are so close together that they effectively form a continuum, or a band of allowed levels[3] (Figure 2-1 (a)). The highest occupied band which contains the valence electrons is called the valence band (VB). The lowest unoccupied band is called the conduction band (CB)[3]. The energy gap between the bands (E_g) determines whether the material is an electrical insulator, a semiconductor or a conductor. The extent to which the states in each band are occupied and the spacing between adjacent bands determines the materials optical- and thermal-properties[4] (Figure 2-1 (b)).

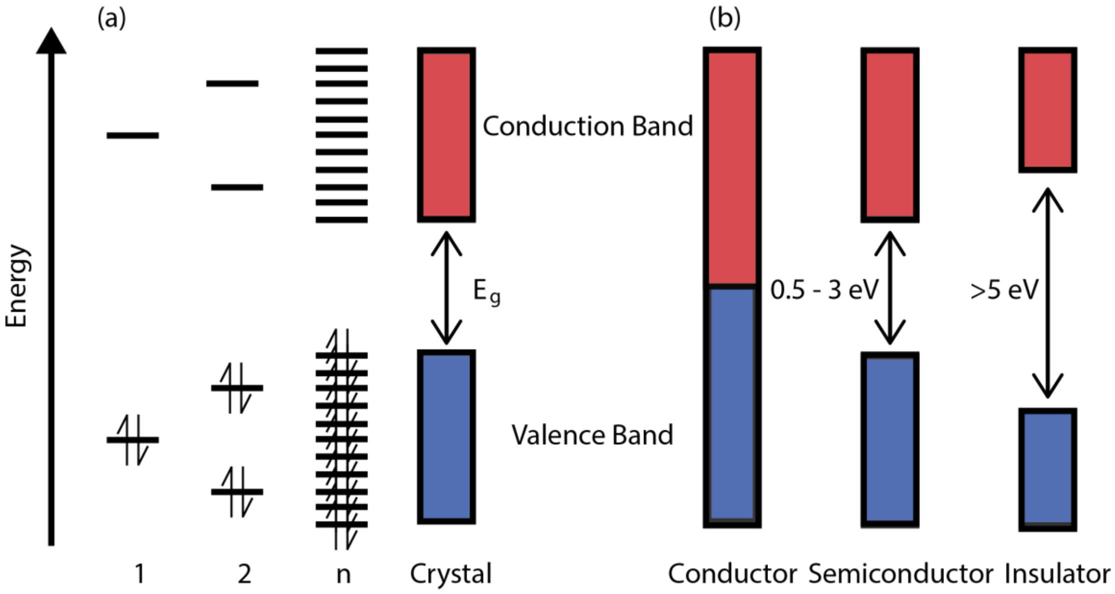

Figure 2-1: Schematic representation of band theory. (a) A schematic indicating how the discrete energies allowed to electrons in an isolated atom split up into bands of allowed energies when a number of similar atoms are brought together in a crystal. (b) The differing band structures of conductors, semiconductors and insulators; overlapping bands represent a conductor; semiconductors are characterized as having a bandgap of 0.5 - 4 eV; and insulators a bandgap of >5 eV.

2.1.2 Organic semiconductors

Like in crystal lattices, orbitals in organic molecules can also lead to the formation bands and subsequent semiconductor properties. Overlap of the un-hybridized carbon P_z orbitals into an extensive network, delocalizes electrons over the whole π-system. As the delocalization extends the atomic orbitals are split and, if many orbitals are involved, they start representing bands seen in semiconductors. In organic semiconductors there is a highest occupied molecular orbital (HOMO) and a lowest un-occupied molecular orbital (LUMO) instead of a CB and VB (Figure 2-2). Interaction with light of the appropriate wavelength causes an electron from the HOMO to be promoted to the LUMO, leading to the formation of Coulomb-bound electron-hole pairs, so called excitons, which can be separated to generate charges[5].

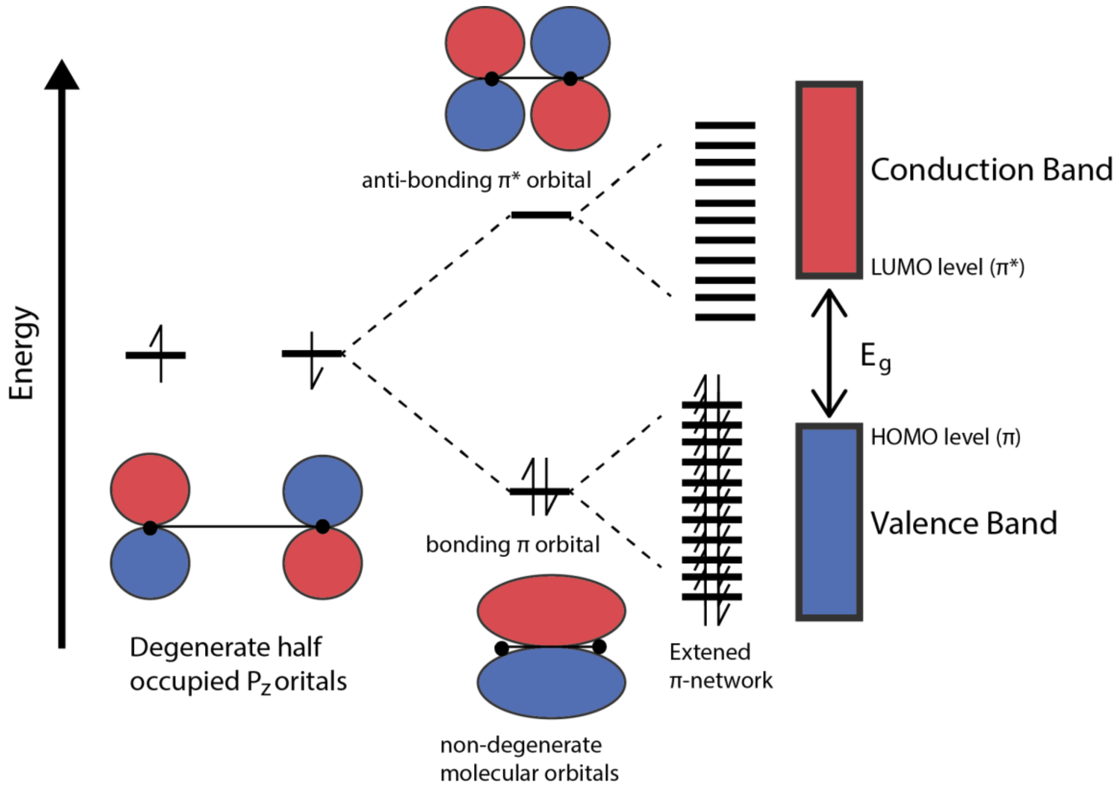

Figure 2-2: Schematic representation of the HOMO and LUMO energy levels formed by the π bonding and π^* anti-bonding molecular orbitals in conjugated polymers. The diagram illustrates the quasi-continuous bands (with a bandgap that is smaller than the initial $\pi - \pi*$ gap) formed when a large number of P_z orbitals overlap.

2.1.3 Nanocrystalline semiconductors

Nanocrystal (NC) semiconductors, quantum dots (QDs) are small particles of semiconductor materials that have potential in optoelectronic applications. QDs can be considered as an intermediate species between atoms or molecules and bulk material. As the size of semiconducting nanocrystals is reduced, the electronic transitions shift to higher energy, and the oscillator strength is concentrated into just a few transitions[6]. Spherical nanocrystals can be considered as zero-dimensional objects, for which confinement is exerted in all three dimensions and consequently the density of states is discontinuous[7] (Figure 2-3). This quantum-size effect drastically modifies the energy spectra of three-dimensionally confined nanocrystals[8].

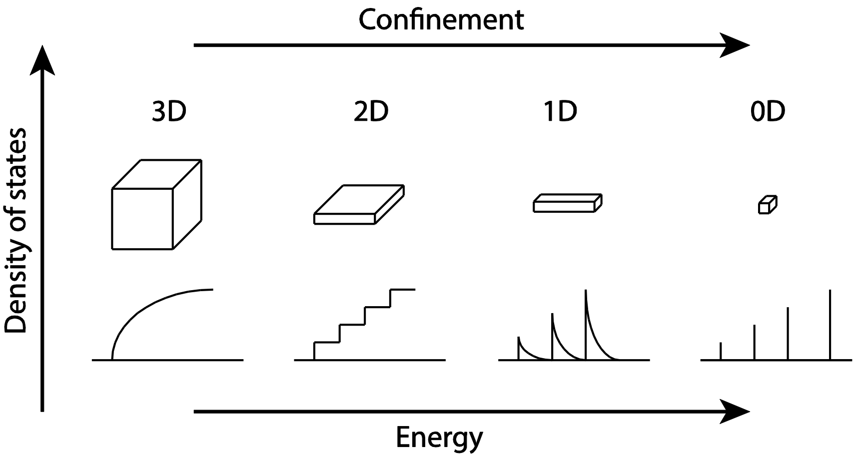

Figure 2-3: Density of states in one band of a semiconductor as a function of dimension.

Thus nanocrystal absorption and luminescence is size dependent. In a spherical nanocrystal surrounded by an infinite potential barrier, the energy of the electron and hole quantum-size levels, depends on the angular momentum quantum number *l* and the principle quantum number *n* and can be written as

$$E_{l,n}^{e,h} = \frac{\hbar^2 \phi_{l,n}^2}{2m_{e,h}\alpha^2}, \tag{2-1}$$

where $m_{e,h}$ is the electron and hole effective mass respectively, α is the crystal radius, $\phi_{l,n}$ is the nth root of the spherical Bessel function of order *l*, i.e. $j_l(\phi_{l,n}) = 0$.[8,9] The effective mass approximation (EMA) shown above gives the correct qualitative picture of the energy levels and wave function in these materials. However the EMA provides only an approximate estimate of the confinement energies in QDs as it does not take into account band mixing[10]. Also Coulomb interaction between the electron and hole must always be taken into account because both particles are confined in the same volume[8]. These factors lead to an increase in the complexity of nanocrystal electronic states. Nevertheless quantum confinement provides a method for bandgap engineering as decreasing the size of the particles results in confinement of the electron and hole wavefunctions, thus increasing the bandgap[11]. The lower limit for the bandgap is that of the bulk material. This value is reached when the radius of the crystal is of the order of the Bohr radius of the exciton (Figure 2-4) [7].

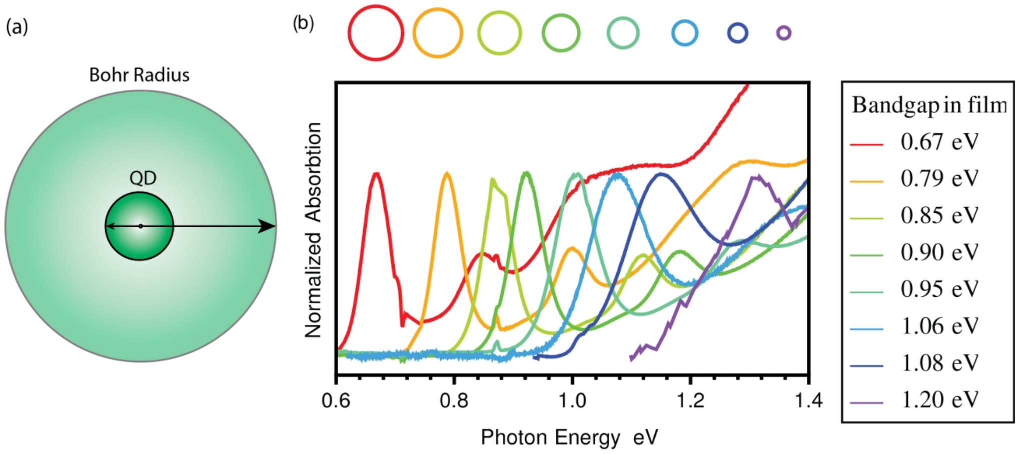

Figure 2-4: A schematic representation of the quantum size effect in nanocrystal quantum dots. (a) A schematic representation of a nanocrystal quantum dot with corresponding exciton Bohr radius. As the Bohr radius of the exciton is larger than the nanocrystals, the exciton is confined within the dimension of the quantum dot leading to a state called quantum confinement. (b) Visual representation of the quantum size effect in PbSe nanocrystals. As the size of semiconducting nanocrystals are reduced, the electronic excitations shift to higher energy.

2.1.4 Optical properties

The absorption of photons by a semiconductor can promote electrons from the valence band to the conduction band. The excited electrons in the conduction band are able to travel and transport charge or energy[3]. When an electron is promoted to the conduction band, a positively charged hole remains. This hole can be filled by another electron creating a new hole which can in turn be filled leading to the conduction of holes. In many situations the correct motion of the hole can be predicted if it is regarded as a physical particle of positive charge[2] (Figure 2-5). These positive holes can be characterized with mobility and an effective mass, just like conduction electrons[3]. Thus semiconductors have two types of free carriers, electrons and holes. For intrinsic semiconductors, without external stimuli, such as external radiation or heat, the product of the electron and hole concentrations at a given temperature is constant[12]. Excess carriers can be generated by either absorption of light or by current injection. The total carrier concentration is then given by the sum of the equilibrium and excess carrier concentrations

$$n = n_0 + \Delta n \text{ and } p = p_0 + \Delta p, \qquad (2\text{-}2)$$

where n_0 are p_0 are the equilibrium electron and hole concentrations, and Δn and Δp are the excess electron and hole concentrations[13].

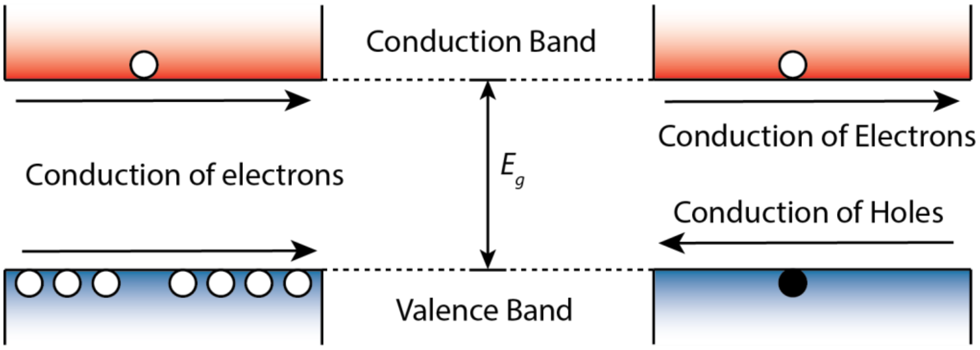

Figure 2-5: A depiction of the motion of conducting electrons and consequent holes. Movement of electrons, shown as white circles and holes, black circles, after corresponding excitations of an electron from the valence to conduction band. The situations depicted on the left and the right are equivalent, using holes to represent missing electrons

The emission processes of photons in semiconductors are similar to molecular chromophores. Electrons and holes can combine either radiatively or non-radiatively. Radiative recombination results in the emission of a photon with energy equal to the bandgap energy of the semiconductor, whereas during non-radiative recombination the energy is converted to phonons. The number of recombination events is proportional to both the number of electrons and holes (Figure 2-6). Thus the recombination rate is proportional to the product of electron and hole concentrations[13].

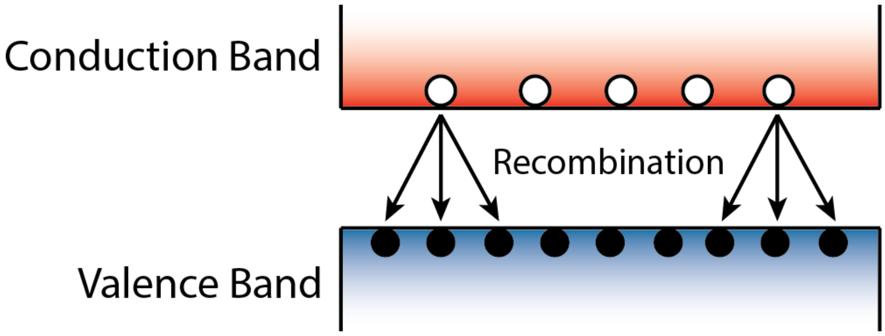

Figure 2-6: Illustration of electron–hole recombination. Electrons are shown as white circles and holes as black circles.

2.2 Nanocrystal Synthesis

Over the past decade research has focused on optimizing the synthesis of semiconductor nanocrystal quantum dots. Synthetic routes utilizing organometallic precursors enable the production of nanocrystalline particles with near monodisperse size distribution[14]. The preparation of nearly monodisperse well passivated NC samples is essential to permit studies that distinguish the truly novel properties inherent to nanoscale structures from those associated with structural heterogeneities or polydispersity. NC samples must be uniform not only in size and shape, but they must also have well-formed crystalline cores and controlled surface chemistry.[15] The production of monodisperse colloidal crystals requires a temporally discrete nucleation event followed by a slower controlled growth of the existing nuclei. This relies on rapid precursor injection to achieve a separation of the nanocrystal nucleation and growth stages[16].

Rapid addition of reagents to the reaction vessel raises the precursor concentration above the nucleation threshold[15] (Figure 2-7). Subsequently, as long as the consumption of feedstock by the growing colloidal NCs is not exceeded by the rate of precursor addition to solution, no new nuclei form. Since the growth of any one NC is similar to all others, the initial size distribution is largely determined by the time over which the nuclei are formed. At high precursor concentrations small nanocrystals grow at a quicker rate compared to larger nanocrystals, thus the NCs can become more uniform over time. This phenomenon has been referred to as focusing of the size distribution. Many systems exhibit a second, distinct, growth phase, at low precursor concentrations, called Ostwald ripening. In this process the high surface energy of the small NCs promotes their dissolution, leading to material being redeposited on the larger NCs. This caused the average NC size increases over time with a compensating decrease in NC number[15,17].

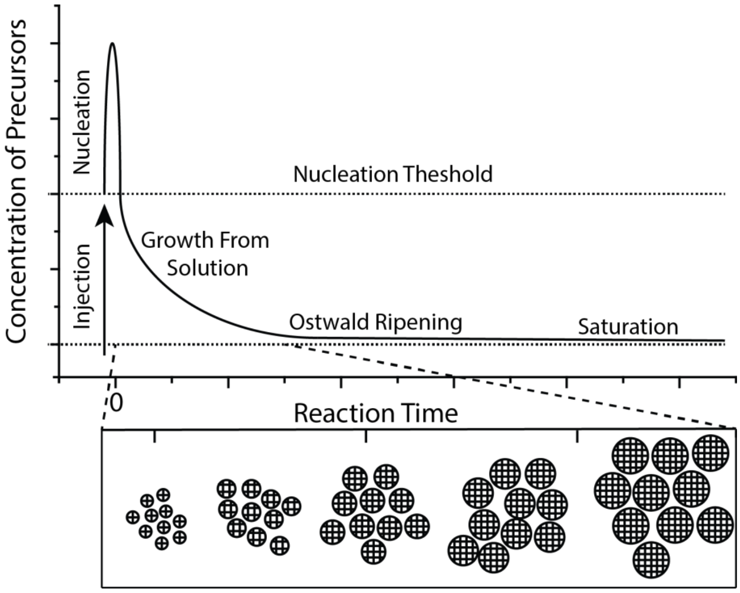

Figure 2-7: Nucleation and growth of nanocrystals. Upon injection the concentration of the precursors rises above the nucleation threshold, promoting the formation of crystal seeds. The concentration then drops below the nucleation threshold and crystal growth proceeds.

2.2.1 Lead chalcogenide nanocrystals

Semiconductors of group III-VI materials offer excellent size tunability across the NIR and visible region and can be produced with inexpensive and relatively safe synthetic precursors. The use of colloidal lead chalcogenide QDs (PbX; X = S, Se, Te) has become increasingly widespread because they can be synthesized using relatively simple methods to exhibit bright, narrow emission energies spanning a very wide range from near- to mid-IR[14,18–20]. Recently these QDs have garnered particularly intense attention over other IR QDs because of their extensive use in the development of next-generation QD-based solar cells. This surge was inspired largely by reports of high carrier multiplication efficiencies in lead chalcogenide QDs[18,21,22]. Lead chalcogenides offer several unique advantages such as a small bulk bandgap (with large tunability using quantum confinement), large Bohr exciton radius (α_B = 46 nm in PbSe; 18-20 nm in PbS; and ≈80 nm in PbTe), good stability and relatively well-established and reproducible synthesis[22].

Lead chalcogenides are usually synthesized though hot injection methods. S, Se or Te powder is dissolved in a coordinating phosphine, usually trioctylphosphine. This is then injected into a solution of lead salts, and large aliphatic ligands, dissolved in a non-coordinating solvent at an elevated temperature. The reaction can then be quickly quenched by lowering the temperature. This rapid injection of precursors allows a short nucleation phase followed by an extended growth phase, and combined with quick reaction quenching, results in near monodisperse nanocrystal samples. Production of lead chalcogenide QDs has also been achieved in the gas phase[23], solid state [24], as polymer films[25], in glass hosts[26] and grown within bacteria[27].

2.2.2 Lead selenide nanorods

While the majority of nanocrystal photovoltaic research is focused on spherical zero-dimensional dots. The use of other nanocrystalline morphologies such as one-dimensional rods offers a new avenue of research with many potential advantages over more established materials. Shape control of the nanocrystals can be achieved by further manipulation of the growth kinetics. Alivisatos and co-workers demonstrated the first shape controlled colloidal synthesis of pure semiconductor nanrods (NRs)[28]. In this synthesis, CdSe NRs were obtained via a surfactant-controlled growth approach, taking advantage of the anisotropic wurtzite crystal structure of CdSe. Wurtzite CdSe is intrinsically an anisotropic material, with a unique c-axis, and when the overall growth rate is fast, growth is generally faster along this axis[28]. Utilizing appropriate coordinative surfactants (mostly phosphonic acids), enabled tuning of the growth kinetics of the chemically dissimilar lattice facets, which resulted in faster growth along the c-axis of the wurtzite crystal, and yielded elongated NRs[29]. Oriented attachment can also produce nanowires (NWs) with control of wire dimensions and morphology. This involves spontaneous self-organization of adjacent particles so that they share a common crystallographic orientation, followed by fusing of these particles at a planar interface[30]. Previously, Cho et al. reported PbSe nanowires made by oriented attachment[31]. In addition to straight nanowires, zigzag, helical, branched, and tapered nanowires as well as single-crystal nanorings were shown to be controllably prepared in one-pot reactions by careful adjustment of the reaction conditions. The inherent anisotropy of crystal structure has been identified as a driving force for one-dimensional growth[28,29,31]. However lead chalcogenides form highly symmetric rock-salt lattices. As such the origin of a dipole moment required for orientated attachment is not initially apparent. Transmission electron microscopy (TEM) has shown that the shape of PbSe nanocrystals evolves during growth from quasi-spherical to cubic. Small PbSe nanocrystals are terminated by six {100} facets and eight {111} facets. The {100} facets are formed by both Pb and Se atoms while the {111} facets must be either Pb- or Se-terminated. Due to the difference in electronegativities between Pb and Se, {111} facets are polar and their arrangement will determine the distribution of electric charge within the PbSe nanocrystal. Depending on the mutual arrangement of the {111} facets, the whole nanocrystal can either have central symmetry and thus a zero net dipole moment or it can lack central symmetry and possess a dipole moment along the <100>, <110>, or<111> axes (Figure 2-8).

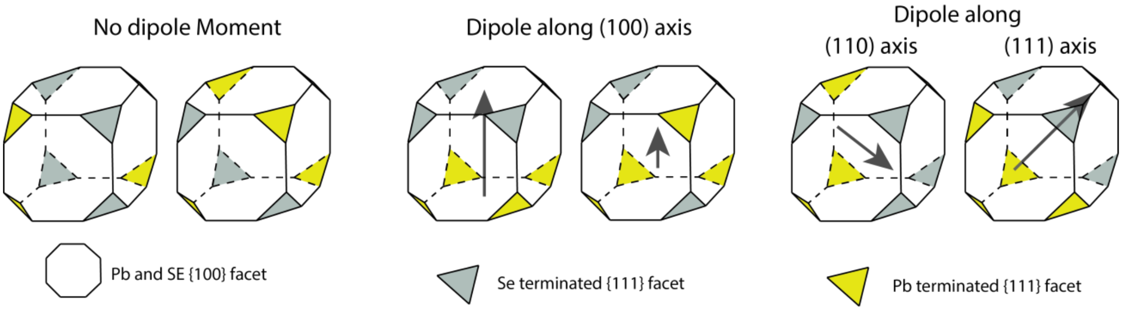

Figure 2-8: Dipole moments of PbSe nanocrystals. Different arrangements of polar {111} facets result in various orientations and magnitudes of the nanocrystal dipole moment. Showing Pb-terminated {111} facet (yellow), Se-terminated {111} facet (grey) and the subsequent dipole moment and magnitude (black arrow).

Assuming a random distribution of {111} facets it has been calculated that ≈89% of nanocrystals will have a dipole; furthermore it has been suggested that due to the dynamic nature of the growth of the {111} facets all nanocrystals can develop a dipole during growth and thus are all nanocrystals are available for orientated attachment[31]. Simple, high-quality PbSe NR synthesis at low temperatures and long timescales has been shown with the replacement of TOP with tris(diethylamino)phosphine (TDP)[32] (Figure 2-9).

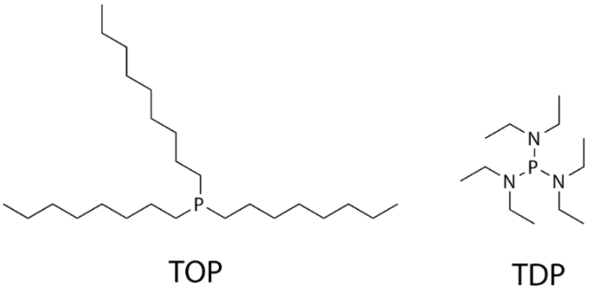

Figure 2-9: Molecular structure of TOP and TDP. The preferential synthesis of nanorods over quantum dots is facilitated by the replacement of TOP with TDP

2.3 Photovoltaic Devices

2.3.1 Photovoltaic device operational principles

The essential function of a solar cell is the generation of power under illumination. The output is determined by a balance between light absorption, charge generation, extraction and recombination[3]. Generation can be considered as the promotion of an electron from the valence band to the conduction band, creating an electron hole pair. Recombination is the loss of an electron in the conduction band through relaxation with a hole in the valence band and thus is detrimental to device performance. Once generated, these free charge carriers are exposed to an internal asymmetry, an intrinsic property of a PV device, producing electron and hole photocurrents[2–4] (Figure 2-10).

The operating regime of a photovoltaic cell is in the range of positive voltage bias, usually from 0 V to the open circuit voltage (V_{oc}), in which the cell delivers power. The cell power density is given by

$$\mathrm{P} = \mathrm{JV}. \qquad (2\text{-}3)$$

Where P is the power, J is the current density and V is the voltage. P reaches its maximum at the cell's operating point or maximum power point: this occurs at some voltage V_m with a corresponding current density J_m (Figure 2-10). The fill factor is defined as the ratio

$$\mathrm{FF} = \frac{\mathrm{J_m V_m}}{\mathrm{J_{sc} V_{oc}}}. \qquad (2\text{-}4)$$

The efficiency of the cell is the power density delivered at the operating point as a fraction of the incident light power density, P_s,

$$\eta = \frac{\mathrm{J_m V_m}}{\mathrm{P_s}} \times 100\%. \qquad (2\text{-}5)$$

Efficiency is related to J_{sc} and V_{oc} using FF,

$$\eta = \frac{\mathrm{J_{sc} V_{oc} FF}}{\mathrm{P_s}} \times 100\%. \qquad (2\text{-}6)$$

These four quantities J_{sc}, V_{oc}, FF and η are the key performance characteristics of a solar cell[3]. All of these should be defined for particular illumination conditions. The standard test condition for solar cells is the Air Mass 1.5G spectrum[33], an incident power density of 1000 W m^{-2} and a temperature of 25 ^{o}C.

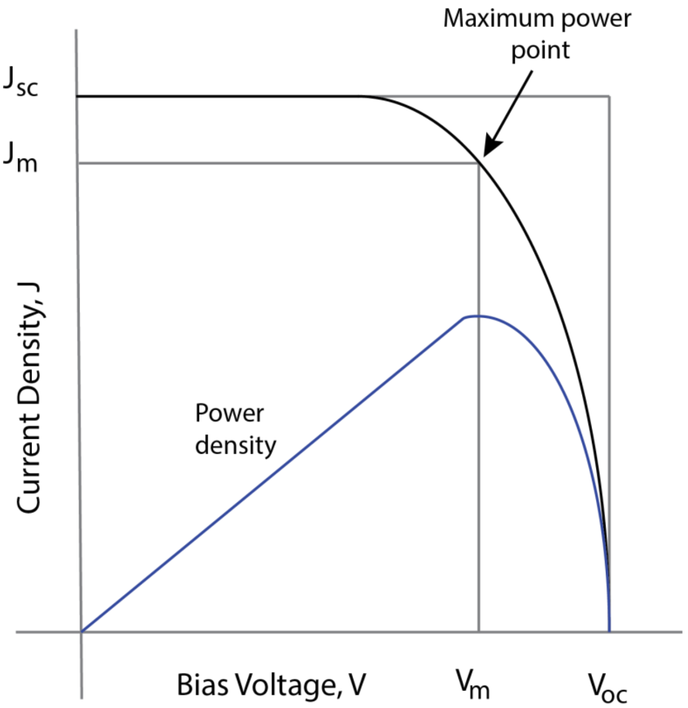

Figure 2-10: The current-voltage (black) and power-voltage (blue) characteristics of an ideal cell. Power density reaches a maximum bias at V_m. The maximum power density $J_m \times V_m$ is given by the area of the inner rectangle. The outer rectangle has an area of $J_{sc} \times V_{oc}$.

Single-junction PV cells exhibit a single absorption threshold, with a single energy gap (E_g) between the valence and conduction bands (Figure 2-11). Single-threshold PV cells operate most efficiently within a narrow wavelength range[34,35]. The fact that the sun has a broad emission spectrum, that spans the ultraviolet, visible and infrared regions, leads to the single-threshold design having a variety of inherent loss mechanisms. The majority of these losses are caused by transmission of photons with energies lower than the bandgap of the cell (Figure 2-11 (a)) and by thermalization of highly energetic charges which dissipate energy in excess of the bandgap as heat (Figure 2-11 (c)). As a result, single-threshold cells can only efficiently harvest a limited portion of the solar spectrum and its energy. The first-generation of PV cells include mono- and polycrystalline silicon wafers (c-Si). The champion c-Si cells have demonstrated efficiencies exceeding 25%. Single threshold GaAs cells have reached efficiencies of up to 26.2%[36] and are approaching the ≈32% Shockley-Queisser limit for single-junction cells[37]. Although these first-generation cells approach the efficiency limit, they are expensive to manufacture and require high-purity semiconductors[38].

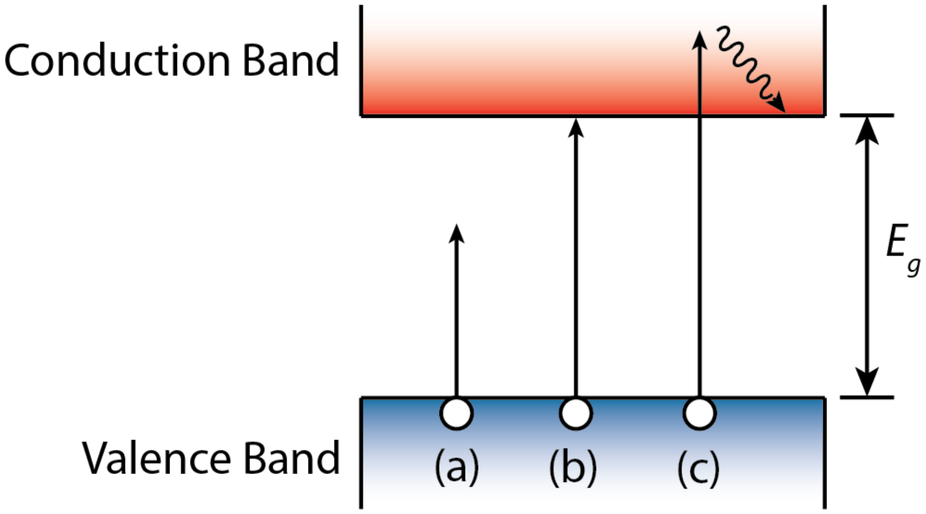

Figure 2-11: A schematic representation of the band structure of a single-threshold solar cell with a bandgap of E_g: (a) Photons with energies less than E_g are not absorbed; (b) the cell efficiently utilizes photons with energies at or slightly greater than E_g ;(c) photons with energies greater than E_g are absorbed, but their excess excitation energy is lost, as electrons relax to the local energy minimum at the bottom of the valence band (thermalization).

Due to the large cost associated with first generation cells a new generation of cells were developed. These cells aim to replicate the efficiency of the first-generation but at a lower cost. Second-generation PV cells use thin films of semiconductor materials, 100-1000 times thinner than first generation silicon wafers[39,40]. Due to reduced material consumption, more exotic and expensive semiconductors are rendered commercially viable. Second-generation PV cells such as CdTe and Copper indium gallium selenide (CIGS) devices have reached efficiencies of greater than 20%, [38,41,42].

The highest efficiency PV cells to date are the multi-junction tandem cells, which have reached efficiencies of over 40%[43,44]. Multi-junction cells consist of a number of bandgaps, each tuned to absorb a different part of the spectrum[45]. Although this increases efficiency, multi-junction cells are still considered too expensive for widespread energy production[46]. Third generation PV cells include those cells which try to surpass the 32% Shockley-Queisser limit for single-bandgap cells set by detailed balance[37]. They include intermediate-band cells, hot carrier cells and spectrum management technologies (up/down conversion)[47].

2.3.2 Nanocrystal photovoltaic devices

Colloidal quantum dots (CQDs) have potential for photovoltaic devices. They are solution processable, can be fabricated at low temperatures and are capable of absorbing the sun’s visible and infrared wavelengths[11]. This combined with their structural and photophysical features (bandgap tunability, multiple exciton generation, self-assembly), and the promise of inexpensive device fabrication (by dropcasting, spin coating, printing and spraying), drives the development of NC-based optoelectronic technologies[48]. Even so the development of optoelectronic devices based on semiconductor nanocrystals has been hampered by the fact that CQDs have an inherent instability under ambient conditions, which is possibly due to destructive oxidative processes occurring at the NC surface[49]. Furthermore, CQDs typically possess electrically insulating organic ligand shells that must be shortened or removed to alloy charge transport in NC PV devices[48]. A separate role of these shorter ligands is to passivate surface traps by chemically bonding with the NC surface. Surface traps can be classified into two major groups. Firstly shallow traps, which are at energies slightly below the conduction band or above the valence band, these are less detrimental to device performance, as shallow-trapped charge-carrier pairs can recombine radiatively or relax back to the band edges, such that losses to efficiency are relatively minor. Secondly deep traps; which are much lower in energy and are close enough in energy to the valence band edge to allow non-radiative recombination such that charge carrier pairs trapped this way are unable to contribute to the device's photocurrent (Figure 2-12). Surface traps and the choice of ligands have the ability to effect the V_{oc}, photoluminescence quantum yield, charge generation and transport, recombination rates and ultimately overall power conversion efficiency (PCE) of nanocrystal PV devices [18].

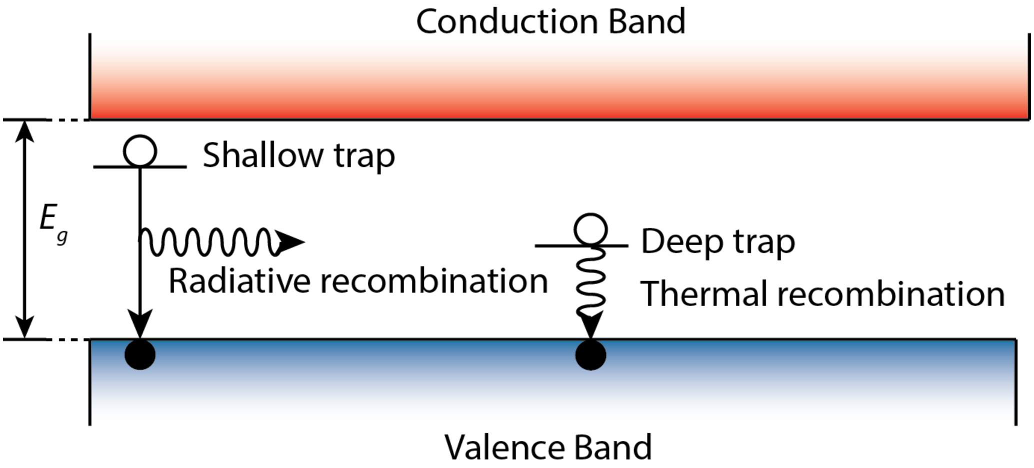

Figure 2-12: A schematic representation of shallow and deep trap states and corresponding electron-hole recombination within the bandgap of nanocrystal semiconductors. Electrons are shown as white circles and holes as black circles.

Currently NC photovoltaic devices have reached efficiencies of greater than 10%[50] but are generally lower[11]. The low overall power conversion efficiencies of these devices has been limited largely to low V_{oc}, regardless of the type of junction used. Generally this is understood to be due to Fermi level pinning at the mid-gap states, which are formed by a large number of surface states associated with defects on the QD surface[51]. At the surface of a crystal, the periodicity of the bulk crystal lattice gives way to faceting, bond contraction, reconstruction, unsaturated/daggling bonds as well as physisorbed and chemisorbed molecular species. With dimensions on the order of a few nanometers many of the atoms in nanocrystals are located at or near the surface[52] . This high ratio of surface area to volume make NCs prone to high trap state densities. Imperfectly passivated surfaces promote recombination of charge carriers and are detrimental to device performance[53,54]. In order to improve CQDs optical properties, chemical stability and photostability, several approaches have been developed, including passivation of the NC surfaces with inorganic shells[18,49]. While these measures have achieved varying levels of success they result in complex, heterostructured materials with altered carrier dynamics[18]. Another technique is to replace the long insulating ligands that enable colloidal stability following synthesis with short organic linkers, leading to improved surface coverage and higher packing densities[48,54,55]. In situ growth of a passivating surface layer has also been demonstrated as a promising means to enhance both the chemical stability and the optical properties of QDs[18].

2.3.3 Nanorod photovoltaic devices

Nanorods (NRs) are advantageous) in photovoltaic applications for several reasons: the elongated geometry improves carrier extraction as it provides a longer undisrupted pathway for charge migration, absorption paths are maximized while maintaining the short distances required for carrier collection, and the material's properties can be manipulated by varying the size of the nanostructures[19,56–58]. There is a trade-off between these advantages and the difficulties of fabricating devices, such as issues with recombination centers at interfaces. Also the NRs tend to lie flat within the plane of the film, which is not the optimum arrangement for electron extraction[56,58]. The device performance depends not only on the shape of the nanoparticles, but also on the arrangement of the nanoparticles within the film. Careful control of the film and particle morphology is therefore required for efficient devices[59].

2.3.4 Multiple exciton generation

CQDs have potential for low cost, high efficiency photovoltaics, with current research looking at improving charge generation, separation and mobility which aims to increase overall PCEs[11]. Multiple exciton generation (MEG)[21] is a scientifically interesting process that might improve PCEs above the Shockley-Queisser limit. MEG is a process in which multiple electron-hole (e-h) pairs are generated from a single photon. MEG provides increased PCE in the form of increased photocurrent[21]. A single junction PV cell with an ideal MEG yield can produce a PCE exceeding 40%[60], which is a considerable improvement over the traditional Shockley-Queisser limit. The ideal MEG yield is described by a staircase function in which each increment of the incident photon energy ($\hbar\omega$) from the bandgap (E_g) results in a new e-h pair. This corresponds to an increase to exciton conversion quantum efficiency (QE) of 100%[61]. Recently Semonin et al.[62] demonstrated the first solar cells with external quantum efficiency (EQE) of greater than 100 %.

MEG, which was first observed in the 1950s in bulk semiconductors as impact ionization, has been predicted to occur more readily in nanocrystals. The relaxation processes and rates at which photo-generated charge carriers return to equilibrium can be greatly affected by the quantization of energy levels, such as occur in QDs[63]. Although there are many different views on the process by which MEG occurs, as of yet there is not a single conclusive theory[64–67]. The concept can be visualized via the process of impact ionization that occurs in bulk semiconductors. Impact ionization is an Auger-type process whereby a high energy exciton, created by the absorption of a photon of energy $\geq 2E_g$, relaxes to the band edge via the energy transfer of at least $1E_g$ worth of energy to a valence band electron, which is thus excited across the energy gap[21] (Figure 2-13 (a)). The result is that two excitons are formed for one absorbed photon. Therefore the process converts more of the high photon energy portion of the solar spectrum into usable energy[21]. Auger recombination (AR), the inverse process of impact ionization, is a process in which an exciton recombines via energy transfer to an electron (or hole) that is excited to a higher-energy state (Figure 2-13 (b)).

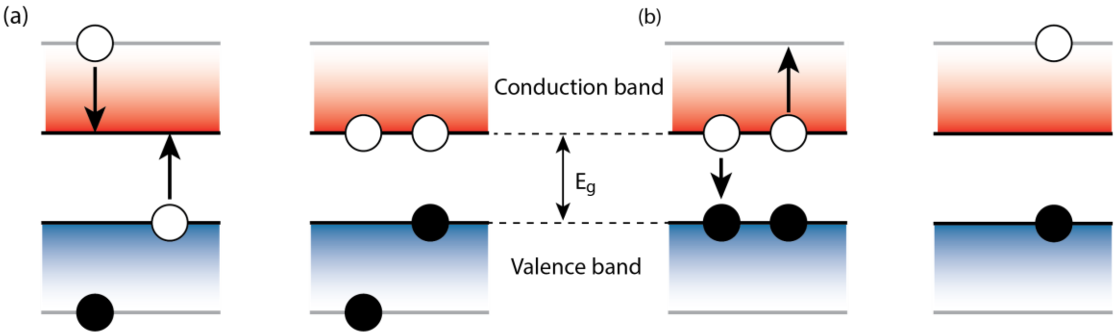

Figure 2-13: A schematic representation of impact ionization and Auger recombination, with electrons (white circles) and holes (black circles). (a) Following initial excitation from a high energy photon, and (b) Auger recombination between two excitons

MEG is usually measured via spectroscopy through monitoring the conversion of excitons into biexcitons which can distinguish by their different relaxation dynamics. While excitons recombine slowly on a submicrosecond time scale, biexcitons recombine very rapidly via AR on a picosecond time scale[21]. The initial research into MEG materials was hampered by difficulty in accurately measuring MEG yields. These difficulties were caused by; pump beam inhomogeneities[68]; photo-charging of the nanocrystals samples[69]; and variations in the surface chemistry of the samples[70]. Through the improved understanding of these effects, experiments were developed that eliminated these misleading artefacts leading to reliable MEG efficiency measurements[69–71]. The direct measurements of MEG has recently been achieved in PbSe nanocrystals devices which showed EQEs exceeding 100%[62].

Two important parameters of the MEG process are the activation threshold ($\hbar\omega_{th}$) and the e-h pair creation energy (ε_{eh}). $\hbar\omega_{th}$ is the minimum energy required to achieve MEG and ε_{eh} is the energy required to generate a new exciton after the MEG threshold is reached[61]. ε_{eh} directly accounts for the competition between impact-ionization-like events producing new excitons and non-MEG intraband relaxation[72]. Energy conservation dictates that the minimal values of ε_{eh} and $\hbar\omega_{th}$ are E_g and $2E_g$ respectively[61]. Due to restrictions imposed by energy and momentum conservation, impact ionization is an inefficient processes in the bulk material with both ε_{eh} and $\hbar\omega_{th}$ considerably higher than the minimum values. QDs present a promising alternative to bulk materials when it comes to MEG, as impact ionization type processes are more efficient in NCs due enhanced Coulomb interactions and relaxation of momentum conservation and the NCs discrete energy states are expected to reduce phonon emission[61,63].

An important consequence of the strong confinement in NCs is a significant enhancement in the carrier-carrier Coulomb interactions resulting from forced overlap of electron wavefunctions and reduced dielectric screening associated with interface polarization effects[73]. It has been found that the MEG activation threshold ($\hbar\omega_{th}$) in nanocrystal systems can be understood in terms of simple bulk-semiconductor, effective-mass arguments without the need to be aware of the precise electric structure of NCs[74]. In a simple two-band model, optical excitation of the bulk material preserves the results in both the photoexcited electron and a hole being characterized by the same set of quantum numbers: angular momentum (l) and the principle quantum number (the number of nodes in its radial component (n))[80]. As a result, the energies of photoexcited electrons (E_e) and holes (E_h) are given by

$$E_{e,h} = \left(\frac{\hbar^2\phi_{nl}^2}{2m_{e,h}R^2}\right), \qquad (\ 2\text{-}7\ )$$

where m_e and m_h are electron and hole effective masses, R is the NC radius, and ϕ_{nl}^2 is the nth root of the Bessel function of the lth order[80]. This expression indicates that the energy of a photon in excess of the energy gap ($\hbar\omega$ - E_g) is distributed between the electron and the hole in inverse proportion to their effective masses: $E_e/E_h = m_h/m_e$. Applying energy conservation and assuming $m_e \leq m_h$, this yields an activation energy of

$$\hbar\omega_{\mathrm{th}} = (2 + \mathrm{m_e}/\mathrm{m_h})\mathrm{E_g}. \qquad (\ 2\text{-}8\ )$$

It has been reported that this model can also be used to determine the MEG activation threshold in NC systems[80]. Due to the mirror symmetry of electron and holes in lead salts the activation energy of lead chalcogenides is predicted to be around $3Eg$, which agrees with experimental measurements[19,61,62,74–78]. Of course, this simple two-band model does not take into account the complexity of electronic band structures in semiconductors, but it can act as a good guide for predicting $\hbar\omega_{th}$.

It is convenient to express the e-h pair creation energy in terms of E_g and the dimensionless MEG efficiency (η_{MEG}). The η_{MEG} serves as a photon energy independent measure of MEG and captures the underlying photophysics regarding the competition between hot carrier cooling to the band edge and the processes leading to production of new electron pairs[22]. There are two factors that influence η_{MEG}: the rate of producing multiexcitons from the initially photogenerated hot exciton, k_{MEG}, and the competition with hot-exciton cooling pathways, k_{cool}[22]. For the generation of the first two excitons, the MEG quantum yield (QY) can be expressed in terms of the rate constants for MEG and cooling by

$$\mathrm{QY} = 1 + \frac{\mathrm{k}_{\mathrm{MEG}}^{(1)}}{\mathrm{k}_{\mathrm{MEG}}^{(1)} + \mathrm{k}_{\mathrm{cool}}}, \qquad (2\text{-}9)$$

where $k_{MEG}^{(1)}$ is the rate constant for producing two excitons fom one hot exction[22,79]. This has been expanded to included higher order MEG events [22], however for our analysis this is unnecessary. As k_{cool} is relatively independent of excess energy[80], and k_{MEG} increases rapidly above $\hbar\omega_{th}$ [81,82], the MEG QY increases with higher energy excitation.

Currently the increases in PCEs in PV devices due to MEG is still too moderate to show significant improvements[83,84]. Therefore, an important current challenge in the MEG field is the development of nanostructures in which the MEG performance approaches the energy conservation defined limit where quantum efficiency of photon-to-exciton conversion increases by 100% per each increment in the photon energy of E_g[85]. It has been suggested that the surfaces of NCs can modulate the efficiency of the MEG process[69,86]. It is known that surfaces of NCs have a large impact on their photophysical properties and that carrier relaxation and dynamics are affected by the surface ligands[87]. MEG may depend on the detailed chemistry and interactions at the NC surface. Efficient surface passivation can be achieved by the exchange of surface ligands for control of surface coverage or the epitaxial growth of another semiconductor onto QDs, leading to the formation of core-shell heterostructures[88]. Further improvements to MEG-enhanced quantum efficiency will necessarily involve maximizing the MEG kinetics by chemical, dimensional, or physical arrangement of individual particles, while also limiting the phonon-mediated exciton cooling rates[62].

2.3.5 Multiple exciton generation in nanorods

To date, MEG has been most extensively investigated for spherical semiconductor NCs[69]. Another potentially interesting class of NC materials is elongated nanoparticles, or nanorods. NRs have the potential for increased MEG efficiency due to weaker carrier-carrier coulomb interactions[89] and reduced dielectric screening[90]. A further enhancement may arise from the reduced symmetry in these structures, which would increase the number of multiexciton states accessible via the MEG process[19]. NRs also allow the reduction of losses by Auger recombination. Elongation of the nanocrystal reduces the effective density of charges (and hence Auger decay rates) while simultaneously preserving a significant degree of spatial confinement[19,91]. Recent results reveal a systematic scaling of the biexciton Auger lifetime with NR volume. The analysis of MEG efficiencies in NRs indicates a dependence of MEG yield on NR aspect ratio, ρ (defined as $\rho = L/D$, where L is the nanocrystal length and D is the nanocrystal diameter), such that, independent of E_g, the quantum efficiency of photon-exciton conversion grows with increasing ρ until it reaches a maximum at ρ = 6-7 and then drops (Figure 2-14). For this optimal value of ρ the MEG yield exceeds that of QDs by a factor of up to ~ 2[19].

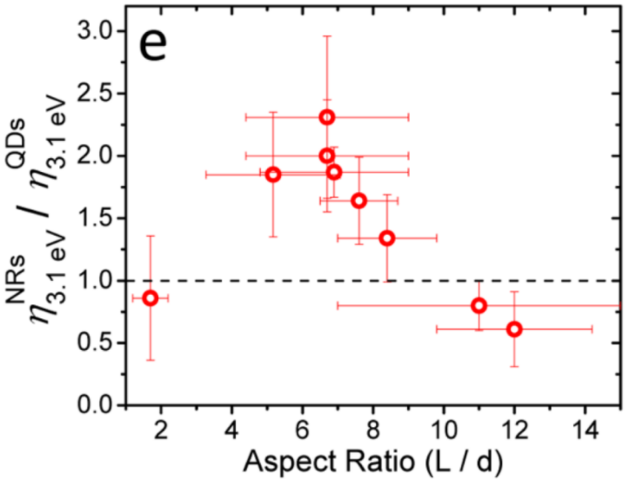

Figure 2-14: The MEG yield enhancement factor for NRs versus QDs as a function of NR aspect ratio. Figure taken from Padilha et al.: Nano Lett. 2013, 13, 1092–1099 - Aspect ratio dependence of auger recombination and carrier multiplication in PbSe nanorods.

2.4 Luminescent Solar Concentrators

2.4.1 Concentration systems

Independent of the PV technology itself, by increasing the sunlight incident on the surface of a solar cell it may be possible to make reductions to the price per Watt of the installed photovoltaic system. The open-circuit voltage, the difference between the quasi fermi levels, depends on the charge density, which is higher under higher light concentrations. In addition to this, under high currents, trap states are saturated which leads to improvements in charge transport. Both higher V_{oc} and better charge transport improve device efficiency[92–94]. Also, entropically there exists a radiative balance between a solar cell and its environment[95]. This leads to a fundamental thermodynamic loss in solar cells due to the radiation of photons into the low temperature environment *i.e.* not toward the sun, which reduces the maximum V_{oc}. Briefly,

$$V_{oc} \propto kTln(\frac{\Omega_{emit}}{\Omega_{sun}}) \qquad (\ 2\text{-}10\ )$$

where Ω_{emit} and Ω_{sun}, are the spherical angle of the light emitted and absorbed by the solar cell. With concentration Ω_{sun} is increased and the maxim achievable V_{oc}. Furthermore, concentrated light requires a smaller solar cell area than under normal solar illumination. These factors mean that concentration systems have the potential to increase PV efficiency, whilst lowering the cost per installed Watt[96].

Current commercial solar concentration systems generally involve the concentration of light via focusing with mirrors. This requires mechanical tracking of the sun and integrated optics. Due to the concentration of broad band solar radiation, the PV units operate at high temperatures and necessitate the need for expensive cooling systems. This cooling as well as the tracking and optics increases the mechanical complexity and the required space of the PV installation. Overall, this makes such systems unsuitable for small-scale installations, or those in regions with mostly diffuse sunlight. Luminescent solar concentrators are an alternative form of concentration which are stationary, potentially inexpensive, and suitable for small-scale distribution[97].

2.4.2 Luminescent solar concentrator operational principles

LSCs concentrate incident solar illumination for use in photovoltaics and other lighting applications. The original LSC, proposed in 1973 by Richard Lerner, consisted of a solution of laser dye contained between two sheets of glass but this proposal was rejected by the National Science Foundation[98]. A "planar solar collector utilizing a luminescent medium to absorb radiation, which emits light at longer wavelengths for concentration onto a semiconductor solar cell" was first reported in the literature by Weber and Lambe (1976)[99]. They discussed the fundamental advantages to the LSC approach of solar concentration: lack of solar tracking requirements; absorption of ambient light; reduced thermal load; and spectral narrowing of light, leading to the possibilities of spectral matching with coupled PV cells. The basis of LSC theory was developed by Goetzberger and Greubel in their original LSC models, in 1977[100].

Typical LSCs (Figure 2-15) consist of luminophores, commonly nanocrystals or fluorescent organic molecules, dispersed within a planar transparent waveguide. Incident light is absorbed by the luminophore and re-emitted into waveguide modes. The refractive index of the waveguide medium determines whether, for a given angle of incidence upon the medium-air interface, emitted light will be totally internally reflected or leave the waveguide via an escape cone.

The geometric ratio (*G*) is defined as the ratio of the solar cell area (the output aperture) attached to the LSC surface area absorbing sunlight (the input aperture). This is the maximum possible concentration achievable by the LSC. Naively it may be assumed that the largest gain is given by the maximum geometric ratio. This simplistic approach ignores the numerous fundamental loss mechanisms of LSCs: namely reabsorption. When the geometric gain is corrected for efficiency losses, the flux gain (*F*) is obtained. $F = G\eta_{LSC}/\eta_{PV}$ where η_{LSC} is the PCE of the concentrator under AM1.5G illumination and η_{PV} is the PCE of the cell under the LSC emission spectrum.

The price per peak Watt generated by an LSC can be calculated from its intrinsic properties as,

$$(\$/\mathrm{W_p})_{\mathrm{LSC}} = \frac{\text{collector cost}}{\mathrm{L}\eta_{\mathrm{LSC}}} + \frac{1}{\mathrm{F}}(\$/\mathrm{W_p})_{\mathrm{PV}}, \qquad (2\text{-}11)$$

where $(\$/W_p)_{PV}$ is the cost of the PV cell and L is the incident solar flux on the LSC. As the cost of the LSC decreases and collector efficiency increases, the first term becomes negligible. With cheap and efficient LSCs, the cost of PV power decreases with the geometric ratio, G.[97]

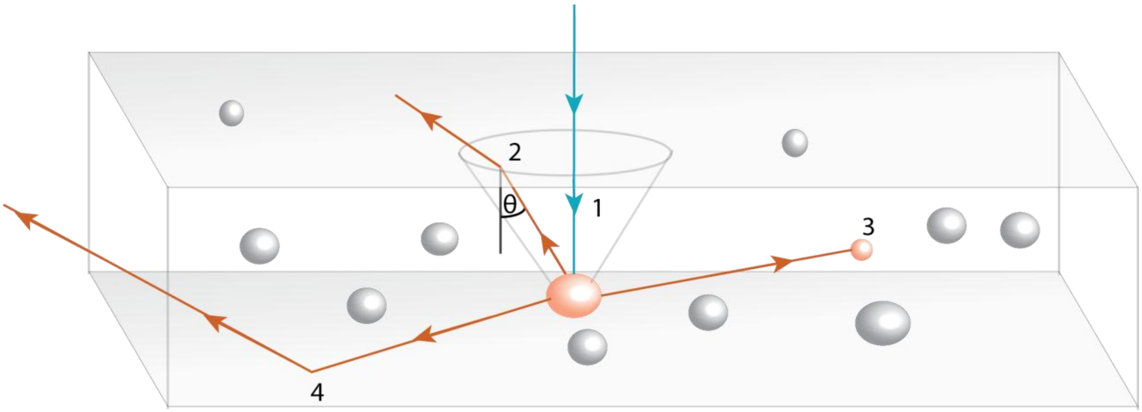

Figure 2-15: A schematic representation of total internal reflection and light trapping in a LSC. The blue ray *1* represents the path of an incident photon absorbed by the luminophore. The orange rays 2, 3 and 4 show three outcomes for a photon emitted by the luminophore. Outcome *2*: the photon is incident on the surface at less than the critical angle and couples out of the waveguide through the escape cone. Outcome 3: the photon is reabsorbed by another luminophore, the probability of this resulting in re-emission is given by the PLQE of the luminophore species. Outcome 4: the photon drives charge separation in a PV cell, as it propagates to the narrow edge the LSC since it is emitted into a waveguide mode. Efficient LSCs would maximize the fraction of photon through path 4.

After a sharp rise in LSC research following the initial development of the concept, a fall in oil prices in the 1980s paired with unstable organic dyes led to an similarly quick fall in research[101]. Recent interest in renewable energy and advances in luminophore materials[102,103] mean that LSC research is once again on the rise, and again shows potential for cost reduction in PV power generation.

2.4.3 Reabsorption losses

LSC efficiencies are currently not sufficient for commercial application. This efficiency depends on a number of inherent parameters; the waveguide refractive index, the luminophores available and proportion of wave-guided light that is reabsorbed[104]. Minimizing LSCs losses requires: minimal overlap between emitted and absorbed light (a large luminophore Stokes shift); a high luminophore PLQE; and a fully transparent supporting medium[100,105].

Overlap between the luminophore absorption and emission spectra means the chance of an emitted photon being reabsorbed is non-zero. This gives the photon more chances to be emitted into escape cones after isotropic emission from dye molecules, and if the PLQE is less than 100%, it may not be re-emitted at all. Reabsorption is a major loss mechanism for LSCs and commercial viability of LSCs necessitates that the reabsorption problem be addressed.

Increasing the Stokes shift of the luminophore may potentially mitigate the reabsorption problem, at the expense of losing some fraction of incident solar absorption. This increase can be achieved by transferring energy from an excited electronic state of one species to that of a different species with a lower-energy excited state. Thus the fluorescence can have a greater Stokes shift than if only one type of species were used. If the concentration of the final emitter is lower than the initial absorber concentration, then a high extinction coefficient can be achieved for incident light while preventing reabsorption. A potential way to achieve this desired energy transfer is Förster resonance energy transfer (FRET).

2.4.4 Förster resonance energy transfer

Energy transfer between photoactive centers can be divided into four distinct types: photon emission and reabsorption; orbital overlap (Dexter); non-radiative processes over ranges greater than the size of molecular orbitals (Förster); and in crystal systems, coherent exciton migration[106]. In Förster resonance energy transfer (FRET), energy is transferred between well-separated atomic or molecular species. A simple example is that of two atoms in a vacuum where the excitation of one leads to an excitation in the other[107]. This was first seen in a thallium and mercury vapor mixture by Cario and Frank[108]. When the mercury atomic absorption lines were excited, it was seen that both species emitted. Many molecular systems also exhibit this phenomenon[106,107,109,110].

This mechanism is distinct from radiative coupling as the energy is transferred before the sensitizer emits. FRET is highly distance dependent as it depends on the overlap between the electronic wavefunctions of both acceptor and sensitizer. The Förster model uses a dipole-dipole interaction giving an R^{-6} trend in interaction strength where R is the intermolecular distance. Higher order moments also contribute, but decay faster with distance. The rate constant of the FRET process is given by:

$$\mathrm{S}^{*} \longrightarrow \mathrm{A}^{*} = \frac{1}{\tau_{\mathrm{obs}}}\left(\frac{\mathrm{R}_0}{\mathrm{R}}\right)^6, \qquad (2\text{-}12)$$

where R_0 is the Förster critical radius, for which excitation transfer and spontaneous deactivation of the sensitizer are equally likely. τ_{obs} is the observed life time of the excited sensitizer, defined as $\tau_{obs} = \tau_0 \Phi_f$, where τ_0 is the intrinsic lifetime of the excited sensitizer, (S*) , and Φ_f is the PLQE of the sensitizer[107]. R_0 is given by

$$\mathrm{R_o}^6 = \frac{9(\ln 10)}{128\pi^5 \mathrm{N_A}} \frac{\mathrm{k}^2 \Phi_\mathrm{f}}{\mathrm{n}^4} \mathrm{J}, \qquad (2\text{-}13)$$

where N_A is Avogadro's number, n is the refractive index of the surrounding medium, κ is an orientation factor and J is the integral of the spectral overlap between sensitizer emission and acceptor absorption:

$$\mathrm{J} = \int \overline{\mathrm{f_D}}(\lambda)\epsilon_\mathrm{A}(\lambda)\lambda^4 d\lambda, \qquad (2\text{-}14)$$

where $\overline{f_D}$ is the normalised emission spectrum of the donor emission, λ is wavelength, and $\epsilon_A$is the acceptor molar extinction coefficient. The orientation factor, k, is given by,

$$\mathrm{k} = cos\phi_{SA} - 3cos\phi_S . cos\phi_A , \qquad (2\text{-}15)$$

where ϕ_{SA} is the angle between the transition dipole moments of both molecules, while ϕ_S and ϕ_A are the angles between the dipole moments and the displacement vector from sensitizer to acceptor.

By choosing the correct luminophores in close proximity, higher energy light can be converted to lower energy light. Roberts *et al.*[111] demonstrated this when they embedded six different dyes with suitably overlapping absorption and emission spectra to cover most of the visible spectrum in a polystyrene sphere. Upon excitation at 480 nm the peak emission from the sphere was seen at 720 nm corresponding to the emission of the lowest energy emitting dye. Converting the whole visible spectrum to a long wavelength would be a natural continuation of this work. Recently work by Bailey *et al.*[103] made LSCs with three boron-dipyrromethene dyes demonstrating that the spectral range over which sunlight may be absorbed increased 45-170 % compared to LSCs with only one dye. The FRET mechanism is strongly affected by distance between chromophores. At the high concentrations required for FRET, in a LSC, reabsorption plays a dominate role. Thus, a mechanism allowing chromophores to be close to each other, without high overall concentrations, has been the subject of much research. This relates directly to reabsorption, as the amount of reabsorption increases greatly when the concentration is at a level that allows efficient FRET.

2.4.5 Photo-active antenna complexes

The replication of bacterial phycobilisomes one possible method to achieve the high local concentration required to enable FRET[102]. Phycobilisomes are complexes of biliproteins and linker polypetides, which produce rapid and directional energy transport to chlorophyll A in the thylakoid membrane.[112] The biliproteins are grouped into three types by their energies; high energy (phycoerythrins), intermediate energy (phycocyanins) and low energy (allophycocyanins). Absorbed energy is transferred from the outer, higher energy biliproteins to the core of lower energy biliproteins, where it is re-emitted into the thylakoid membrane[112]. This produces effective light harvesting and energy migration into a photoreceptive region by directed energy transfer (Figure 2-16). Imitating phycobilisomes may lead to the creation of structures that can hold dyes in close proximity together without necessitating high, homogeneous, concentrations. Significantly reduced reabsorption losses have been shown by the direct use of phycobilisomes in LSC devices[102]. Therefore phycobilisomes are not only an efficient light harvesting system applicable to LSCs, but also a blueprint for more specific synthetic systems. Figure 2-16 shows the generalized structure of phycobilisomes as a few central emitter molecules with radial absorbing antennae.

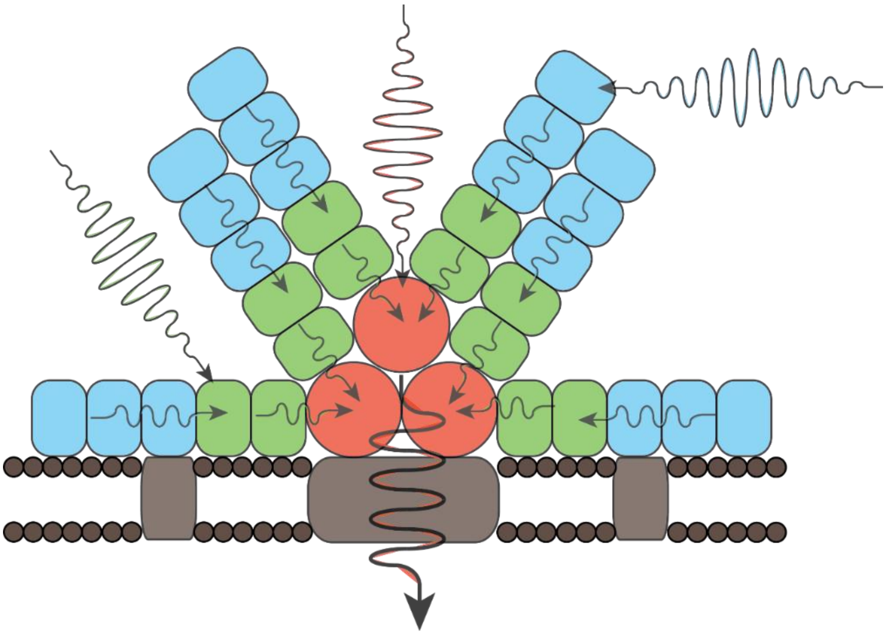

Figure 2-16: Schematic phycobilisome structure Indicating absorption of incident photons and FRET through the phycoerythrins, in blue, phycocyanins, in green, and allophycocyanins, in red, to the thylakoid membrane (grey.)

2.5 Light-Emitting Diodes

2.5.1 Light-emitting diode operational principles

LEDs operate though the injection of electrons and holes which radiatively recombine to emit photons. The energy of photons emitted from a LED is defined by the quasi fermi energy of the injected electrons and holes, usually limited by E_g. In an ideal diode, all electrons injected into an active region will generate a photon. The ideal LED has a quantum efficiency of unity. The internal quantum efficiency is defined as

$$\eta_{\mathrm{int}} = \frac{\text{number of photons emitted from active region } (\mathrm{s}^{-1})}{\text{current in the external circuit}} = \frac{P_{\mathrm{int}}/(h\nu)}{I/e}, \qquad (2\text{-}16)$$

where P_{int} is the optical power emitted from the active region and I is the injection current. In an ideal LED all photons emitted from the active layer are emitted into free space and thus the extraction efficiency is unity[13]. Due to various loss pathways this not always the case; photons may be absorbed by the substrate or electrodes and light may become trapped into waveguide modes reducing its ability to escape from the LED.

Photon extraction efficiency can severely limit LED performance, and in general extraction efficiencies above 50% are not possible without resorting to sophisticated and complex structures. Thus the external quantum efficiency is defined as

$$\eta_{\mathrm{ext}} = \frac{\text{number of photons emitted from into free space } (\mathrm{s}^{-1})}{\text{current in the external circuit}} = \frac{\mathrm{P}/(\mathrm{h}\nu)}{\mathrm{I}/\mathrm{e}} \,. \qquad (\text{2-17})$$

Overall power efficiency is defined as $\eta_{power} = P/IV$, where IV is the electrical power provided to the LED[13]. The refractive index contrast between the light-emitting material and the surround material leads to a non-isotropic emission pattern. In the case of high index light-emitting materials with a planar surface a Lambertian emission pattern is obtained. The Lambertian emission pattern follows a cosine dependence on the angle φ. The intensity is highest for emission normal to the LED surface and at an angle of 60° it decreased to half of its maximum value[13].

The human eye contains photoreceptive cells capable of perceiving red, blue and green light. As such, the eye's response to visible light is wavelength dependent. Since the eye is generally the recipient of LED applications adjustments in photometric measurements have to be made in relevance to the human eye. The luminous flux (in units of lumen) represents the light power of a source perceived by the eye (which is wavelength dependent) and is defined as a monochromatic light source emitting an optical power of 1/683 Watt at 555 nm has a luminous flux of 1 lumen (lm). The luminous intensity (in units of candela (cd)) represents the light intensity as perceived by the eye. A monochromatic light source emitting an optical power of 1/683 Watt at 555 nm into the solid angle of 1 steradian (sr) has a luminous intensity of 1 candela (cd)[13].

2.5.2 Nanocrystal light-emitting diodes

Electro-luminescent devices have been developed based on many type III-V semiconductors[13], porous silicon [113], organics[114] and semiconducting polymers[115]. Due to the optical properties of colloidal nanocrystals they are seen as potential candidate materials for LEDs. Specifically, their tunable narrow emission offers the potential for high color quality lighting applications. In QD-LEDs electroluminescence is usually driven by direct charge injection, an electron and a hole are injected from charge transport layers (CTLs) into a QD, forming an exciton that subsequently recombines to emit a photon[116] (Figure 2-17).

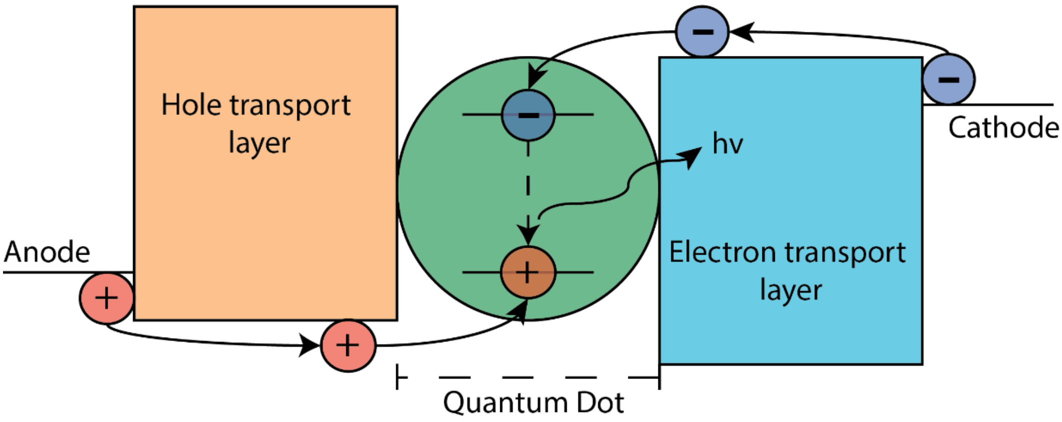

Figure 2-17: Operational schematic of a QD-LED. The electron and holes recombine into the QD resulting in the emission of a photon.

Quantum dot LEDs (QD-LEDS) are LEDS that use QDs as the light-emitting layer have undergone extensive developed since they were first developed in the mid 90s[117–119]. Colloidal quantum dots are solution processable which facilities a variety of low cost and large-area deposition techniques([120–124]). Initially QD-LEDs were similar in structure to polymer LEDs, being comprised of CdSe core-only QDs between two electrodes. Electroluminescence was achieved in these devices with extremely low EQEs (<0.01% at around 100 cd m^{-2}). These low efficiencies were party due to the low PLQE of the quantum dots, and a consequence of the very low current densities achievable by using insulating QDs as both charge transport and emissive materials[125]. Over the subsequent decades QDs became more complex, and core shell structures were employed to improve PLQE[126–131]. Notably, core-shell CdSe QDs were later employed as the emission material and due to the increased PLQE these devices produced EQEs up to 0.22% (maximum of 600 cd m^{-2})[118]. By decoupling the luminance process from charge transport through organic layers, with the insertion of a monolayer of QDs at the interface of polymer bilayer LEDs, new devices demonstrated EQEs of 0.5%[121,132–137]. Consequently, the fabrication and patterning of a closely packed QD monolayer became important to enhance the efficiency of QD-LEDs[125]. Replacing the organic CTLs with inorganic CTLs led to devices with greater air stability and allowed the passage of higher current densities[132]. An alternative to organic CTLs are sputtered metal oxide films which can be deposited at room temperature[138]. Although this allows devices to operate at higher current densities, the EQEs are generally <0.1%[125]. This inefficiency is generally attributed to damage of the QDs during sputtering of the overlying metal oxide[139]. More recent devices employ hybrid architectures comprising of both organic and inorganic CTLS. Typically, the n-type semiconductor is a metal oxide while the p-type layer is an organic semiconductor. Devices with these architectures have seen high EQEs 0.22%-18% with maximum brightness values ranging between 2200 – 218000 cd m^{-2} [140,141].

2.5.3 Lead halide perovskites semiconductors

Metal halide perovskite semiconductors have recently shown outstanding optoelectronic characteristics such as low cost solution processability[142–145], high mobility[146–148], bright emission[149] and tuneable band gap and luminescence[150–152]. Indeed hybrid organic-inorganic lead halides $MAPbX_3$ (MA = CH_3NH_3, X = Cl, Br and I) have seen encouraging development as inexpensive absorber layers in solar cells with conversion efficiencies exceeding 20%[153–156], solution cast photodetectors for the visible, ultraviolet and X-ray regions of the spectrum[157–161], gain media for optically pumped lasers[151,162–166] and emission layers for LEDs[149,167–169].

It's been shown that the use of methyl ammonium halides in perovskite materials is one of the limiting factors of their thermal and operational stability[170]. By replacing the organic MA with inorganic cesium, to produce all inorganic $CsPbX_3$ (X = Cl, Br, I), the thermal stability of the perovskite is increased to $\approx 500^{o}$C[171], although this decreases the solution processability compared to the hybrid organic-inorganic $MAPBX_3$[172].

While the majority of recent research has focused on thin film and bulk materials[145,153–155,173,174], Perovskite nanocrystals have only recently been synthesised. This includes hybrid organic-inorganic $MAPbX_3$ nanocrystals and nanostructures[175] and all inorganic caesium lead halide $CsPbX_3$ (X = Cl, Br, I), caesium tin halide $CsSnX_3$ (X = Cl, Br, I), nanocrystals and nanostructures[176–178] The move to colloidal semiconductor quantum dots not only improves solution processability of these materials but also allows size tunabilty due to the 3D confinement effect[175,179] and creates a material that is ready miscible with other optoelectronic materials eg. Polymers, fullerene and other nanomaterials. These cesium lead halide perovskite nanocrystals have shown to have near unity quantum yields without the need for core shell structures and can be synthesized in a one pot synthesis to produce colors over the visible spectrum by changing the halide composition (Figure 2-18)[180,181]. Thus they represent a new potential emission material for LEDs.

Figure 2-18: Cesium lead halide perovskite nanocrystals. Color change comes from changing the halide compositing: far left sample = $CsPbCl_3$, Middle sample = $CsPbBr_3$ and far right sample = $CsPbI_3$. Other colors come from different rations of Cl:Br or Br:I.

2.6 References

(1) Piprek, J. *Semiconductor Optoelectronic Devices- Introduction to Physics and Simulation*; Academic Press: San Diego, 2003.

(2) Green, M. A. *Solar Cells - Operating Principles, Technology and System Applications*; University of New South Wales: Sydney, 1992.

(3) Nelson, J. *The Physics of Solar Cells*; Imperial College Press: London, 2003.

(4) Young, H. D.; Freedman, R. A.; Ford, L. A. *Sears and Zemansky's University Physics: with Modern Physics*; 13th ed.; Addison-Wesley: San Francisco, 2012.

(5) Carsten, D.; Vladimir, D. *Reports Prog. Phys.* **2010**, *73*, 96401.

(6) Alivisatos, A. P. *Adv. Sci.* **1996**, *271*, 933–937.

(7) Kuder, S.; Carbone, L.; Manna, L.; Parak, W. J. In *Semicoductor Nanocrystal Quantum Dots*; 2008; pp. 1–34.

(8) Efros, A.; Rosen, M. *Annu. Rev. Mater. Sci.* **2000**, 475–521.

(9) Klimov, V. *J. Phys. Chem. B* **2006**, 16827–16845.

(10) Ramaniah, L.; Nair, S. *Phys. B Condens. Matter* **1995**, *212*, 245–250.

(11) Tang, J.; Sargent, E. H. *Adv. Mater.* **2011**, *23*, 12–29.

(12) Schubert, E. F. *Doping in III–V Semiconductors*; Ahmed, H.; Pepper, M.; Broers, A., Eds.; Cambridge University Press: New York, 1993.

(13) Schubert, E. F. *Light-Emitting Diodes*; Second.; Cambridge University Press: New York, 2006.

(14) Hines, M. A.; Scholes, G. D. *Adv. Mater.* **2003**, *15*, 1844–1849.

(15) Murray, C. *Annu. Rev. Mater. Sci.* **2000**, 545–610.

(16) Chen, O.; Chen, X.; Yang, Y.; Lynch, J.; Wu, H.; Zhuang, J.; Cao, Y. C. *Angew. Chem. Int. Ed. Engl.* **2008**, *47*, 8638–8641.

(17) Rogach, A. L. *Semiconductor Nanocrstal Quatum Dots*; SpringerWienNewYork, 2008.

(18) Bae, W. K.; Joo, J.; Padilha, L. A.; Won, J.; Lee, D. C.; Lin, Q.; Koh, W.; Luo, H.; Klimov, V. I.; Pietryga, J. M. *J. Am. Chem. Soc.* **2012**, *134*, 20160–20168.

(19) Padilha, L. A.; Stewart, J. T.; Sandberg, R. L.; Bae, W. K.; Koh, W.-K.; Pietryga, J. M.; Klimov, V. I. *Nano Lett.* **2013**, *13*, 1092–1099.

(20) Wanger, D. D.; Correa, R. E.; Dauler, E. A.; Bawendi, M. G. *Nano Lett.* **2013**, *13*, 5907–5912.

(21) Schaller, R.; Klimov, V. *Phys. Rev. Lett.* **2004**, *92*, 186601.

(22) Midgett, A.; Luther, J.; Stewart, J. *Nano Lett.* **2013**, *13*, 3078–3085.

(23) Kaito, C.; Saito, Y.; Fujita, K. *Jpn. J Appl. Phys.* **1987**, *26*, L1973–L1975.

(24) Wang, W.; Liu, Y.; Zhan, Y.; Zheng, C.; Wang, G. *Mater. Res. Bull.* **2001**, *36*, 1977–1984.

(25) Wang, S.; Yang, S. *Langmuir* **2000**, 389–397.

(26) Borrelli, N.; Smith, D. *J. Non. Cryst. Solids* **1994**, *180*, 25–31.

(27) Gong, J.; Zhang, Z.; Bai, H.; Yang, G. *Sci. China Ser. E Technol. Sci.* **2007**, *50*, 302–307.

(28) Peng, X.; Manna, L.; Yang, W.; Wickham, J.; Scher, E.; Kadavanich, A.; Alivisatos, A. *Nature* **2000**, *404*, 59–61.

(29) Sitt, A.; Hadar, I.; Banin, U. *Nano Today* **2013**, *8*, 494–513.

(30) Penn, R. L. *Science* **1998**, *281*, 969–971.

(31) Cho, K.-S.; Talapin, D. V; Gaschler, W.; Murray, C. B. *J. Am. Chem. Soc.* **2005**, *127*, 7140–7147.

(32) Koh, W.; Bartnik, A. C.; Wise, F. W.; Murray, C. B. *J. Am. Chem. Soc.* **2010**, *132*, 3909–3913.

(33) American Society for Testing and Materials. *Astm Int.* **2013**, *03*, 1–21.

(34) Streetman, B. G.; Banerjee, S. K. *Solid State Electronic Devices*; 6th ed.; Pearson Prentice Hall: New Jersey, 2006.

(35) Sargent, E. H. *Nat. Photonics* **2009**, *3*, 325–331.

(36) Hamaker, H. C.; Ford, C. W.; Werthen, J. G.; Virshup, G. F.; Kaminar, N. R.; King, D. L.; Gee, J. M. *Appl. Phys. Lett.* **1985**, *47*, 762.

(37) Shockley, W.; Queisser, H. J. *J. Appl. Phys.* **1961**, *32*, 510.

(38) Green, M. A. *Sol. Energy* **2004**, *76*, 3–8.

(39) Bar, M.; Wilks, R. G.; M., R.; Gerlach, D.; Ruske, F.; Lips, K.; Rech, B.; Weinhardt, L.; Blum, M.; Pookpanratana, S.; Krause, S.; Zhang, Y.; Heske, C.; Yang, W.; Denlinger, J. D. *Appl. Phys. Lett.* **2010**, *97*, 072105.

(40) Archer, M. D.; Nozik, A. J. *Nanostructured and Photoelectrochemical System for Solar Photon Conversion*; Imperial College Press, 2008.

(41) Keevers, M. J.; Young, T. L.; Schubert, U.; Green, M. A. *Proc. 22nd Eur. Photovolt. Sol. Energy Conf.* **2009**.

(42) National Renewable Energy Laboratory. *Best Research-Cell Efficiencies*; U.S. Department of Energy, 2016.

(43) Tobin, S. P.; Vernon, S. M.; Bajgar, C.; Haven, V. E.; Geoffroy, L. M.; Lillington, D. R. *IEEE Trans. Electron Devices* **1988**, *9*, 256–258.

(44) Wojtczuk, S.; Tobin, S.; Sanfacon, M.; Haven, V.; Geoffroy, L.; Vernon, S. *Photovolt. Spec. Conf. 1991., Conf. Rec. Twenty Second IEEE* **1991**, 73–79.

(45) Loferski, J. J. *Prog. Photovoltaics Res. Appl.* **1993**, *1*, 67–78.

(46) Hirst, L. C.; Ekins-daukes, N. J. *Prog. Photovoltaics Res. Appl.* **2011**, 286–293.

(47) Brown, G. F.; Wu, J. *Laser Photonics Rev.* **2009**, *3*, 394–405.

(48) Law, M.; Luther, J. M.; Song, Q.; Hughes, B. K.; Perkins, C. L.; Nozik, A. J. *J. Am. Chem. Soc.* **2008**, *130*, 5974–5985.

(49) Pietryga, J. M.; Werder, D. J.; Williams, D. J.; Casson, J. L.; Schaller, R. D.; Klimov, V. I.; Hollingsworth, J. A. *J. Am. Chem. Soc.* **2008**, *130*, 4879–4885.

(50) Chuang, C.; Brown, P.; Bulović, V.; Bawendi, M. *Nat. Mater.* **2014**, 1–6.

(51) Yoon, W.; Boercker, J. E.; Lumb, M. P.; Placencia, D.; Foos, E. E.; Tischler, J. G. *Sci. Rep.* **2013**, *3*, 2225.

(52) McBride, J.; Pennycook, T. *ACS Nano* **2013**, 8358–8365.

(53) Gur, I.; Fromer, N. A.; Geier, M. L.; Alivisatos, A. P. *Science* **2005**, *310*, 462–465.

(54) Ip, A. H.; Thon, S. M.; Hoogland, S.; Voznyy, O.; Zhitomirsky, D.; Debnath, R.; Levina, L.; Rollny, L. R.; Carey, G. H.; Fischer, A.; Kemp, K. W.; Kramer, I. J.; Ning, Z.; Labelle, A. J.; Chou, K. W.; Amassian, A.; Sargent, E. H. *Nat. Nanotechnol.* **2012**, *7*, 577–582.

(55) Luther, J. M.; Law, M.; Song, Q.; Perkins, C. L.; Beard, M. C.; Nozik, A. J. *ACS Nano* **2008**, *2*, 271–280.

(56) Goncher, G.; Solanki, R. *Proc. SPIE* **2008**, *7047*, 70470L – 70470L – 14.

(57) Sun, B.; Snaith, H. J.; Dhoot, A. S.; Westenhoff, S.; Greenham, N. C. *J. Appl. Phys.* **2005**, *97*, 014914.

(58) Sun, B.; Marx, E.; Greenham, N. C. *Nano Lett.* **2003**, 5–7.

(59) Sun, B.; Greenham, N. C. *Phys. Chem. Chem. Phys.* **2006**, *8*, 3557–3560.

(60) Werner, J.; Kolodinski, S.; Queisser, H. *Phys. Rev. Lett.* **1994**, *72*, 3851–3854.

(61) Padilha, L. A.; Stewart, J. T.; Sandberg, R. L.; Bae, W. K.; Koh, W.-K.; Pietryga, J. M.; Klimov, V. I. *Acc. Chem. Res.* **2013**, *46*, 1261–1269.

(62) Semonin, O. E.; Luther, J. M.; Choi, S.; Chen, H.-Y.; Gao, J.; Nozik, A. J.; Beard, M. C. *Science* **2011**, *334*, 1530–1533.

(63) Nozik, A. J. *Annu. Rev. Phys. Chem.* **2001**, 193–231.

(64) Rupasov, V.; Klimov, V. *Phys. Rev. B* **2007**, *76*, 125321.

(65) McGuire, J. A.; Sykora, M.; Joo, J.; Pietryga, J. M.; Klimov, V. I. *Nano Lett.* **2010**, *10*, 2049–2057.

(66) Stewart, J. T.; Padilha, L. A.; Qazilbash, M. M.; Pietryga, J. M.; Midgett, A. G.; Luther, J. M.; Beard, M. C.; Nozik, A. J.; Klimov, V. I. *Nano Lett.* **2012**, *12*, 622–628.

(67) Schaller, R. D.; Agranovich, V. M.; Klimov, V. I. *Nat. Phys.* **2005**, *1*, 189–194.

(68) Beard, M. C.; Ellingson, R. J. *Laser Photonics Rev.* **2008**, *2*, 377–399.

(69) Nozik, A. J. *J. Chem. Phys. Lett.* **2008**, *457*, 3–11.

(70) Binks, D. J. *Phys. Chem. Chem. Phys.* **2011**, *13*, 12693–12704.

(71) Smith, C.; Binks, D. *Nanomaterials* **2013**, *4*, 19–45.

(72) Stewart, J. T.; Padilha, L. A.; Bae, W. K.; Koh, W.-K.; Pietryga, J. M.; Klimov, V. I. *J. Phys. Chem. Lett.* **2013**, *4*, 2061–2068.

(73) McGuire, J. A.; Joo, J.; Pietryga, J. M.; Schaller, R. D.; Klimov, V. I. *Acc. Chem. Res.* **2008**, *41*, 1810–1819.

(74) Schaller, R. D.; Petruska, M. a.; Klimov, V. I. *Appl. Phys. Lett.* **2005**, *87*, 253102.

(75) Schaller, R. D.; Pietryga, J. M.; Klimov, V. I. *Nano Lett.* **2007**, *7*, 3469–3476.

(76) Cunningham, P. D.; Boercker, J. E.; Foos, E. E.; Lumb, M. P.; Smith, A. R.; Tischler, J. G.; Melinger, J. S. *Nano Lett.* **2013**, *13*, 3003–3003.

(77) Davis, N. J. L. K.; Böhm, M. L.; Tabachnyk, M.; Wisnivesky-Rocca-Rivarola, F.; Jellicoe, T. C.; Ducati, C.; Ehrler, B.; Greenham, N. C. *Nat. Commun.* **2015**, *6*, 8259.

(78) Sandeep, C. S. S.; ten Cate, S.; Schins, J. M.; Savenije, T. J.; Liu, Y.; Law, M.; Kinge, S.; Houtepen, A. J.; Siebbeles, L. D. A. *Nat. Commun.* **2013**, *4*, 2360–2366.

(79) Beard, M. C.; Midgett, A. G.; Hanna, M. C.; Luther, J. M.; Hughes, B. K.; Nozik, A. J. *Nano Lett.* **2010**, *10*, 3019–3027.

(80) Bertazzi, F.; Moresco, M.; Penna, M.; Goano, M.; Bellotti, E. *J. Electron. Mater.* **2010**, *39*, 912–917.

(81) Tirino, L.; Weber, M.; Brennan, K. F.; Bellotti, E.; Goano, M. *J. Appl. Phys.* **2003**, *94*, 423–430.

(82) Ziaja, B.; London, R. A.; Hajdu, J. *J. Appl. Phys.* **2006**, *99*.

(83) Hanna, M. C.; Nozik, A. J. *J. Appl. Phys.* **2006**, *100*, 074510.

(84) Klimov, V. I. *Appl. Phys. Lett.* **2006**, *89*, 123118.

(85) Sandberg, R. L.; Padilha, L. A.; Qazilbash, M. M.; Bae, W. K.; Schaller, R. D.; Pietryga, J. M.; Stevens, M. J.; Baek, B.; Nam, S. W.; Klimov, V. I. *ACS Nano* **2012**, *6*, 9532–9540.

(86) Trinh, M. T.; Houtepen, A. J.; Schins, J. M.; Hanrath, T.; Piris, J.; Knulst, W.; Goossens, A. P. L. M.; Siebbeles, L. D. A. *Nano Lett.* **2008**, *8*, 1713–1718.

(87) Beard, M. C.; Midgett, A. G.; Law, M.; Semonin, O. E.; Ellingson, R. J.; Nozik, A. J. *Nano Lett.* **2009**, *9*, 836–845.

(88) Sashchiuk, A.; Yanover, D.; Rubin-Brusilovski, A.; Maikov, G. I.; Čapek, R. K.; Vaxenburg, R.; Tilchin, J.; Zaiats, G.; Lifshitz, E. *Nanoscale* **2013**, *5*, 7724–7745.

(89) Bartnik, A. C.; Efros, A. L.; Koh, W.-K.; Murray, C. B.; Wise, F. W. *Phys. Rev. B* **2010**, *82*, 195313.

(90) Achermann, M.; Hollingsworth, J. A.; Klimov, V. I. *Phys. Rev. B* **2003**, *68*, 1–5.

(91) Li, L.; Hu, J.; Yang, W.; Alivisatos, A. P. *Nano Lett.* **2001**, *1*, 349–351.

(92) Fabre, E.; Mautref, M.; Mircea, A. *Appl. Phys. Lett.* **1975**, *27*, 239.

(93) Ohtsuka, H.; Kitatani, T.; Yazawa, Y.; Warabisako, T. *Sol. Energy Mater. Sol. Cells* **1998**, *50*, 251–257.

(94) Ragay, F. W.; Marti, A.; Araujo, G. L.; Wolter, J. H. *Sol. Energy Mater. Sol. Cells* **1996**, *40*, 5–21.

(95) Rau, U.; Kirchartz, T. *Nat. Publ. Gr.* **2014**, *13*, 103–104.

(96) Laque, A.; Hengedus, S. *Handbook of Photovoltaic Science and Engineering*; John Wiley & Sons, 2003.

(97) Currie, M. J.; Mapel, J. K.; Heidel, T. D.; Goffri, S.; Baldo, M. A. *Science* **2008**, *321*, 226–228.

(98) Batchelder, J. S.; Zewail, A. H.; Cole, T. *Appl. Opt.* **1979**, *18*, 3090–3110.

(99) Weber, W. H.; Lambe, J. *Appl. Opt.* **1976**, *15*, 2299–2300.

(100) Goetzberger, A.; Greubel, W. *Appl. Phys.* **1977**, *14*, 123–139.

(101) Debije, M. G.; Verbunt, P. P. C. *Adv. Energy Mater.* **2012**, *2*, 12–35.

(102) Mulder, C. L.; Theogarajan, L.; Currie, M.; Mapel, J. K.; Baldo, M. A.; Vaughn,

M.; Willard, P.; Bruce, B. D.; Moss, M. W.; McLain, C. E.; Morseman, J. P. *Adv. Mater.* **2009**, *21*, 3181–3185.

(103) Bailey, S. T.; Lokey, G. E.; Hanes, M. S.; Shearer, J. D. M.; McLafferty, J. B.; Beaumont, G. T.; Baseler, T. T.; Layhue, J. M.; Broussard, D. R.; Zhang, Y.-Z.; Wittmershaus, B. P. *Sol. Energy Mater. Sol. Cells* **2007**, *91*, 67–75.

(104) van Sark, W. G. J. H. M. *Renew. Energ.* **2012**, 1–4.

(105) Baur, G.; Greubel, W. *Appl. Phys. Lett.* **1977**, *31*, 4–6.

(106) Livingston, R. *J. Phys. Chem.* **1951**, *61*, 860–864.

(107) Förster, T. *Discuss. Faraday Soc.* **1959**, *27*, 7–17.

(108) Cario, G.; Franck, J. *Zeitschrift für Phys. A Hadron. Nucl.* **1922**, *11*, 161–166.

(109) Schlosser, M.; Lochbrunner, S. *J. Phys. Chem. B* **2006**, *110*, 6001–6009.

(110) Braslavsky, S. E.; Fron, E.; Rodríguez, H. B.; Román, E. S.; Scholes, G. D.; Schweitzer, G.; Valeur, B.; Wirz, J. *Photochem. Photobiol. Sci.* **2008**, *7*, 1444–1448.

(111) Roberts, D. V; Wittmershaus, B. P.; Zhang, Y.-Z.; Swan, S.; Klinosky, M. P. *J. Lumin.* **1998**, *79*, 225–231.

(112) MacColl, R. *J. Struct. Biol.* **1998**, *124*, 311–334.

(113) Bsiesy, A.; Muller, F.; Ligeon, M.; Gaspard, F.; Herino, R.; Romestain, R.; Vial, J. C. *Phys. Rev. Lett.* **1993**, *71*, 637–640.

(114) Burroughes, J. H.; Bradley, D. D. C.; Brown, A. R.; Marks, R. N.; Mackay, K.; Friend, R. H.; Burns, P. L.; Holmes, A. B. *Nature* **1990**, *347*, 539–541.

(115) Greenham, N. C.; Moratti, S. C.; Bradley, D. D. C.; Friend, R. H.; Holmes, A. B. *Nature* **1993**, *365*, 628–630.

(116) Shirasaki, Y.; Supran, G. J.; Bawendi, M. G.; Bulović, V. *Nat. Photonics* **2013**, *7*, 13–23.

(117) Colvin, V. L.; Schlamp, M. C.; Alivisatos, a P. *Nature* **1994**, *370*, 354–357.

(118) Schlamp, M. C.; Peng, X.; Alivisatos, a P. *J. Appl. Phys.* **1997**, *5837*, 5837–5842.

(119) Dabbousi, B. O.; Bawendi, M.; Onitsuka, O.; Rubner, M. F. *Appl. Phys. Lett.* **1995**, *66*, 1316–1318.

(120) Wood, V.; Bulović, V. *Nano Rev.* **2010**, *1*, 1–7.

(121) Coe, S.; Woo, W.-K.; Bawendi, M.; Bulovic, V. *Nature* **2002**, *420*, 3–6.

(122) Tekin, E.; Smith, P. J.; Hoeppener, S.; Van Den Berg, A. M. J.; Susha, A. S.; Rogach, A. L.; Feldmann, J.; Schubert, U. S. *Adv. Funct. Mater.* **2007**, *17*, 23–28.

(123) Wood, V.; Panzer, M. J.; Chen, J.; Bradley, M. S.; Halpert, J. E.; Bawendi, M. C.; Bulovic, V. *Adv. Mater.* **2009**, *21*, 2151–2155.

(124) Kim, L.; Anikeeva, P. O.; Coe-Sullivan, S. A.; Steckel, J. S.; Bawendi, M. G.; Bulović, V. *Nano Lett.* **2008**, *8*, 4513–4517.

(125) Shirasaki, Y.; Supran, G. J.; Bawendi, M. G.; Bulović, V. *Nat. Photonics* **2013**, *7*, 13–23.

(126) Mattoussi, H.; Radzilowski, L. H.; Dabbousi, B. O.; Thomas, E. L.; Bawendi, M. G.; Rubner, M. F. *J. Appl. Phys.* **1998**, *83*, 7965.

(127) Yang, Y.; Zheng, Y.; Cao, W.; Titov, A.; Hyvonen, J.; Manders, J. R.; Xue, J.; Holloway, P. H.; Qian, L. *Nat. Photonics* **2015**, *9*, 1–9.

(128) Nizamoglu, S.; Ozel, T.; Sari, E.; Demir, H. V. *Nanotechnology* **2007**, *18*, 065709.

(129) Shen, H.; Bai, X.; Wang, A.; Wang, H.; Qian, L.; Yang, Y.; Titov, A.; Hyvonen, J.; Zheng, Y.; Li, L. S. *Adv. Funct. Mater.* **2014**, *24*, 2367–2373.

(130) Ji, W.; Jing, P.; Xu, W.; Yuan, X.; Wang, Y.; Zhao, J.; Jen, A. K. Y. *Appl. Phys. Lett.* **2013**, *103*.

(131) Lin, Q.; Song, B.; Wang, H.; Zhang, F.; Chen, F.; Wang, L.; Guo, F.; Li, L. S.; Shen, H. *J. Mater. Chem. C* **2016**.

(132) Mueller, A. H.; Petruska, M. A.; Achermann, M.; Werder, D. J.; Akhadov, E. A.; Koleske, D. D.; Hoffbauer, M. A.; Klimov, V. I. *Nano Lett.* **2005**, *5*, 1039–1044.

(133) Panzer, M. J.; Aidala, K. E.; Anikeeva, P. O.; Halpert, J. E.; Bawendi, M. G.; Bulovic, V. *Nano Lett.* **2010**, *10*, 2421–2426.

(134) Achermann, M.; Petruska, M. A.; Koleske, D. D.; Crawford, M. H.; Klimov, V. I. *Nano Lett.* **2006**, *6*, 1396–1400.

(135) Achermann, M.; Petruska, M. A.; Kos, S.; Smith, D. L.; Koleske, D. D.; Klimov, V. I. *Nature* **2004**, *429*, 642–646.

(136) Steckel, J. S.; Snee, P.; Coe-Sullivan, S.; Zimmer, J. P.; Halpert, J. E.; Anikeeva, P.; Kim, L. A.; Bulovic, V.; Bawendi, M. G. *Angew. Chemie - Int. Ed.* **2006**, *45*, 5796–5799.

(137) Anikeeva, P.; Madigan, C.; Halpert, J.; Bawendi, M.; Bulović, V. *Phys. Rev. B* **2008**, *78*, 1–8.

(138) Caruge, J. M.; Halpert, J. E.; Wood, V.; Bulović, V.; Bawendi, M. G. *Nat. Photonics* **2008**, *2*, 247–250.

(139) Wood, V.; Panzer, M. J.; Halpert, J. E.; Caruge, J. M.; Bawendi, M. G.; Bulovic, V. *ACS Nano* **2009**, *3*, 3581–3586.

(140) Qian, L.; Zheng, Y.; Xue, J.; Holloway, P. H. *Nat. Photonics* **2011**, *5*, 543–548.

(141) Kwak, J.; Bae, W. K.; Lee, D.; Park, I.; Lim, J.; Park, M.; Cho, H.; Woo, H.; Yoon, D. Y.; Char, K.; Lee, S.; Lee, C. *Nano Lett.* **2012**, *12*, 2362–2366.

(142) Kojima, A.; Teshima, K.; Shirai, Y.; Miyasaka, T. *J. Am. Chem. Soc.* **2009**, *131*,

6050–6051.

(143) Lee, M.; Teuscher, J.; Miyasaka, T. *Science* **2012**, *338*, 643–648.

(144) Burschka, J.; Pellet, N.; Moon, S.-J.; Humphry-Baker, R.; Gao, P.; Nazeeruddin, M. K.; Grätzel, M. *Nature* **2013**, *499*, 316–319.

(145) Nie, W.; Tsai, H.; Asadpour, R. *Science* **2015**, *347*, 522–525.

(146) Stranks, S.; Eperon, G.; Grancini, G. *Science* **2013**, *342*, 341–345.

(147) Xing, G.; Mathews, N.; Sun, S.; Lim, S. *Science* **2013**, *342*, 498–500.

(148) Dong, Q.; Fang, Y.; Shao, Y.; Mulligan, P. *Science* **2015**, *347*, 967–970.

(149) Tan, Z.-K.; Moghaddam, R. S.; Lai, M. L.; Docampo, P.; Higler, R.; Deschler, F.; Price, M.; Sadhanala, A.; Pazos, L. M.; Credgington, D.; Hanusch, F.; Bein, T.; Snaith, H. J.; Friend, R. H. *Nat. Nanotechnol.* **2014**, *9*, 687–692.

(150) Zhang, W.; Anaya, M.; Lozano, G.; Calvo, M. E.; Johnston, M. B.; Míguez, H.; Snaith, H. J. *Nano Lett.* **2015**, *15*, 1698–1702.

(151) Xing, G.; Mathews, N.; Lim, S. S.; Yantara, N.; Liu, X.; Sabba, D.; Grätzel, M.; Mhaisalkar, S.; Sum, T. C. *Nat. Mater.* **2014**, *13*, 476–480.

(152) Filip, M. R.; Eperon, G. E.; Snaith, H. J.; Giustino, F. *Nat. Commun.* **2014**, *5*, 5757–5766.

(153) Green, M. A.; Ho-Baillie, A.; Snaith, H. J. *Nat. Photonics* **2014**, *8*, 506–514.

(154) Park, N. *J. Phys. Chem. Lett.* **2013**, *4*, 2425–2429.

(155) Zhou, H.; Chen, Q.; Li, G.; Luo, S.; Song, T. *Science* **2014**, *365*, 542–546.

(156) Jeon, N. J.; Noh, J. H.; Yang, W. S.; Kim, Y. C.; Ryu, S.; Seo, J.; Seok, S. Il. *Nature* **2015**, *517*, 476–480.

(157) Dou, L.; Yang, Y. M.; You, J.; Hong, Z.; Chang, W.-H.; Li, G.; Yang, Y. *Nat. Commun.* **2014**, *5*, 5404.

(158) Guo, Y.; Liu, C.; Tanaka, H.; Nakamura, E. *J. Phys. Chem. Lett.* **2015**, *6*, 535–539.

(159) Yakunin, S.; Sytnyk, M.; Kriegner, D.; Shrestha, S.; Richter, M.; Matt, G. J.; Azimi, H.; Brabec, C. J.; Stangl, J.; Kovalenko, M. V.; Heiss, W. *Nat. Photonics* **2015**, *9*, 444–449.

(160) Sutherland, B. R.; Johnston, A. K.; Ip, A. H.; Xu, J.; Adinolfi, V.; Kanjanaboos, P.; Sargent, E. H. *ACS Photonics* **2015**, *2*, 1117–1123.

(161) Maculan, G.; Sheikh, A. D.; Abdelhady, A. L.; Saidaminov, M. I.; Haque, M. A.; Murali, B.; Alarousu, E.; Mohammed, O. F.; Wu, T.; Bakr, O. M. *J. Phys. Chem. Lett.* **2015**, *6*, 3781–3786.

(162) Wang, Y.; Li, X.; Song, J.; Xiao, L.; Zeng, H.; Sun, H. *Adv. Mater.* **2015**, *27*, 7101–7108.

(163) Sutherland, B.; Hoogland, S.; Adachi, M. *ACS Nano* **2014**, *8*, 10947–10952.

(164) Zhang, Q.; Ha, S. T.; Liu, X.; Sum, T. C.; Xiong, Q. *Nano Lett.* **2014**, *14*, 5995–6001.

(165) Deschler, F.; Price, M. *J. Phys. Chem. Lett.* **2014**, *5*, 1421–1426.

(166) Zhu, H.; Fu, Y.; Meng, F.; Wu, X.; Gong, Z.; Ding, Q.; Gustafsson, M. V; Trinh, M. T.; Jin, S.; Zhu, X.-Y. *Nat. Mater.* **2015**, *14*, 636–642.

(167) Shen, H.; Cao, W.; Shewmon, N. T.; Yang, C.; Li, L. S.; Xue, J. *Nano Lett.* **2015**, *15*, 1211–1216.

(168) Kim, Y.-H.; Cho, H.; Heo, J. H.; Kim, T.-S.; Myoung, N.; Lee, C.-L.; Im, S. H.; Lee, T.-W. *Adv. Mater.* **2015**, *27*, 1248–1254.

(169) Stranks, S. D.; Snaith, H. J. *Nat. Nanotechnol.* **2015**, *10*, 391–402.

(170) Kulbak, M.; Cahen, D.; Hodes, G. *J. Phys. Chem. Lett.* **2015**, *6*, 2452–2456.

(171) Stoumpos, C.; Malliakas, C. *Cryst. Growth Des.* **2013**, *15*, 2722–2727.

(172) Beal, R. E.; Slotcavage, D. J.; Leijtens, T.; Bowring, A. R.; Belisle, R. a; Nguyen, W. H.; Burkhard, G.; Hoke, E. T.; McGehee, M. D. *J. Phys. Chem. Lett.* **2016**, 2–7.

(173) Grätzel, M. *Nat. Mater.* **2014**, *13*, 838–842.

(174) Shi, D.; Adinolfi, V.; Comin, R.; Yuan, M.; Alarousu, E.; Buin, A.; Chen, Y.; Hoogland, S.; Rothenberger, A.; Katsiev, K.; Losovyj, Y.; Zhang, X.; Dowben, P. A.; Mohammed, O. F.; Sargent, E. H.; Bakr, O. M. *Science* **2015**, *347*, 519–522.

(175) Zhang, F.; Zhong, H.; Chen, C.; Wu, X.; Hu, X.; Huang, H. **2015**, *3*, 4533–4542.

(176) Protesescu, L.; Yakunin, S.; Bodnarchuk, M. I.; Krieg, F.; Caputo, R.; Hendon, C. H.; Yang, R. X.; Walsh, A.; Kovalenko, M. V. *Nano Lett.* **2015**, 1–5.

(177) Zhang, D.; Eaton, S. W.; Yu, Y.; Dou, L.; Yang, P. *J. Am. Chem. Soc.* **2015**, *137*, 9230–9233.

(178) Jellicoe, T. C.; Richter, J. M.; Glass, H. F. J.; Tabachnyk, M.; Brady, R.; Dutton, S. E.; Rao, A.; Friend, R. H.; Credgington, D.; Greenham, N. C.; Böhm, M. L. *J. Am. Chem. Soc.* **2016**, *138*, 2941–2944.

(179) Protesescu, L.; Yakunin, S.; Bodnarchuk, M. I.; Krieg, F.; Caputo, R.; Hendon, C. H.; Yang, R. X.; Walsh, A.; Kovalenko, M. V. *Nano Lett.* **2015**, *15*, 3692–3696.

(180) Chen, X.; Peng, L.; Huang, K.; Shi, Z.; Xie, R.; Yang, W. *Nano Res.* **2016**, *9*, 1–13.

(181) Sun, S.; Yuan, D.; Xu, Y.; Wang, A.; Deng, Z. *ACS Nano* **2016**, *10*, 3648–3657.

3 MULTIPLE EXCITON GENERATION IN PHOTOVOLTAIC DEVICES

3.1 Abstract

Multiple exciton generation – a process in which multiple charge-carrier pairs are generated from a single optical excitation - is a promising way to improve the photocurrent in photovoltaic devices and offers the potential to break the Shockley-Queisser limit. One-dimensional nanostructures, e.g. nanorods have been shown spectroscopically to display increased MEG efficiencies compared to their zero-dimensional analogues. Here we present solar cells fabricated from PbSe nanorods of three different bandgaps. All three devices showed external quantum efficiencies (EQEs) exceeding 100 % and we report a maximum EQE of 122% for cells consisting of the smallest bandgap NRs. We estimate internal quantum efficiencies to exceed 150% at relatively low energies compared with other MEG systems, and this demonstrates the potential for substantial improvements in device performance due to MEG.

This work was published as Multiple Exciton Generation in Lead Selenide Nanorod Solar Cells with External Quantum Efficiencies Exceeding 120% - Davis, N. J. L. K.; Böhm, M. L.; Tabachnyk, M.; Wisnivesky-Rocca-Rivarola, F.; Jellicoe, T. C.; Ducati, C.; Ehrler, B.; Greenham, N. C. Nat. Commun. 2015, 6, 8259.

All the below work was carried out by myself except where stated. Dr. Marcus L. Böhm performed the UPS and XPS measurements. Mrs. Florencia Wisnivsky-Rocca-

Rivarola performed the TEM measurements. Dr. Bruno Ehrler performed the ellipsometry measurements.

3.2 Introduction

Solar cells fabricated from conventional bulk semiconductors such as silicon or gallium arsenide are approaching the physical limit of solar power conversion efficiency (PCE)[1,2]. Thermalization of hot carriers is the predominant cause of this limitation[2]. A promising strategy to overcome such phonon-related loss processes is to harvest multiple charge carrier pairs generated from a single excitation. Recently it has been demonstrated that these mechanisms are particularly efficient in colloidal quantum dots (QDs) where the process is termed multiple exciton generation (MEG)[3–5]. MEG is enhanced in systems where the limited spatial extent of the excited states (a) relaxes the requirements for conservation of crystal momentum that apply in typical bulk systems[6] and (b) increases the MEG yield[7]. In an ideal system, bi-exciton states will be formed efficiently once the excitation energy exceeds twice the bandgap.

The multiple-exciton state formed by MEG in PbSe QDs has been shown in spectroscopic experiments to relax on a timescale of 20-200 ps [3] to a single-exciton state, by an Auger-like process that is the reverse of the MEG process. In order to harvest charge carriers from multiple-exciton states it is necessary for charge separation to occur on much faster timescales than Auger decay, and this is not necessarily easy to achieve in a device structure. We note that it is important to achieve two rapid charge transfer events for each doubly-excited nanoparticle, since the trion state formed after the first charge transfer event is known to decay rapidly[8].

Recently it has been shown that the initial yield of multi-exciton states is enhanced in PbSe nanorod (NR) systems[9–11]. It has been proposed[9] that this may be due to enhanced MEG rates arising from larger coulombic electron-hole binding in NRs[12]. Furthermore, Auger relaxation is found to be slowed in these one-dimensional systems[9]. It has been argued that this is due to a slower bimolecular Auger-type recombination in elongated nanostructures compared to a faster, three-particle Auger-type process in zero-dimensional QDs[9,13]. NR films are therefore attractive for photovoltaics exploiting MEG, however fabrication of working devices from NRs has so far proved very challenging[14].

Here we present the synthesis and characterization of PbSe nanorods and their incorporation into working devices. We demonstrate that charges generated by MEG can be extracted from solar cells consisting purely of PbSe NRs with external quantum efficiencies exceeding 120%.

3.3 Methods

PbSe nanorod synthesis: The synthesis of PbSe nanorods was carried out following modified versions of previously reported methods[15].

Briefly, PbO (1.76 g, 7.8 mmol), oleic acid (OA; 6.2 ml, 19.7 mmol, 5.6 g) and octadecene (ODE; 41.8 ml, 127.6 mmols, 32.6 g) were combined in a three-neck flask and degassed at 110 ^{0}C under vacuum (10^{-2} mbar or better) for 2 h. Subsequently, the reaction flask was flushed with nitrogen and heated to 160 ^{o}C. In parallel $CdCl_2$ (0.16 g, 0.9 mmol), tetradecylphosphonic acid (TDPA; 33 mg, 0.12 mmol) and oleylamine (8.13 ml, 30.4 mmol, 8.1 g) were combined in a separate three-neck flask and degassed under vacuum (10^{-2} mbar or better) at 110 °C for 12 h. The solution was flushed with nitrogen and set to 100 °C. A solution of selenium (1.92 g, 23.8 mmol) in tris(diethylamino)phosphine (TDP; 24.0 ml, 87.6 mmol; 20.8 g) was rapidly injected into the lead precursor solution. The bandgap of the PbSe nanorods was tuned by adjusting the reaction temperature while the overall reaction time was kept constant at 2.5 min. For bandgaps of 1.05 eV, 0.95 eV and 0.80 eV reaction temperatures of 120 ^{o}C, 130 ^{o}C and 140 ^{o}C were chosen respectively. For the in-situ $CdCl_2$ treatment 2.7 ml of the $CdCl_2$/TDPA solution was injected into the reaction flask of the nanorods, 10s before the crystal growth was quenched. The reaction was quenched by adding 20 ml of ice-cold hexane and by placing the reaction flask in an ice-water bath. The nanorods were isolated from the reaction mixture by flocculating to turbidity using a 1-buthanol/ethanol/hexane solvent system. The purified QDs were then re-dispersed in octane at a concentration of ~ 100 mg/ml and stored under Argon.

Nanorod analysis: Absorption spectra in solutions were measured on nanorod samples dispersed in tetrachloroethylene (TCE) at a concentration of ca. 1 mg ml^{-1} using a PerkinElmer Lambda 9 UV-Vis-IR spectrometer. Film absorption spectra were taken from PbSe nanorods which were prepared on quartz glass using a modified version of a literature reported layer-by-layer deposition method[16]. Briefly, PbSe nanorods were spin-coated on the substrate at a concentration of 25 mg/ml in octane (1500 rpm for 15 sec) after a wait of 5 sec. Subsequently, the native OA ligand was exchanged with ethane dithiol (20 mmol in acetonitrile) in a second spin-coating step using the same spinning conditions. In order to remove residual ligand and un-exchanged nanorods consecutive spin-rinsing steps using pure acetonitrile and octane were performed. This cycle was repeated four times. For the final nanorod layer we used hydrazine (1M in acetonitrile) instead of EDT as the exchanging ligand. The nanorod films were encapsulated by affixing a glass coverslip on the nanorod layer using carbon tape as spacer unit and epoxy glue as sealant. Transmission electron microscopy samples were prepared as reported elsewhere by drop casting a ca. 1 mg ml^{-1} nanorod solution in octane on a TEM Grid (200 Mesh Cu, Agar Scientific) in a nitrogen-filled glove box.

Photovoltaic device fabrication: Solar cells were prepared on indium tin oxide (ITO)-patterned glass substrates cleaned in an ultrasonic bath with ethanol, acetone and isopropanol. A ca. 55 nm ZnO layer (Figure 3-11 (c)) was deposited using a sol-gel method suggested by Lloyd et al.[17] and modified by Beek et al. [18]. Briefly, 250 µL of diethylzinc in hexane (1M) was diluted in 750 µL anhydrous tetrahydrofuran in a nitrogen filled glove box. The solution is spun-cast in air at 4000 rpm for 30 seconds. As water is required to convert the diethylzinc into ZnO, the films were then allowed to rest at room temperature under ambient environment for 15 minutes and were then annealed at 130 ^{o}C for 5 minutes. PbSe nanorods were deposited following a sequential layer-by-layer spin-coating technique as described above. The samples were then transferred into a thermal evaporator and molybdenum oxide (MoOx) (7 nm) and gold (Au) (100 nm) were deposited through a shadow mask at 3×10^{-6} mbar or better. The solar cells were encapsulated by affixing a glass slide on top of the contacts using transparent epoxy glue.

Photovoltaic device characterization: For external quantum efficiency (EQE) measurements, we used a 100 W tungsten halogen lamp (500-1500 nm) and a 120 W Xenon lamp (350 – 500 nm) dispersed through a monochromator (Oriel Cornerstone 260). For wavelengths between 1500 nm and 800 nm we employed a set of InGaAs detectors, (ThorLabs SM1PD2A) and for wavelengths between 900 nm and 350 nm a set of silicon diodes (ThorLabs SM05PD1A) were used. A Keithley 2635 source measure unit (SMU) was used to measure the short-circuit current as a function of wavelength. The incident light was focused to a spot size of ca. 1 mm^2 using a set of lenses to illuminate the individual pixel of size 5.5 cm^2. Current-voltage characteristics were measured under AM 1.5G conditions using an Abet Sun 2000 solar simulator, at an intensity equivalent to 100 mW cm^{-2} after correcting for spectral mismatch. Both the dark and light current-voltage characteristics were measured using the Keithley 2635 SMU.

Internal quantum efficiency measurements: Internal quantum efficiency (IQE) is represented as EQE/absorbed light fraction[5]. The absorbed light fraction was found by measuring the reflectivity at ca. normal incidence of a device using a photodiode. We used a 100 W tungsten halogen lamp (500-1500nm) and a 120 W Xenon lamp (350 – 500 nm) dispersed through a monochromator (Oriel Cornerstone 260). For wavelengths between 1500 nm and 800 nm we employed a set of InGaAs detectors, (ThorLabs SM1PD2A) and for wavelengths between 900 nm and 350 nm a set of silicon diodes (ThorLabs SM05PD1A) were used. The absorbed light fraction is then determined by 1 - R where R is the reflectivity.

Photoelectron Spectroscopy: For photoelectron spectroscopy 3 nm chromium and 80 nm gold were thermally evaporated onto cleaned silicon substrates. The QDs were deposited in a layer-by-layer fashion as described above. The samples were then transferred into the vacuum chamber of a Thermo Scientific ESCALAB 250Xi X-ray Photoelectron Spectrometer (XPS) minimizing air exposure (about 10sec).

Ultraviolet photoelectron spectroscopy (UPS) measurements were performed using a double-differentially pumped He gas discharge lamp (He I radiation ($h\nu$=21.2 eV); pass energy 2 eV). In Figure 3-7 the spectra are presented as a function of binding energy with respect to vacuum level.

X-ray photoelectron spectroscopy (XPS) was performed using an XR6 monochromated Al Kα X-ray source with an energy $h\upsilon$ = 1486.6 eV and a spot size of 650 μm. To prevent the samples from surface charging an Argon-ion flood gun was used. For data analysis of both UPS- and XPS spectra we used the software package “Thermo Avantage” (Thermo Fisher Scientific Inc., Waltham, USA).

Transmission Electron Microscopy (TEM): Samples were prepared by affixing a TEM grid (200 Mesh Cu, Agar Scientific) onto a glass substrate. A single layer of PbSe QDs was deposited from an octane solution (ca. 5 mg/ml) and was ligand exchanged with the ligand mixture solution following methods described above. The prepared TEM grid was then removed from the glass substrate and imaged employing a FEI Tecnai F20 microscope operated at 200 kV. For high resolution TEM (HRTEM) the same microscope and conditions were used. TEM analysis of the crystal orientation and lattice spacing is shown in Figure 3-4.

The preparation of a cross-sectional lamellar specimen was carried out on a FEI Helios dual beam FEG SEM/FIB microscope, fitted with an Omniprobe micromanipulator for in-situ lift-out. The sample preparation was performed following a standard FIB in-situ lift-out technique,[19] and the thinning step of the lamellar specimen was performed with decreasing beam current to reduce sample damage and improve sputtering of the material. The cross-sectional specimen was analyzed through high angle annular dark field STEM (HAADF-STEM), using a Fischione detector on a FEI Tecnai F20 microscope, operated at 200 kV.

Energy dispersive x-ray spectroscopy (EDX) mapping of the cross sectional specimen was performed using a FEI Tecnai Orisis TEM/STEM equipped with a field-assisted thermionic emitter gun, operating at 200 kV. The microscope is also equipped with four Bruker silicon drift detectors (SDD) for high collection efficiency and high count rates.

The device structure was analyzed using EDX compositional mapping and de-noised using principle component analysis (PCA) (Figure 3-6). PCA is a multivariate statistical method that sorts the components in the data in order of decreasing variance. In this case it was used to estimate the dimensionality of the data by plotting the explained variance against the component index in a logarithmic y-scale. This plot shows a quick drop, eventually becoming a slowly descending line. The point at which it becomes linear is considered to give an estimate of the number of components within the dataset. For this case, nine components were identified. The de-noising property of PCA is achieved by using a reduced set of components to make a model of the original signal, reducing the dimensionality of the data, and consequently the noise.

Transmission Electron Microscopy image analysis: Nanocrystal size distributions were measured using the software package ImageJ (https://imagej.nih.gov/ij/). Briefly a contrast threshold was chosen which solely included the nanocrystal particles and not the image background. Using the analyze particle function, which counts areas of contrast above the threshold, particle size was limited to a designated maximum which excluded overlaid nanocrystals and the total nanocrystals and their size were measured. This was done for a number of different TEM images. To determine the proportion of rods, hook and dot shaped nanoparticles the circularity parameter was used in the analyze particles function.

Ellipsometry: For ellipsometry, all samples were prepared as described above but on silicon substrates. The only exception is ITO, which was measured on glass as received from Psiotec. The samples were measured on a Woollam Vase VB-400 ellipsometry in reflection mode (ITO in transmission mode) using monochromatic light from a xenon lamp guided through a monochromator. The data for the quantum dot samples was fitted using a combination of a Cauchy and a Gaussian model. The ITO data was fitted with a combination of a Drude and a Lorentz oscillator and the MoOx was fitted with a Lorentz oscillator.

Transfer matrix modelling of IQE: Reflectance was modelled as per literature sources[20,21]. *n* and *k* values were measured in-house as described above and are presented in Figure 3-12. This program calculates the field profile, exciton generation profile and generated current from the wavelength dependent complex indices of refraction in devices using a transfer matrix method described in detail in ref [22,23]. It assumes the light source located in an n = 1 environment (air) and that the first layer is a thick substrate, so that incoherent reflection at the air/1st layer interface is taken into account before the coherent interference is calculated in the remaining layers. Film thicknesses were measured using a DEKTAK profilometer. Error in the model is given as ± 10 nm of the active layer.

3.4 Results

3.4.1 Nanorod synthesis

PbSe nanorods (NRs) of three different s (1.05 eV, 0.95 eV and 0.80 eV) were synthesized following a method modified from that reported by Koh et al.[15] (see Figure 3-1 (a)). Further XPS and TEM analysis are provided in Figure 3-3 and Figure 3-4 respectively. We employed an additional in-situ CdCl2 treatment at the end of the NR synthesis to provide additional surface passivation. It has been shown that this approach minimizes the occurrence of sub-bandgap tail states which improves solar cell performance significantly[24,25].

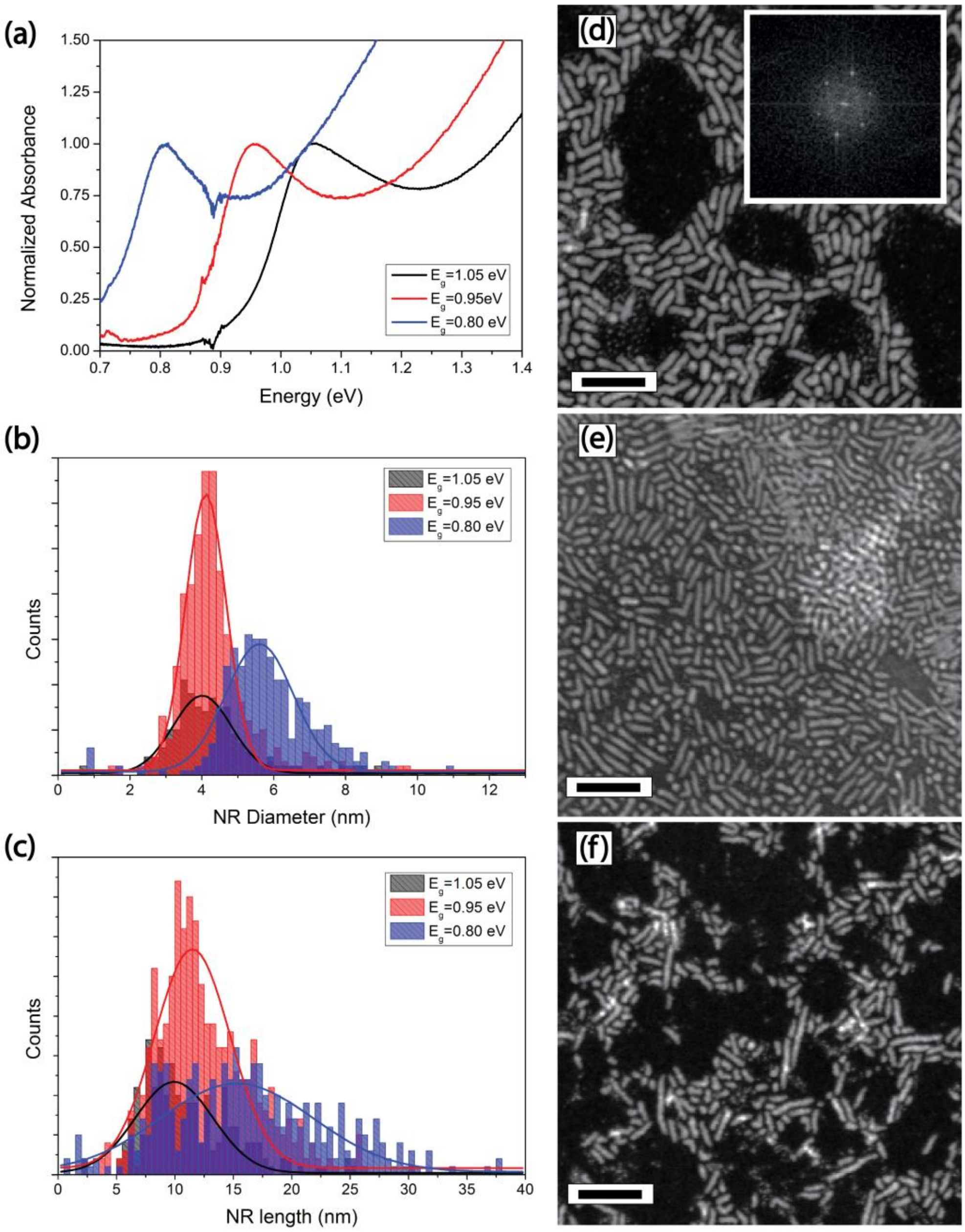

Figure 3-1: Analysis of synthesized NRs. (a) Normalized absorbance spectra of three different $CdCl_2$-treated PbSe NR samples in solution. The feature at 0.88 eV is an artefact due to the detector change during the absorbance measurement. (b) Short- and (c) long-axis distribution of the same bandgap PbSe NRs as determined by analysis of the scanning transmission electron microscopy (TEM) images (details in the methods). High angle annular dark field (HAADF) TEM images for 0.80 eV, 0.95 eV and 1.05 eV bandgap samples are shown in (d-f). To confirm the lattice parameters of PbSe in the synthesized NRs we extract an FFT image from a high resolution TEM for the 0.8eV bandgap sample (see inset (d)). The scale bars in (d-f) correspond to 25 nm.

The NR synthesis was optimized to minimize the diameter and length distributions and to reduce the formation of dots and hooks, in order to improve charge transport[26–28]. We optimized existing PbSe NR synthesis methods such that the NR aspect ratio was ca. 7 and the quantity of residual spherical quantum dots and hook-like structures is minimized. Recently, it has been demonstrated by Boercker et al. that both water and oleic acid (OA) influence the nanorod shape greatly[28]. For instance, while increased water content reduces the aspect ratio of the final NRs, it was shown that excess quantities of uncoordinated OA in the Pb-oleate precursor solution promotes the formation of branched nanostructures. It has been discussed that a resulting increased reactivity of potential side reactions such as the reaction of tris(dimethylamino)phosphine (TDP) to bis(diethylamido)phosphorous acid (BDPA) are likely to drive these structural dependences on the content of free OA and water.

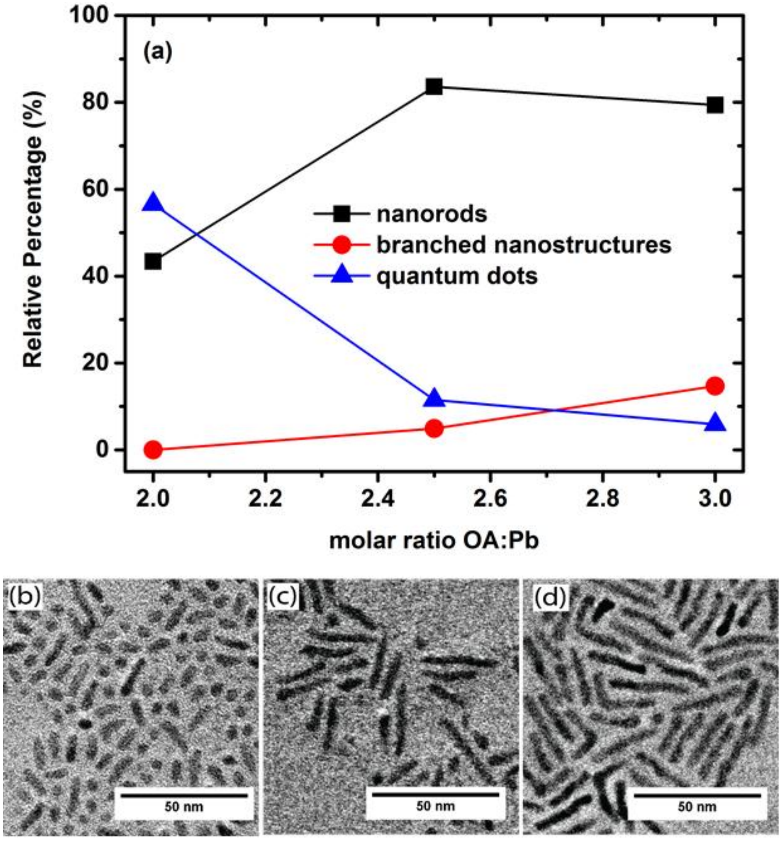

Figure 3-2: Optimization of NR synthesis. (a) Relative percentage of nanostructure species formed as a function of OA:Pb stoichiometric ratio from TEM image analysis (details in the method). Transmission electron microscopy (TEM) images of nanostructures formed in a reaction employing a 2.0 (b), 2.5 (c) and 3.0 (d) molar ratio of OA and Pb in the Pb-precursor solution. All TEMs shown are before size selective precipitation to remove residual quantum dots.

In order to reduce the branching ratio of the nanocrystals we explore the influence of different Pb to OA ratios (see Figure 3-2 (a)) while keeping the water content at a minimum (fully degassed reactants). We find that at a stoichiometric ratio of 2.5 (OA:Pb) in the Pb-precursor solution produces the highest relative quantity of rod structures and keeps the unwanted population of branched nanostructures to a minimum. We note that with higher OA:Pb ratios the relative quantity of 0-dimensional quantum dots decreases further. As these crystals can be separated from the NRs via size-selective precipitation we evaluate an OA:Pb ratio of 2.5 as optimized stoichiometry for our Pb-precursor.

In Figure 3-2 (b-d) we show additional transmission electron microscopy (TEM) images for the different OA:Pb ratios. TEM confirmed only negligible quantities (< 5 % by particle number) of non-NR structures, and diameter and length standard deviations of ca. 8 % and 13 % respectively (see Figure 3-1 (b-f)).

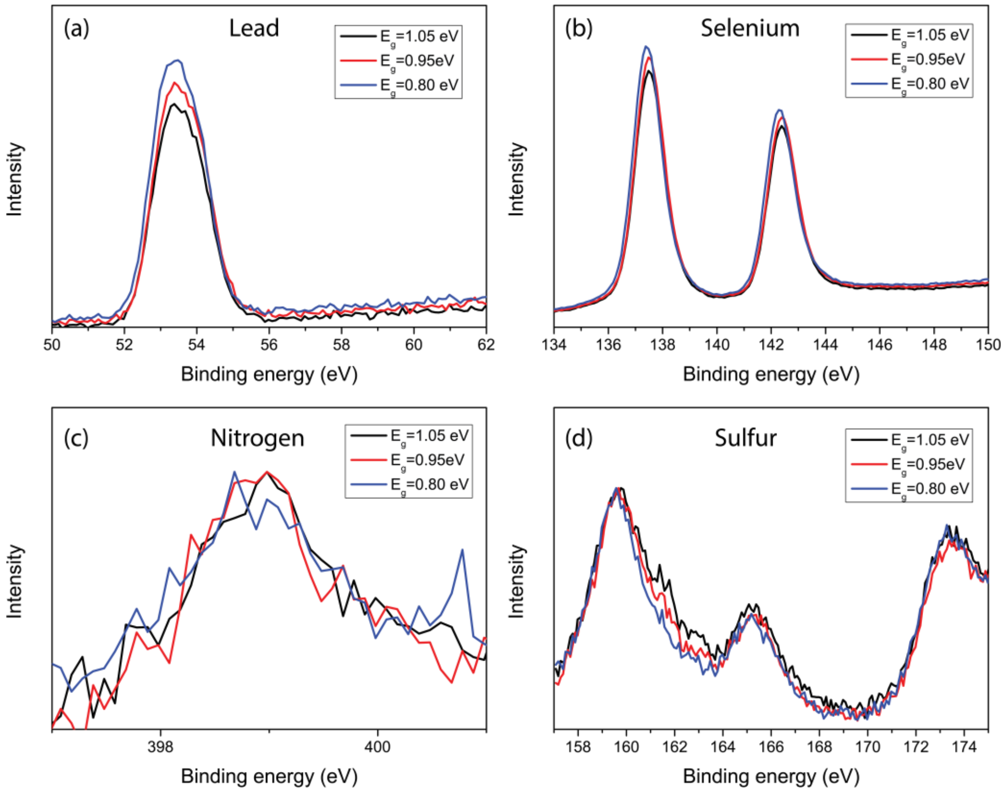

Figure 3-3: X-ray photoelectron spectroscopy conducted on $CdCl_2$-treated PbSe nanorod films. These were prepared using EDT and hydrazine as the final ligand species. Three different bandgap PbSe nanorods were measured: 0.80eV (color), 0.95eV (black) and 1.05eV (gray)

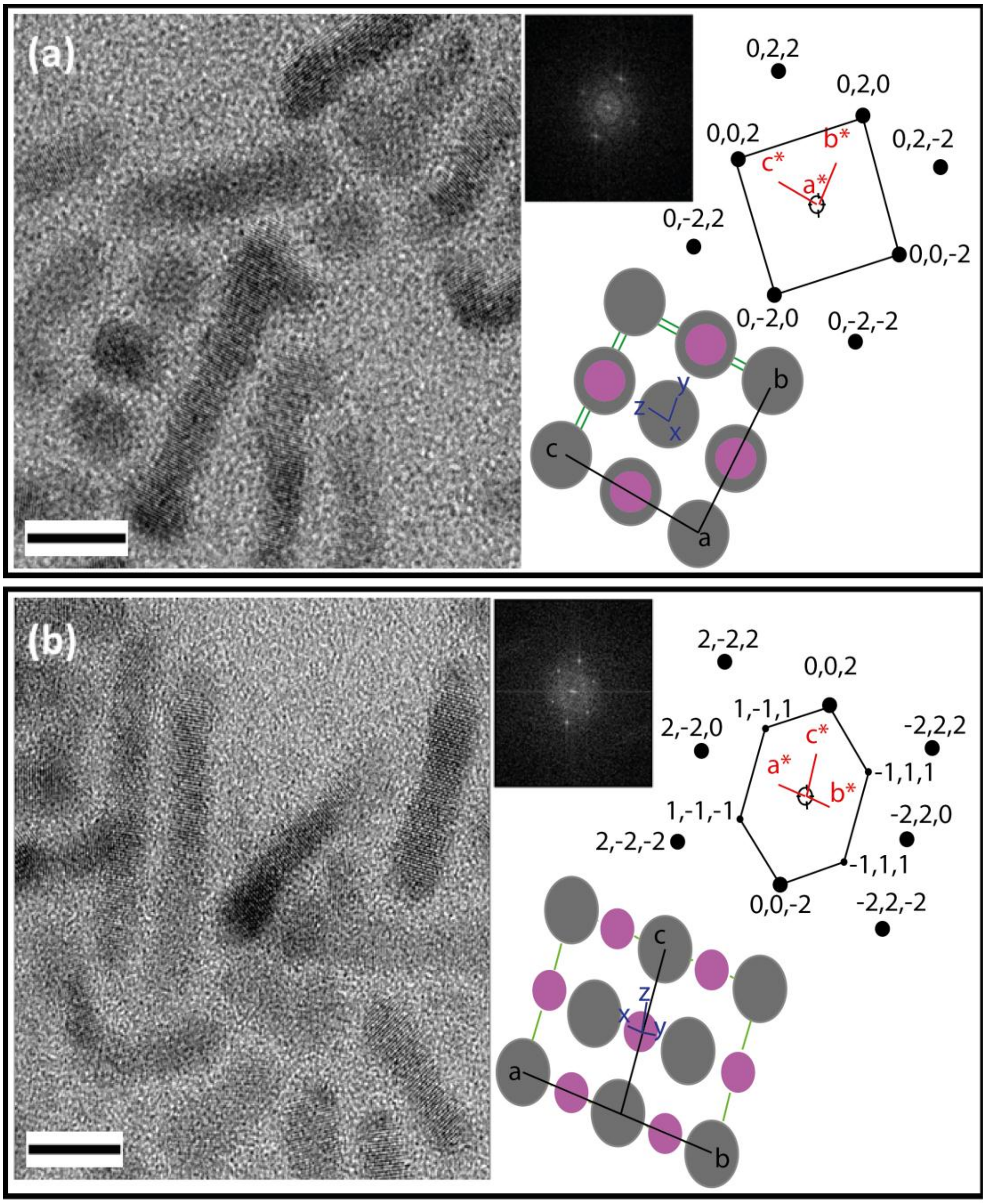

Figure 3-4: Lattice spacing and crystal orientation of PbSe nanorods; (a) Imaged from the PbSe zone Axis [1 0 0] (d1 = 3.06 Å, d2 = 3.06 Å, Angle = 90°). (b) Imaged from the PbSe zone Axis [1 1 0] (d1 = 3.53 Å, d2 = 3.53 Å, Angle = 90°). Scale bars correspond to 10 nm.

3.4.2 Photovoltaic device fabrication

We fabricated solar cells by depositing a dense array of PbSe NRs on a ZnO film which was produced using a sol-gel method[5,18] (see Figure 3-5(a) for the device architecture).

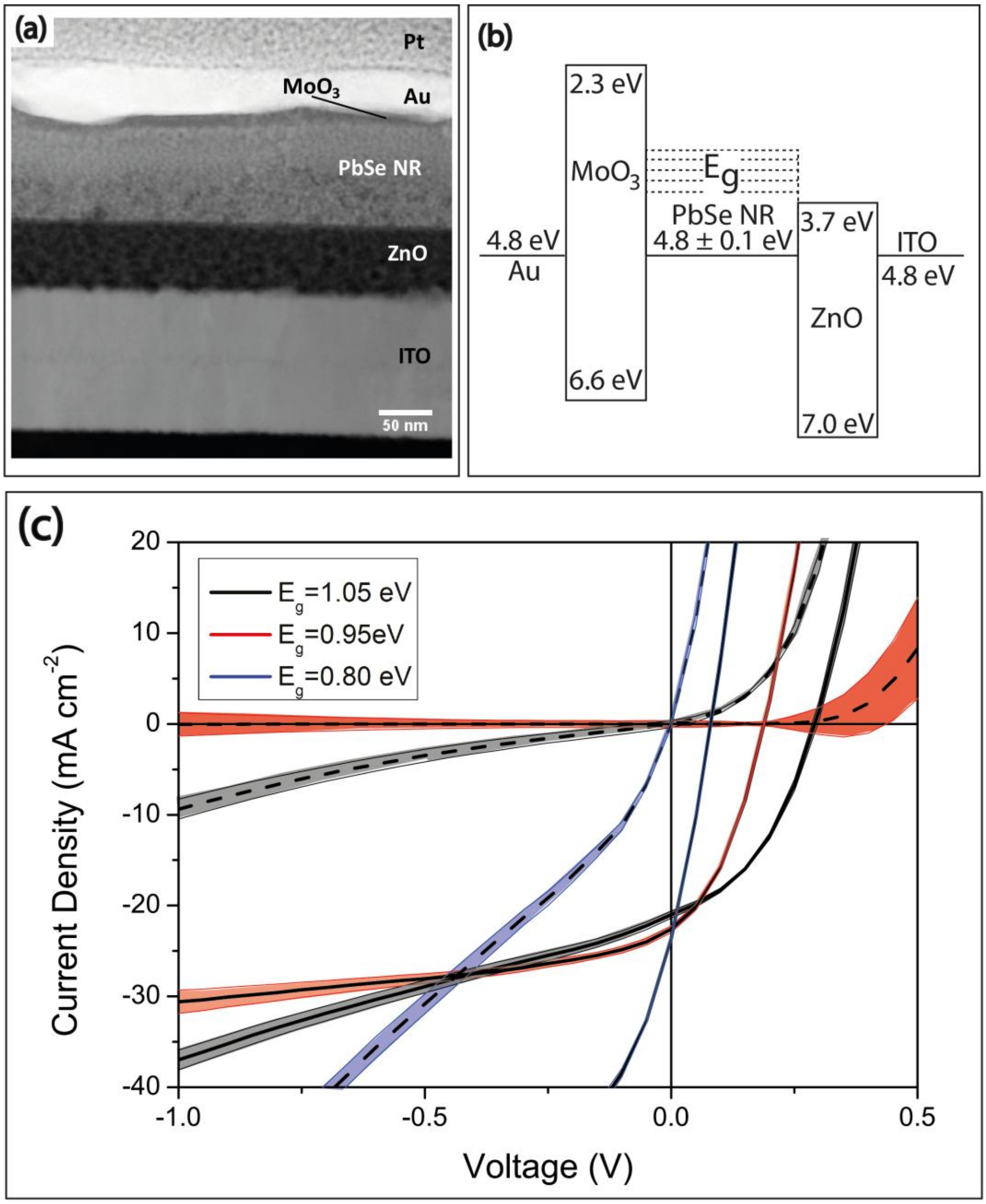

Figure 3-5: PbSe NR photovoltaic devices. (a) Cross-sectional TEM outlining the device architecture (see Figure 3-6) for details on compositional analysis) and (b) energy alignment as determined by a combination of ultraviolet photoelectron spectroscopy (UPS) and absorbance spectroscopy. (c) JV characteristics of depleted heterojunction solar cells consisting of PbSe NRs with bandgaps 0.80 eV (blue), 0.95 eV (red) and 1.05 eV (black). The dark currents are shown as dashed lines and the JV curves under AM1.5G illumination are shown as solid lines. We show the averaged performance of multiple independent solar cells (6 cells for 1.05 eV, 5 cells for 0.95 eV and 5 cells for 0.80 eV) in dark lines and the spread as a shaded area around the mean.

The NRs were deposited in a layer-by-layer approach using the ligand 1,2-ethanedithiol (EDT) for the first layers and hydrazine as the exchanging ligand for the final NR layer. The device structure was analyzed using EDX compositional mapping and de-noised using principle component analysis (PCA) (Figure 3-6). X-ray line intensities were then extracted from the EDX spectrum from each component, generating the individual intensity maps for the elements of interest. In order to facilitate the interactive data analysis of these complex datasets, HyperSpy an open-source, free software package, has been used to analyze the EDX data from HAADF-STEM spectrum images.

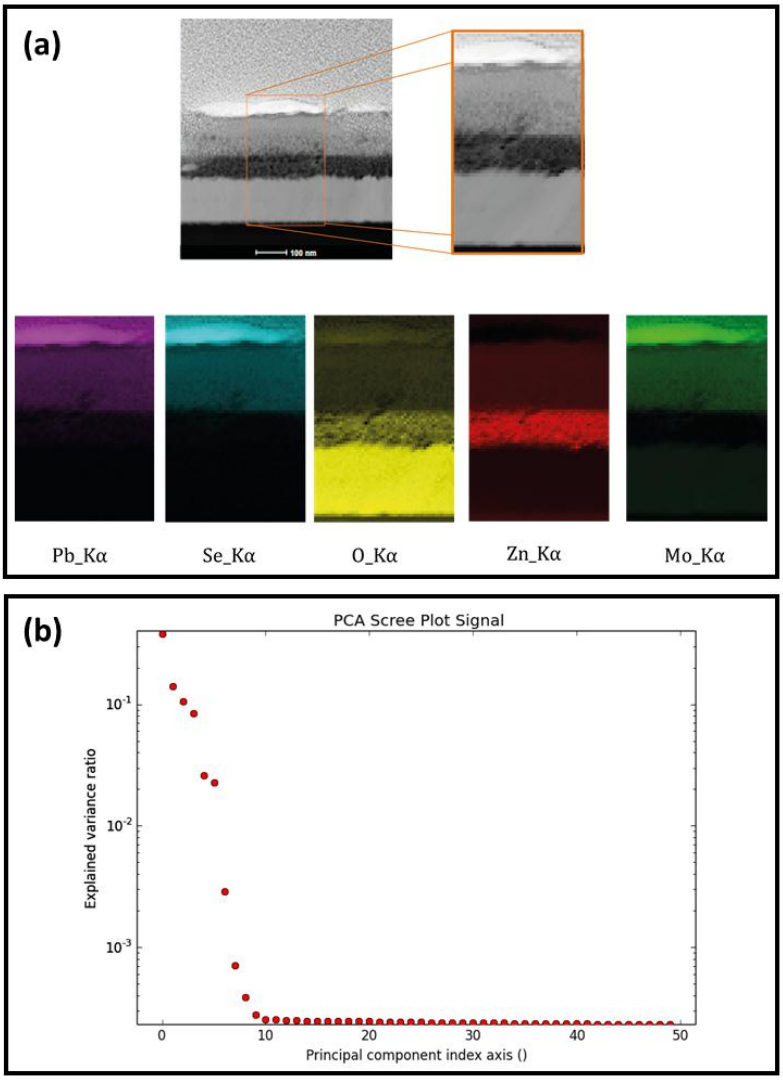

Figure 3-6: Analysis of EDX compositional maps (a) EDX Compositional maps. The images were de-noised using principal component analysis (PCA) and the maps were plotted from the resulting intensity profile for each element. (b) Principal component analysis (PCA) has been used to reduce the noise from the acquired EDX spectra

Due to the effect of ligand-induced surface dipoles, it has been shown recently that QDs treated with amine-functionalized ligands exhibit shifted operational HOMO and LUMO levels which are closer to the vacuum level compared to analogous QD films employing thiol-functionalized ligands[29]. A multi-layer QD film where the bottom layers are treated with EDT and the top layer with hydrazine is therefore likely to show an energy cascading structure which promotes charge extraction[30]. The relevant energy levels were determined using a combination of ultraviolet photoelectron spectroscopy (UPS) and absorbance spectroscopy as described in previous work[31] (see Figure 3-7) and are presented in Figure 3-5 (b).

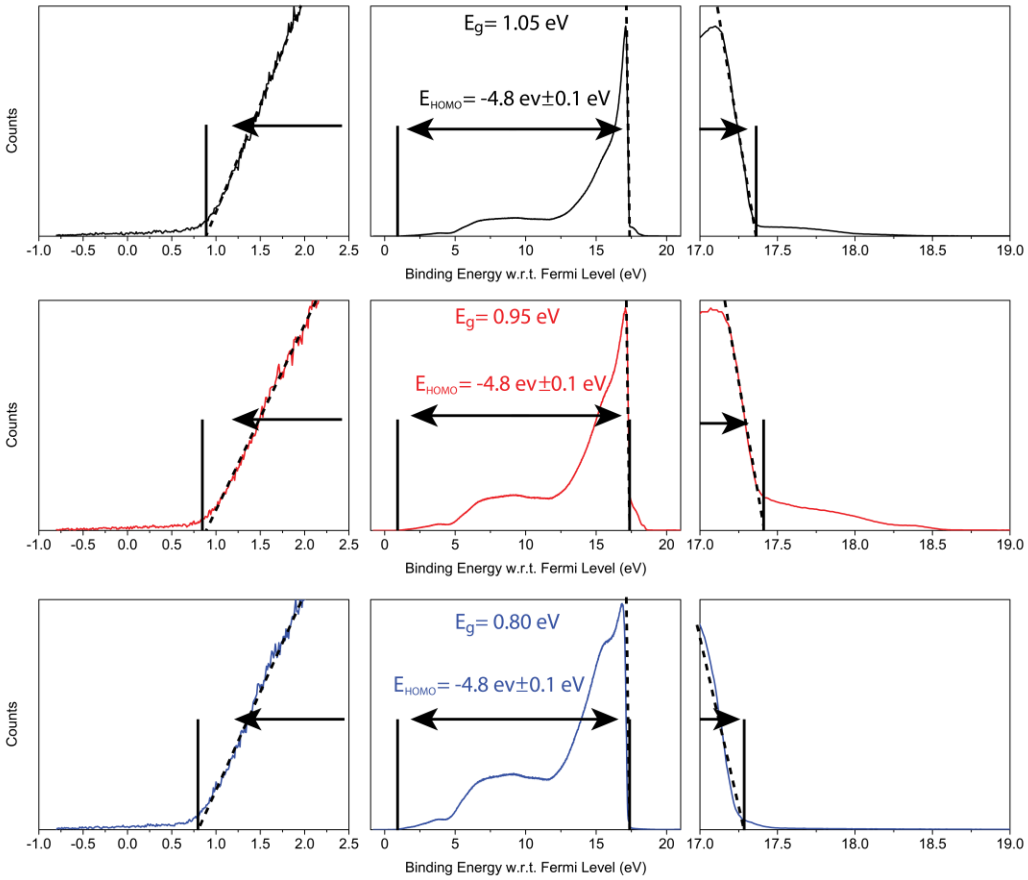

Figure 3-7: Ultraviolet photoelectron spectroscopy of films consisting of $CdCl_2$-treated PbSe nanorods. These were deposited in a layer-by-layer approach using EDT and hydrazine as the final ligand species. We identify the LUMO level of the nanorods as demonstrated previously.[21] Briefly, we determine the bandgap of the nanorods from the energy of the first excitonic peak in the solution absorption spectrum (Figure 3-1) and subtract this value from the HOMO level measured by UPS to identify the LUMO level of the nanorods.

Current-voltage characteristics of the optimized solar cells made from three different bandgap NRs are shown in Figure 3-5(c) and the standard photovoltaic device parameters are listed in Table 3-1. It's worth noting that these devices showed large leakage current without illumination. Upon illumination these devices seem to produce more current at greater reverse biases, but this is due to their imperfect diode operation as seen in the dark current. When the current was measured at different reverse biases (up to 10 V) no additional current was produced.

Table 3-1: Photovoltaic parameters of PbSe NR champion devices with three different bandgaps.

E_g (eV)	J_{sc} (mA/cm^2)	V_{oc} (V)	FF (%)	η (%)
1.05	21.0	0.29	41	2.52
0.95	22.6	0.19	37	1.61
0.80	23.5	0.08	28	0.54

We compare the performance of NR devices, which were ligated with either 1,3 benzene dithiol (BDT) or the combination of 1,2-ethane dithiol (EDT) and hydrazine. We found that the dual ligand approach with EDT and hydrazine produces higher short circuit currents and fill factors and reduces the open circuit voltage marginally (see Figure 3-8 (a)). This effect has been explained in literature with an enhanced charge carrier mobility in NC films treated with amine ligands[3,4]. Furthermore, replacing TiO_2 as electron-collecting layer with ZnO showed similar improvements to the photovoltaic parameters (see Figure 3-8 (b)). We tentatively assign the increased short-circuit current to higher charge mobilities in ZnO compared to TiO_2[34,35] and the mildly reduced open circuit voltage to a greater abundance of sub-bandgap tail states in ZnO[36]. We next study the effect of the improved nanorod synthesis (i.e. suppression of residual 0-diminsional quantum dots and remaining "hook/cross"-nanostructures in the nanorod sample) as well as the applied CdCl2-treatment on the device performance. While the "cleaner" nanorod sample shows mainly an increase in short-circuit current, it is the additional $CdCl_2$-treatment which improves all relevant photovoltaic parameters (i.e. V_{oc}, fill factor as well as the J_{sc}, see Figure 3-8 (c)).

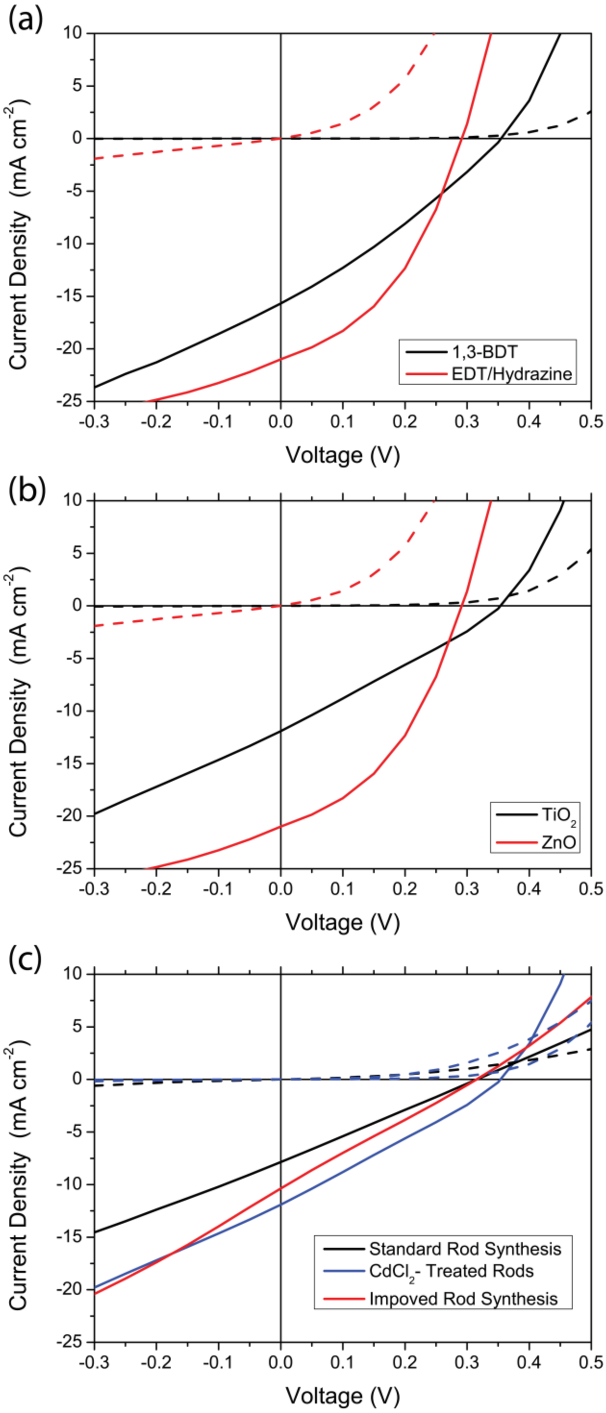

Figure 3-8: Optimization of device parameters. The dark currents are shown as dashed lines and the JV curves under AM1.5G illumination are shown as solid lines. The final surface ligands (a), the metal oxide (b) and the synthesis conditions as outlined in the methods (c) were optimized. In (a) the $CdCl_2$-treated PbSe NRs (E_g = 1.05 eV) where deposited on ZnO. In (b) we compared the same NRs passivated with EDT and hydrazine on TiO_2 and ZnO. In (c) we correlated the PV performance of differently synthesized NRs (E_g = 0.91 eV) deposited on ZnO.

We speculate that the first effect may be associated with an improved NR bulk morphology[27,37] and assign a refined surface passivation to be responsible for the latter improvement[24].The influence on device performance of choice of ligands, metal oxides and nanorod synthesis is presented in Figure 3-8, while the optimized device architecture is shown in Figure 3-5 (a). We attribute the non-ideal diode behavior seen particularly for the 0.8 eV NR device to tail states in the sol-gel processed ZnO[20] and remaining trap states in the PbSe NR film[31]. These tail states allow trap-induced leakage current especially in devices fabricated from small-bandgap NRs under reverse bias, thereby reducing the quality of the diode in the dark. Under illumination we expect these tail states to promote trap-assisted recombination, thereby reducing the open-circuit voltage[31,38].

3.4.3 Device quantum efficiencies

Figure 3-9 displays the short-circuit external quantum efficiency (EQE) spectrum for NR devices. Interestingly, we observe maximum EQEs of 109 ± 3 %, 113 ± 4 % and 122 ± 3 % for devices with NR bandgaps of 1.05 eV, 0.95 eV and 0.80 eV respectively at high photon energies (ca. 3.3 eV). We note that no antireflective coating was employed to reduce reflectance losses at the glass/air interface.

Reassuringly, we can reconstruct the measured short circuit current within ca. 1 % measurement error by integrating the EQE over the AM1.5G solar spectrum (see Table 3-2). Furthermore, measuring the EQE under different white light biases produced identical spectra, suggesting a current collection which is independent of the charge carrier density (see Figure 3-10 (a)). For the lowest photon energies we recognize a clearly visible first excitonic peak in all three test devices and explain the steep drop in quantum efficiency for photon energies exceeding 3.5 eV by the onset of absorption of the ZnO layer (see Figure 3-11 (a)).

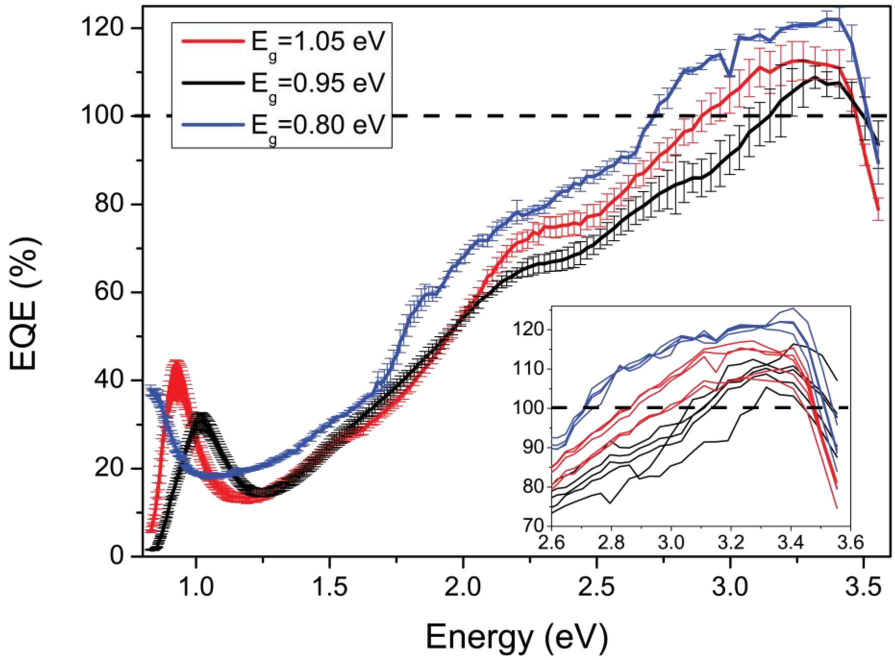

Figure 3-9: External quantum efficiencies of PbSe NR photovoltaic devices. The bandgaps of the NRs used are 0.80 eV (blue), 0.95 eV (red) and 1.05 eV (black). The inset shows the high-energy region of the individual EQE spectra of the solar cells displaying quantum efficiencies greater than 100 %. Error bars show the mean standard error of multiple independent solar cells (6 cells for 1.05 eV, 5 cells for 0.95 eV and 5 cells for 0.80 eV).

Table 3-2: Error between calculated and measured short circuit current. In order to reconstruct the short-circuit current from the individual EQEs we multiply the spectrally resolved photocurrent at each wavelength with the corresponding AM1.5G value and integrate over the entire spectrum. The respective error in % was taken from the error of each individual comparison between measured and calculated J_{SC}. We compared in total 4, 6 and 6 independent solar cells for NR devices of the bandgap 0.80 eV, 0.95 eV and 1.05 eV respectively.

Eg	Measured JSC (mA/cm^2)	Calculated JSC (mA/cm^2)	Error (%)
1.05	20.3 ± 1.1	20.2 ± 1.0	0.4
0.95	21.2 ± 1.1	21.2 ± 1.0	1.1
0.80	23.2 ± 0.6	22.6 ± 0.4	0.9

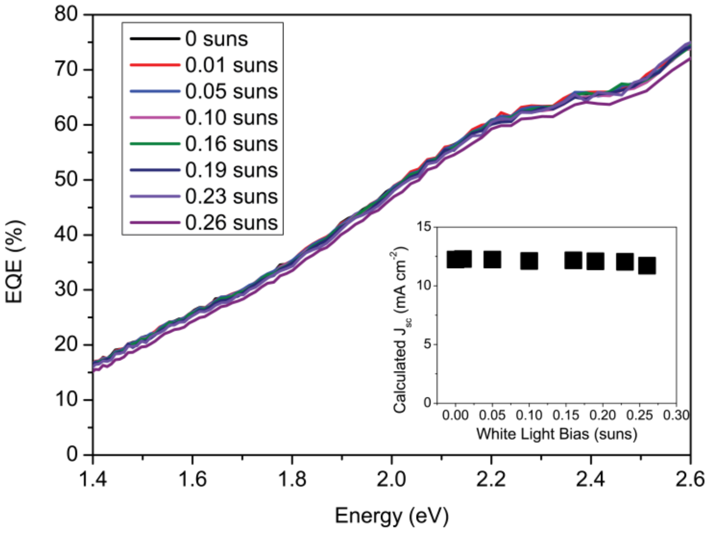

Figure 3-10: White light bias dependent EQE spectra of devices consisting of NRs of the bandgap 1.05 eV. The short-circuit current shown in the inset was calculated by integrating the EQE against the AM1.5G solar spectrum. Due to the lack of photocurrent for excitations of 2.7 eV and higher energies as well as the lack of the photocurrent in the infra-red the calculated values are smaller than the ones listed in Table 3-2. The white light bias was calibrated against the photon flux of an AM1.5G solar simulator using a reference silicon solar cell (Czibula & Grundmann 015-2008).

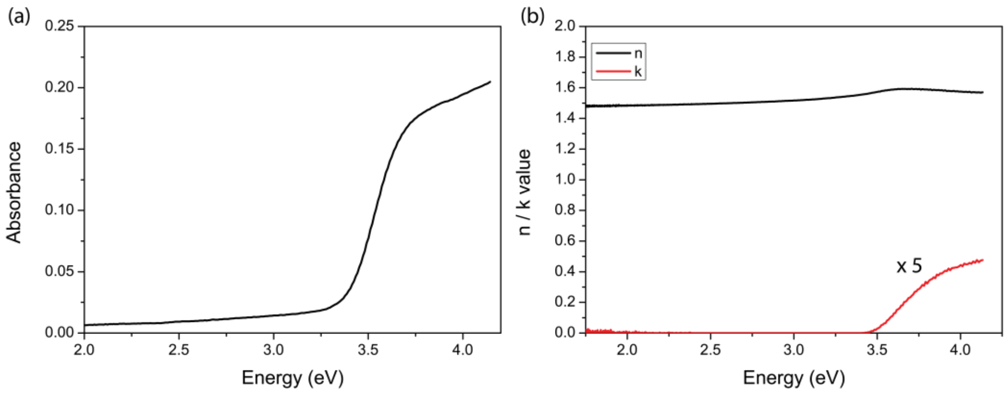

Figure 3-11: Absorption and ellipsometry of Sol-Gel ZnO film. (a) Film absorbance of sol-gel processed ZnO. (b) Film thickness determination using the refractive index n and extinction coefficient k determined using ellipsometry. We determine the film thickness of ZnO by ellipsometry. Using the phase delay caused by the interference between the light reflected from the surface and the light which travelled through the film we relate the physical film thickness with the index of refraction n. We identify a film thickness of ca. 55nm.

To allow for incomplete absorption of incident photons, we next determined the internal quantum efficiency (IQE) via two independent approaches: First, we measure the fraction of light reflected from the device at each photon energy, $R_{(hv)}$, using a calibrated silicon or germanium photodiode. The IQE was then calculated as $IQE^{Exp}(hv) = EQE_{(hv)}/(1 - R_{(hv)})$. We note that $IQE^{Exp}(hv)$ presents the lower bound for the IQE, as parasitic absorbance by other layers and diffuse scattering are negelected[5]. In our second approach, we derive $IQE^{Model}(hv)$ by applying an optical transfer matrix model[22,23] using the refractive indices n and the extinction coefficients k of each device layer measured by ellipsometry (see Figure 3-12).

In this case $IQE^{Model}(hv) = EQE/A$, where A is the calculated fraction of light absorbed. Reassuringly, we identify similar values for $IQE^{Exp}(hv)$ and $IQE^{Model}(hv)$ (see Figure 3-13). These values at their highest are above 170 % which is comparable to devices incorporating singlet fission materials to generate multiple excitons[22,39,40].

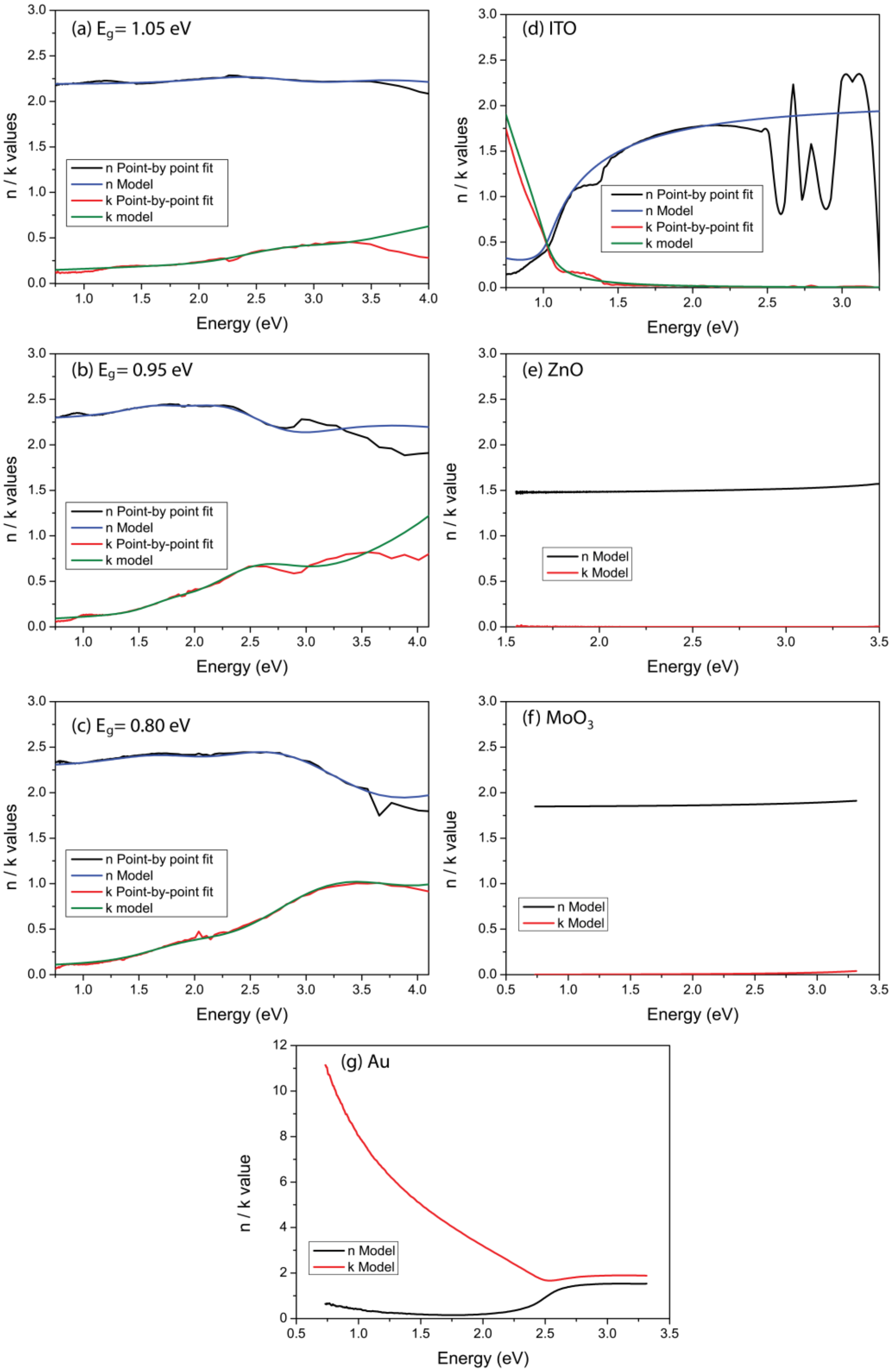

Figure 3-12: Determination of the refractive index n and the extinction coefficient k of PbSe NRs of (a) 1.05eV E$_g$, (b) 0.95eV E$_g$ (c) 0.8eV E$_g$, (d) ITO, (e) ZnO, (f) MoO3 and (g) Au layers using ellipsometry. Layer thickness are as follows: 1.05 eV PbSe rods 115 ± 10 nm, 0.95 eV PbSe rods 124 ± 10 nm. 0.80 eV PbSe rods 122 ± 10 nm, ITO 150 nm, ZnO 55 ± 5 nm, MoO$_3$ 8.0 nm ± 0.1 nm, Au 100 nm ± 1 nm.

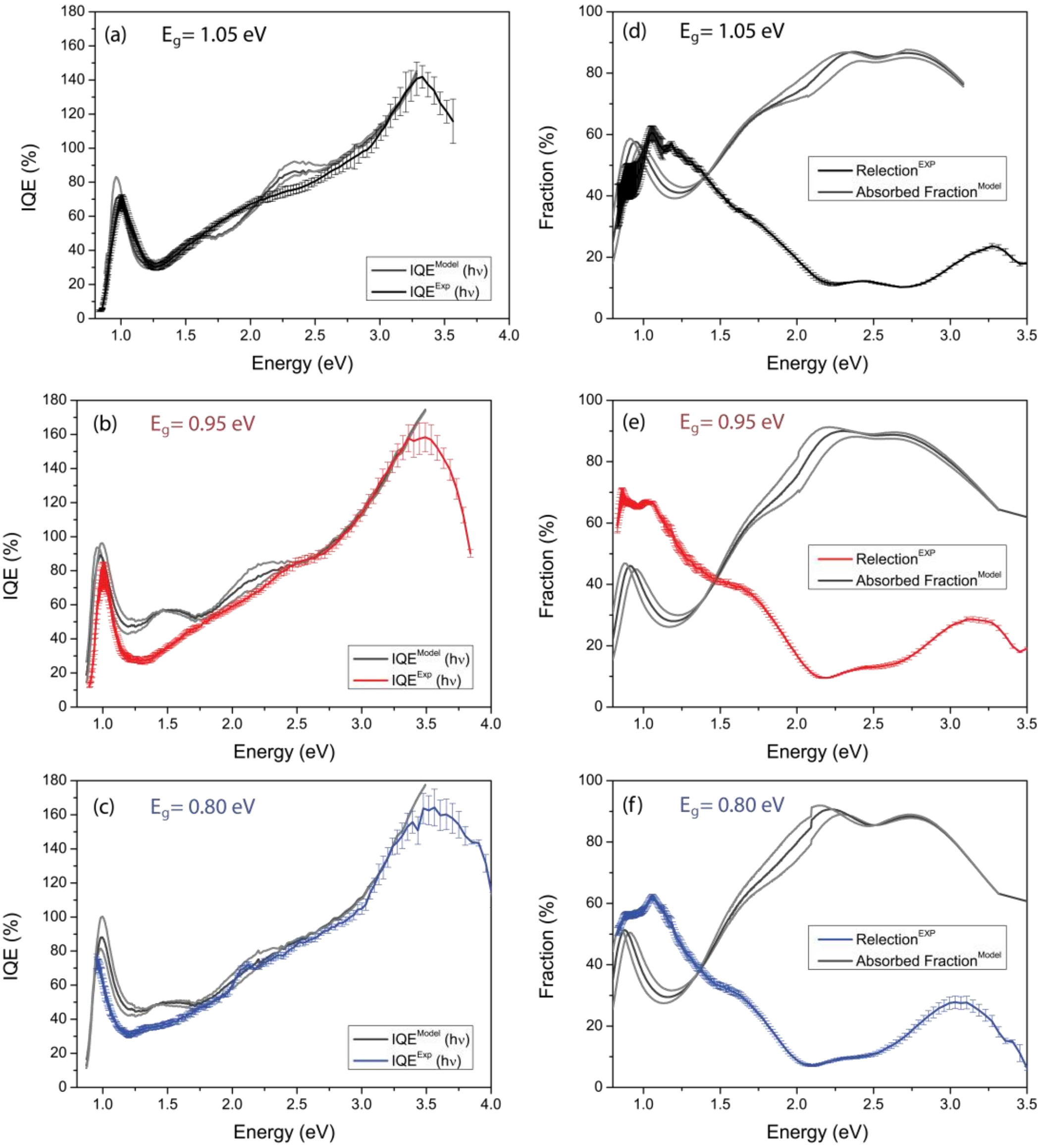

Figure 3-13: Internal quantum efficiency (IQE) of photovoltaic devices. NRs with bandgaps of 1.05 eV (a), 0.95 eV (b) and 0.80 eV (c). $IQE^{EXP}(h\nu)$ and $IQE^{Model}(h\nu)$ were determined respectively using reflectance measurements and optical modeling as described in the text. (d)-(f) show the measured reflection (colored curve) and modelled absorbed fraction (grey curve) for bandgaps of 1.05 eV, 0.95 eV and 0.80 eV respectively. Error bars show the mean standard error of multiple independent solar cells (6 cells for 1.05 eV, 5 cells for 0.95 eV and 5 cells for 0.80 eV). The range of grey curves shown for the modeled results illustrate the effect of changing the active layer thickness in the model by the experimental error of ±10 nm.

We note that the dip in EQE after the first excitonic absorption peak is deeper than would be expected based on the absorption spectrum (see Figure 3-14 (a)), leading to a significant dip in the calculated IQE spectrum in the same spectral region. This phenomenon is difficult to explain, but is seen in many nanocrystal devices[5,41–43]. It is unlikely to result from charge generation taking place deeper in the device when the absorption coefficient is lower, as these effects should recover in full when the absorption coefficient regains its initial peak value at around 1.4 Eg (see Figure 3-14 (b) for film absorption).

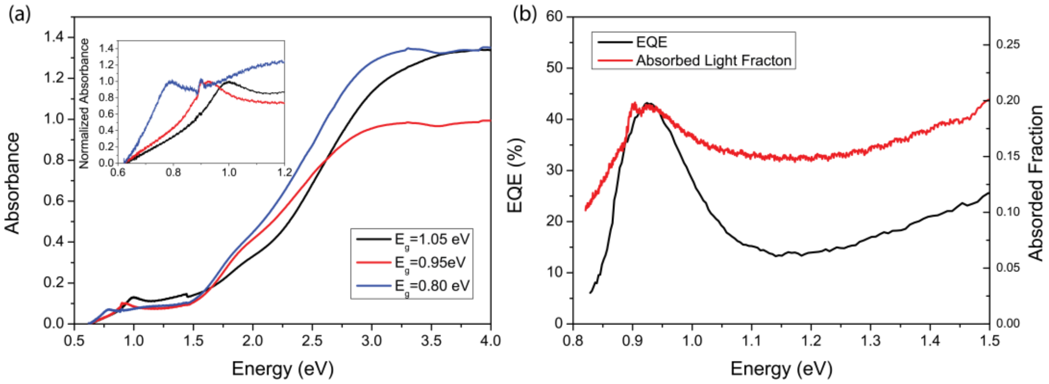

Figure 3-14: Absorption spectrum on nanorod samples. (a)Film absorbance spectra of three different bandgap PbSe nanorod samples. The inset shows the normalized absorbance of the region of the first excitonic peaks. (b) EQE and absorbed light fraction of a film of QDs (E_g=0.95 eV). The dip in measured EQE after the first absorption peak is larger than expected from the fraction of light absorbed in the device assuming a constant IQE.

In Figure 3-15 we show the IQE above $2E_g$ for all three nanoparticles sizes as a function of energy normalized to the respective bandgap energy. An ideal MEG system would show sharp increases in quantum efficiency at multiples of the bandgap. However, in common with other reports,[5,9,10,32,44,45] we find a gradual increase in efficiency above $2E_g$. The threshold energy at which this increase begins and the rate of efficiency increase above the threshold are important parameters in comparing materials systems and in determining the gain in power conversion efficiency due to MEG for a device under solar illumination. Beard et al.[4] have considered a model in which the rate of multiple exciton generation increases with energy above threshold, leading to a gradual rise in initial MEG yield as this process competes with rapid cooling. In a device, quantum efficiency enhancement depends not only on the initial yield of multiple excitons, but also on being able to rapidly separate and efficiently collect the additional charge carriers. From our data, we make the following observations: The dependence of IQE on bandgap-normalized energy is remarkably similar for all three nanorod bandgaps, exceeding 100% at around 2.9E_g in all cases and reaching 150% by 3.4E_g. This is a substantial improvement over the dot devices reported by Semonin et al.[5], where the IQE increases much more slowly with energy, not reaching 150% until nearly 5E_g. In our data it is difficult to accurately determine a threshold energy for MEG, due to the energy-dependent quantum efficiency below 2Eg that is discussed above. Clearly quantum efficiency without the assistance of MEG cannot be more than 100%, so the MEG threshold must be below 2.9E_g. Taking a quantum efficiency of 75-80% with no MEG contribution, consistent with the IQE values at the first excitonic peak, suggests an MEG threshold below 2.5E_g, and if the energy dependence of IQE in Figure 3-15 were solely due to MEG then the threshold would be close to 2E_g.

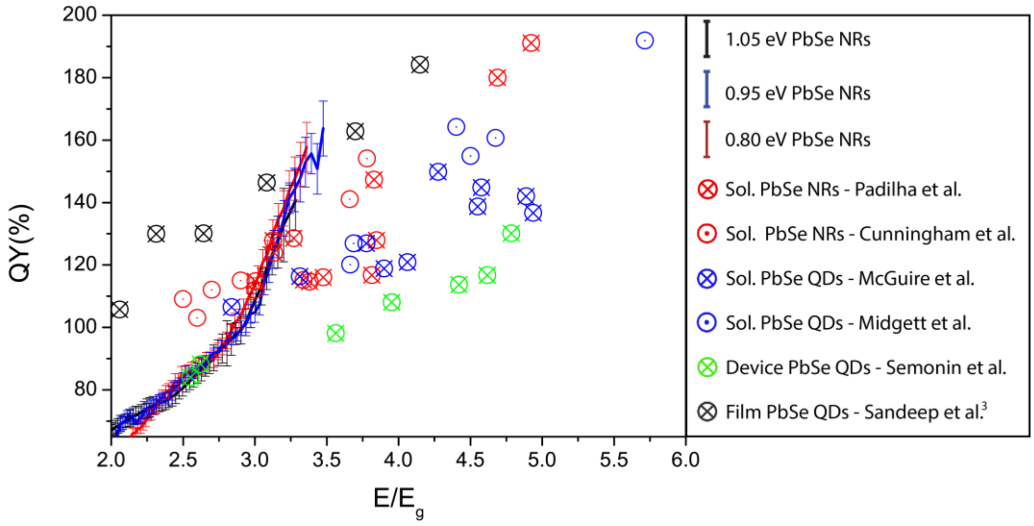

Figure 3-15: Comparison of the IQEs of PbSe NR devices (E_g = 1.05 eV, 0.95 eV and 0.80 eV) with MEG quantum yields of PbSe QDs in solution[44,45], PbSe QDs in films[5,32] and PbSe NRs in solution[9,11]. Error bars show the mean standard error of multiple independent solar cells (6 cells for 1.05 eV, 5 cells for 0.95 eV and 5 cells for 0.80 eV).

It is interesting to compare the IQE energy dependence with spectroscopic measurements of initial MEG yields in PbSe dots[44,45] and rods[9,11] in solution, also shown in Figure 3-15. Despite the fact that device IQEs are reduced by Auger recombination competing with charge separation, and by regular recombination losses, the IQEs we measure increase more rapidly with energy than the initial MEG yields in solution. This indicates that MEG is enhanced in films, an important result when attempting to make predictions about MEG in devices based on spectroscopic measurements in solution. This enhancement of MEG in films has been noted by Sandeep et al.[32], who use microwave conductivity measurements to determine MEG yields at longer times in films of PbSe dots. In those measurements, the threshold was close to $2E_g$, but the yield of additional carriers was strongly dependent on the choice of ligands, with quantum efficiencies comparable with ours seen only in films with the shortest, 1,2-ethanediamine, ligands, presumably due to the short ligands allowing rapid charge separation between nanoparticles. The reason for such a low MEG threshold energy remains unclear; mechanisms proposed include the formation of inter-particle band structure in the solid state[32] or a trap-assisted MEG mechanism[46]. Interestingly, Sandeep et al.[32] also observed inefficient charge carrier generation from MEG in PbSe dot films using the same 1,2-ethanedithiol ligand that we use here (see Figure 3-15). The difference may be due to the change from dots to rods, or due to the additional hydrazine treatment that we apply. Our measurements on nanorod devices demonstrate that carriers from MEG can not only be separated locally to contribute to microwave conductivity, but can also be collected efficiently in a solar cell structure.

Finally we estimate the contribution of MEG to the photocurrent in our devices under solar illumination. To do this, we make the (very conservative) assumption that only the fraction of the IQE in excess of 100% is due to MEG, and we weight the measured EQE by that fraction before integrating over the solar spectrum (see Figure 3-16).

We find that the short-circuit current under AM1.5G illumination is enhanced by at least 1.7%, 4.5% and 5.8% for NR bandgaps of 1.05 eV, 0.95 eV and 0.8 eV respectively. Assuming a more realistic quantum efficiency without MEG of 80% leads to enhancements as high as 12.5% for the 0.8 eV sample (Table 3-3), compared with the 4% enhancement estimated by similar methods for dot devices[5]. MEG thus contributes a substantive amount to the device efficiency, in contrast to the effects seen in bulk semiconductors such as $Si_{1-x}Ge_x$ alloys where carrier multiplication effects increase the photocurrent by at most 2%.

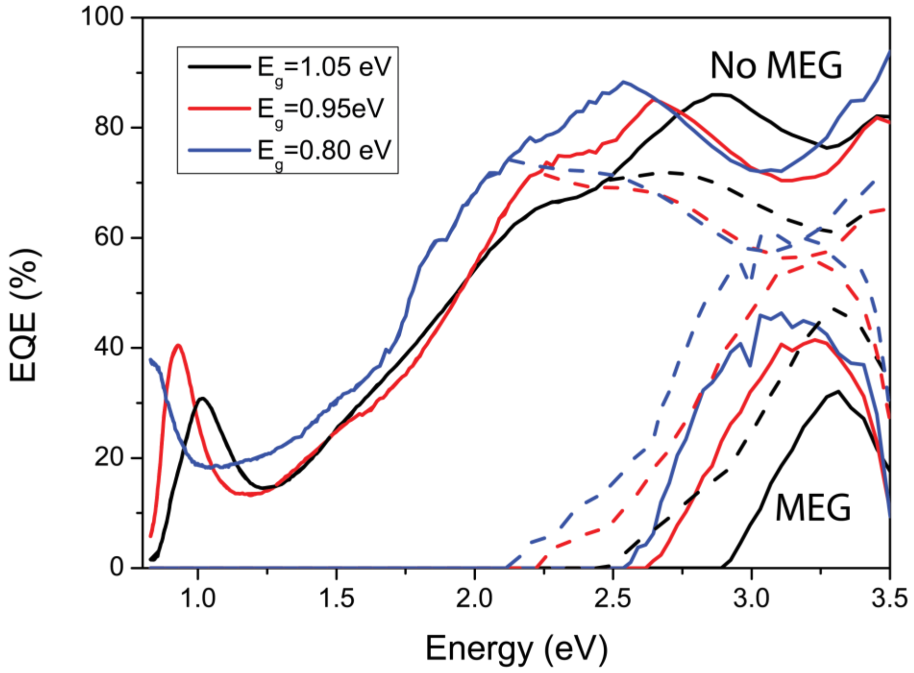

Figure 3-16: Calculated EQEs used for determining the increase in photocurrent due to MEG. The solid and dashed lines indicate the EQE assuming MEG occurs with an IQE greater than 100% or 80% respectively. The fraction of the IQE in excess of 100% or 80% is assumed to be due to MEG, and we weight the measured EQE by that fraction before integrating over the solar spectrum.

Table 3-3: Calculated MEG contribution to the short-circuit current. [a] MEG taken as an IQE greater than 100 %. [b] MEG taken as an IQE greater than 80%.

Eg (eV)	Current attributed to MEG (mA/cm^2)	Current without MEG (mA/cm^2)	Enhancement due to MEG (%)
1.05a	0.3	20.4	1.7
0.95 a	0.9	20.4	4.5
0.80 a	1.3	23.2	5.8
1.05 b	1.0	19.7	5.0
0.95 b	2.0	19.4	10.2
0.80 b	2.7	21.9	12.5

3.5 Conclusion

We have demonstrated working photovoltaic devices based on high-quality CdCl2-treated PbSe NRs of three different bandgaps. EQE values clearly exceeded 100 %, and maximum EQEs of 122% were found for the smallest-bandgap devices. Estimated IQE values were found to increase rapidly above $2E_g$, reaching values as high as 170% at only $3.5E_g$. This behavior is superior to that seen in solution-based measurements of MEG yields, and indicates potential for substantial efficiency gains in MEG-base solar cells.

3.6 On Going Research

This chapter showed that the excess energy of photo-excited charges in solar cells could be used to generate extra charges in solar cells. While we were able to report extremely high internal quantum efficiencies greater than 170% the PCE of the solar cells were quite low (0.5-2.5%). We attribute these low efficiencies to the low V_{oc} of the devises. The V_{oc} was found to be about 0.75 eV lower than the bandgap of the PbSe nanorods used. While switching the electron acceptor layer from TiO_2 to ZnO and the use of EDT/Hydrazine ligands compared to BDT was found to decrease the V_{oc} by about 0.1 eV each it is not enough to account for the large difference. The most likely source for the low V_{oc} comes from the nanocrystals surface themselves.

In an attempt to decrease the surface traps on the PbSe nanorods and potentially increase the V_{oc} of devices the idea of creating a core shell structure through cation exchange was briefly explored

3.6.1 Cation exchange core shell nanocrystals

In traditional nucleation and growth of colloidal nanocrystals, their resulting size, shape, and composition are often interdependent. Methods for independently tuning one parameter (e.g. composition) while preserving the other two (e.g. size and shape) would enable more systematic control over the resulting NC properties[37,47]. Composition can be altered post synthesis by exchanging either the cation or anion with a substitutional ion from solution. Cation exchange reactions have been shown to occur completely and reversibly in ionic nanocrystals at room temperature with unusually fast reaction rates[48]. During the diffusion and exchange of cations, the anion sub-lattice is relatively stable, leading to two important consequences. Firstly, the shapes of anisotropic NCs are generally preserved upon cation exchange, as long as the minimum dimensions of the NC are greater than the reaction zone of the exchange process. Secondly, a topotaxial relationship exists between the initial and final materials[48]. Thus, if the exchange reaction is limited to only part of the NC, a heterostructure is produced where the different compositions share a continuous anion framework[37,47,48]. Due to the high surface-to-volume ratio the entire NC lattice is accessible to solid state diffusion. The thermodynamic driving force for exchange between two cations can be controlled by the solvent and surfactant system based on their relative solvation energies in the presence of a particular coordinating species[47,49].

Briefly, PbSe nanorods were synthesized and exposed to a Cd-olate complex as per Neo et al.[50], forming a CdSe shell around the nanocrystal. From the resulting blue-shift, due to the decrease in PbSe core size we calculate a CdSe shell of 0.12 nm (Figure 3-17 a)). We see an increase in PLQE for the shelled nanorods, from 3.2% to 18.5%. When these nanorods were incorporated into devices as per Chapter 2, although they showed a decrease in JSC we do see an increase in the V_{oc} when the Cd shell is employed (Figure 3-17 b)). By taking into account the PLQE of these materials the V_{oc} loss can be estimated[51], using $kT\ln(\mathrm{PLQE})$ to be ≈ 90 and 40 meV, for core only and core shell nanorods respectively. Accounting for this loss from the maximum thermodynamically achievable V_{oc} for the core only and core shell nanorods based devices (0.95 and 0.91 eV, respectively, with respect to their bandgaps) yields a V_{oc} of around ≈0.86 V and 0.87 V. For both PV devices we find there is still an additional loss of ≈0.6-0.7 eV that can potentially arise from surface defects present in this nanocrystals. Therefore, further improvements to the V_{oc} in these systems can possibly come from improvement of the PLQEs.

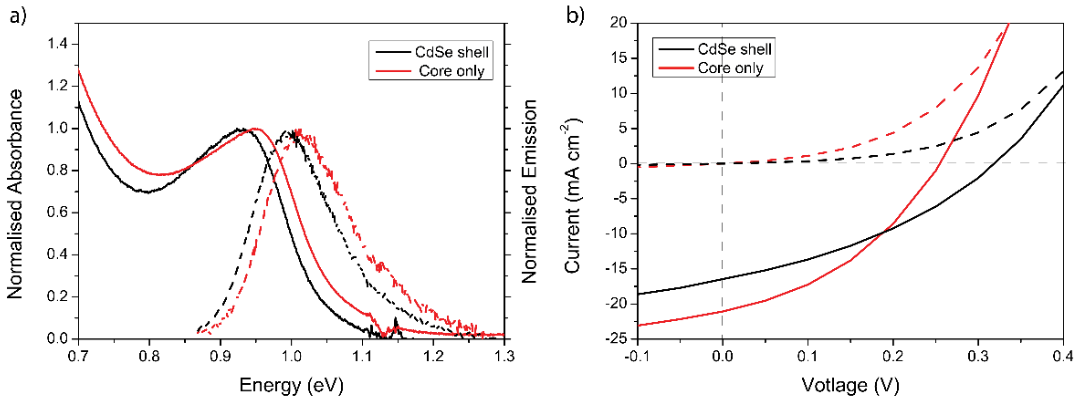

Figure 3-17: Comparison between core only PbSe and CdSe core shell PbSe nanorods. a) Absorbance and emission spectrum of PbSe nanorods before and after shelling with CdSe. b) JV curve of devices made with core only PbSe and CdSe core shell PbSe nanorods.

Further work still needs to be done to quantify these results. If it was possible to use the increased V_{oc} from adding a passivating shell to the nanocrystal while maintaining charge extraction, and thus J_{sc}, more efficient nanorod devices could be made. This could be done by looking at the effect of shell thickness and even shell composition has on photo-physical properties as well as device performance.

3.7 References

(1) Green, M. A.; Emery, K.; Hishikawa, Y.; Warta, W.; Dunopl, E. D. *Prog. Photovolt. Res. Appl.* **2014**, *22*, 701–710.

(2) Shockley, W.; Queisser, H. J. *J. Appl. Phys.* **1961**, *32*, 510.

(3) Schaller, R.; Klimov, V. *Phys. Rev. Lett.* **2004**, *92*, 186601.

(4) Beard, M. C.; Midgett, A. G.; Hanna, M. C.; Luther, J. M.; Hughes, B. K.; Nozik, A. J. *Nano Lett.* **2010**, *10*, 3019–3027.

(5) Semonin, O. E.; Luther, J. M.; Choi, S.; Chen, H.-Y.; Gao, J.; Nozik, A. J.; Beard, M. C. *Science* **2011**, *334*, 1530–1533.

(6) Smith, C.; Binks, D. *Nanomaterials* **2013**, *4*, 19–45.

(7) Midgett, A.; Luther, J.; Stewart, J. *Nano Lett.* **2013**, *13*, 3078–3085.

(8) Žídek, K.; Zheng, K.; Abdellah, M.; Lenngren, N.; Chábera, P.; Pullerits, T. *Nano Lett.* **2012**, *12*, 6393–6399.

(9) Padilha, L. A.; Stewart, J. T.; Sandberg, R. L.; Bae, W. K.; Koh, W.-K.; Pietryga, J. M.; Klimov, V. I. *Nano Lett.* **2013**, *13*, 1092–1099.

(10) Cunningham, P. D.; Boercker, J. E.; Foos, E. E.; Lumb, M. P.; Smith, A. R.; Tischler, J. G.; Melinger, J. S. *Nano Lett.* **2011**, *11*, 3476–3481.

(11) Cunningham, P. D.; Boercker, J. E.; Foos, E. E.; Lumb, M. P.; Smith, A. R.; Tischler, J. G.; Melinger, J. S. *Nano Lett.* **2013**, *13*, 3003–3003.

(12) Bartnik, A. C.; Efros, A. L.; Koh, W.-K.; Murray, C. B.; Wise, F. W. *Phys. Rev. B* **2010**, *82*, 195313.

(13) Aerts, M.; Spoor, F. C. M.; Grozema, F. C.; Houtepen, A. J.; Schins, J. M.; Siebbeles, L. D. A. *Nano Lett.* **2013**, *13*, 4380–4386.

(14) Han, L.; Liu, J.; Yu, N.; Liu, Z.; Gu, J.; Lu, J.; Ma, W. *Nanoscale* **2015**, *7*, 2461–2470.

(15) Koh, W.; Bartnik, A. C.; Wise, F. W.; Murray, C. B. *J. Am. Chem. Soc.* **2010**, *132*, 3909–3913.

(16) Pattantyus-Abraham, A.; Kramer, I. *ACS Nano* **2010**, *4*, 3374–3380.

(17) Lloyd, M. T.; Peters, C. H.; Garcia, A.; Kauvar, I. V.; Berry, J. J.; Reese, M. O.; McGehee, M. D.; Ginley, D. S.; Olson, D. C. *Sol. Energy Mater. Sol. Cells* **2011**, *95*, 1382–1388.

(18) Beek, W. J. E.; Slooff, L. H.; Wienk, M. M.; Kroon, J. M.; Janssen, R. A. J. *Adv. Funct. Mater.* **2005**, *15*, 1703–1707.

(19) Langford, R. M.; Rogers, M. *Micron* **2008**, *39*, 1325–1330.

(20) Paul, G.; Sen, S. *Mater. Lett.* **2002**, *57*, 742–746.

(21) Ehrler, B.; Walker, B. J.; Böhm, M. L.; Wilson, M. W. B.; Vaynzof, Y.; Friend, R. H.; Greenham, N. C. *Nat. Commun.* **2012**, *3*, 1019.

(22) Tabachnyk, M.; Ehrler, B.; Bayliss, S.; Friend, R. H.; Greenham, N. C. *Appl. Phys. Lett.* **2013**, *103*, 153302.

(23) Burkhard, G. F.; Hoke, E. T.; McGehee, M. D. *Adv. Mater.* **2010**, *22*, 3293–3297.

(24) Ip, A. H.; Thon, S. M.; Hoogland, S.; Voznyy, O.; Zhitomirsky, D.; Debnath, R.; Levina, L.; Rollny, L. R.; Carey, G. H.; Fischer, A.; Kemp, K. W.; Kramer, I. J.; Ning, Z.; Labelle, A. J.; Chou, K. W.; Amassian, A.; Sargent, E. H. *Nat. Nanotechnol.* **2012**, *7*, 577–582.

(25) Asil, D.; Walker, B. J.; Ehrler, B.; Vaynzof, Y.; Sepe, A.; Bayliss, S.; Sadhanala, A.; Chow, P. C. Y.; Hopkinson, P. E.; Steiner, U.; Greenham, N. C.; Friend, R. H. *Adv. Funct. Mater.* **2014**, *25*, 928–935.

(26) Cho, K.-S.; Talapin, D. V; Gaschler, W.; Murray, C. B. *J. Am. Chem. Soc.* **2005**, *127*, 7140–7147.

(27) Baker, J. L.; Widmer-Cooper, A.; Toney, M. F.; Geissler, P. L.; Alivisatos, A. P. *Nano Lett.* **2010**, *10*, 195–201.

(28) Boercker, J. E.; Foos, E. E.; Placencia, D.; Tischler, J. G. *J. Am. Chem. Soc.* **2013**, *135*, 15071–15076.

(29) Brown, P.; Kim, D.; Lunt, R.; Zhao, N. *ACS Nano* **2014**, *8*, 5863–5872.

(30) Chuang, C.; Brown, P.; Bulović, V.; Bawendi, M. *Nat. Mater.* **2014**, 1–6.

(31) Ehrler, B.; Musselman, K. *ACS Nano* **2013**, *7*, 4210–4220.

(32) Sandeep, C. S. S.; ten Cate, S.; Schins, J. M.; Savenije, T. J.; Liu, Y.; Law, M.; Kinge, S.; Houtepen, A. J.; Siebbeles, L. D. A. *Nat. Commun.* **2013**, *4*, 2360–2366.

(33) Gao, Y.; Aerts, M.; Sandeep, C. S. S.; Talgorn, E.; Savenije, T. J.; Kinge, S.; Siebbeles, L. D. A.; Houtepen, A. J. *ACS Nano* **2012**, *6*, 9606–9614.

(34) Look, D.; Reynolds, D.; Sizelove, J. *Solid State Commun.* **1998**, *105*, 399–401.

(35) Yagi, E.; Hasiguti, R.; Aono, M. *Phys. Rev. B* **1996**, *54*, 7945–7956.

(36) Willis, R.; Olson, C.; O’Regan, B. *J. Phys. Chem. B* **2002**, *106*, 7605–7613.

(37) Rivest, J. B.; Swisher, S. L.; Fong, L.-K.; Zheng, H.; Alivisatos, A. P. *ACS Nano* **2011**, *5*, 3811–3816.

(38) Nayak, P. K.; Garcia-Belmonte, G.; Kahn, A.; Bisquert, J.; Cahen, D. *Energy Environ. Sci.* **2012**, *5*, 6022.

(39) Yang, L.; Tabachnyk, M.; Bayliss, S. *Nano Lett.* **2015**, *15*, 354–358.

(40) Congreve, D. N.; Lee, J.; Thompson, N. J.; Hontz, E.; Yost, S. R. *Science* **2007**, *340*, 334–337.

(41) Hillhouse, H. W.; Beard, M. C. *Curr. Opin. Colloid Interface Sci.* **2009**, *14*, 245–259.

(42) Fuke, N.; Hoch, L.; Koposov, A. *ACS Nano* **2010**, *4*, 6377–6386.

(43) Law, M.; Luther, J.; Beard, M. *Photovolt. Spec. Conf. 2009 34th IEEE* **2009**, 2068–2073.

(44) McGuire, J. A.; Joo, J.; Pietryga, J. M.; Schaller, R. D.; Klimov, V. I. *Acc. Chem. Res.* **2008**, *41*, 1810–1819.

(45) Midgett, A. G.; Hillhouse, H. W.; Hughes, B. K.; Nozik, A. J.; Beard, M. C. *J Phys. Chem. C* **2010**, 17486–17500.

(46) Allan, G.; Delerue, C. *Phys. Rev. B* **2009**, *79*, 195324.

(47) Luther, J. M.; Zheng, H.; Sadtler, B.; Alivisatos, A. P. *J. Am. Chem. Soc.* **2009**, *131*, 16851–16857.

(48) Son, D. H.; Hughes, S. M.; Yin, Y.; Paul Alivisatos, A. *Science* **2004**, *306*, 1009–1012.

(49) Sadtler, B.; Demchenko, D. O.; Zheng, H.; Hughes, S. M.; Merkle, M. G.; Dahmen, U.; Wang, L.-W.; Alivisatos, A. P. *J. Am. Chem. Soc.* **2009**, *131*, 5285–

5293.

(50) Neo, D. C. J.; Cheng, C.; Stranks, S. D.; Fairclough, S. M.; Kim, J. S.; Kirkland, A. I.; Smith, J. M.; Snaith, H. J.; Assender, H. E.; Watt, A. A. R. *Chem. Mater.* **2014**, *26*, 4004–4013.

(51) Ross, R. T. *J. Chem. Phys.* **1967**, *46*, 4590–4593.

4 ANTENNA COMPLEXES FOR LUMINESCENT SOLAR CONCENTRATORS

4.1 Abstract

Luminescent solar concentrators (LSCs) are waveguides doped with luminescent centers that can spectrally and spatially concentrate sunlight. They can reduce the cost of photovoltaic energy production and are attractive prospects for photobioreactors and building-integrated applications. Reabsorption, caused by non-zero overlap between the absorption and emission spectra of the light-emitting centers, often limits LSC efficiency. Donor-acceptor energy-transfer complexes are one method to mitigate reabsorption by shifting the emission away from the main absorption peak. Here we introduce versatile star-shaped donor-acceptor molecules based on a central BODIPY energy acceptor with oligofluorene donor side units. Varying the oligofluorene chain length alters the relative oscillator strengths of the donor and acceptor, changing the severity of reabsorption for a given donor density, but also changing the luminescence yield and emission spectrum. We performed comprehensive device measurements and Monte Carlo ray tracing simulations of LSCs containing three oligofluorene-BODIPY donor-acceptor systems with different oligofluorene chain lengths, and then extended the simulation to study hypothetical analogs with higher donor-acceptor ratios and different terminal acceptors. We found that the measured structures permit waveguide propagation lengths on a par with

state-of-the-art nanocrystalline emitters, while the proposed structures are viable candidates for photobioreactor and energy production roles and should be synthesized.

This work was published in the Journal of Materials Chemistry C: Star Shaped Oligomers to Minimize Reabsorption Losses in Luminescent Solar Concentrators. Authors: Davis, N J. L. K.; MacQueen, R.; Jones, S. T. E.; Orofino, C.; Cortizo-Lacalle, D,; Taylor, R.; Credgington, D.; Skabara, P. J.; and Greenham, N. C. DOI: 10.1039/C6TC05298C

All the below work was carried out by myself except where stated. Dr Rowan W. MacQueen wrote the simulation. Mr. Saul T.E. Jones cut and polished the LSCs.

4.2 Introduction

Luminescent solar concentrators (LSCs) consist of a transparent waveguide doped with highly luminescent chromophores. Sunlight incident on the LSC is absorbed by the chromophores and emitted into waveguide modes, confining the light for transport to a useful output[1]. As the input aperture of an LSC is larger than the output aperture, LSCs can concentrate light spatially as well as spectrally. Photovoltaic (PV) cells can be attached to the output aperture, increasing the photon flux available to the cell compared to direct illumination by sunlight[2–4]. The narrow emission spectrum of the LSC can also be tuned to improve conversion efficiency[4]. The primary motivation for this LSC-PV combination has traditionally been the high cost of PV cells, with the LSCs intended as a cheap replacement for large areas of expensive cell. However, as the cost of PV modules has decreased, other applications are under consideration. The aesthetic and structural properties of LSCs are being viewed as increasingly important[1]. PV modules in general are heavy, non-structural, and available in limited colors, while LSCs are light, can be formed into a range of shapes and as part of structures, and are colorful. This makes them a strong prospect for integration into energy-generating structures[2–4]. In addition, LSCs are being explored as a means to enhance photobioreactors[5], as daylighting sources[6] and as antennae for visible-light communications[7].

The power conversion efficiency (PCE) of an LSC is given by $PCE \approx \eta_{abs}\eta_{stokes}\eta_{em}\eta_{prop}(G)$, where η_{abs} is the absorbed fraction of the solar spectrum,

η_{stokes} is the fraction of energy lost in down conversion, η_{em} is the probability of remission into waveguide modes, and η_{prop} accounts for all the propagation-related losses. G, the geometric ratio, is the ratio of input to output aperture areas[8–10]. The need to guide light over long distances within a heavily-doped matrix means reabsorption typically dominates the losses embedded in η_{prop}[4,11,12], except in unusual cases of emitters with very large Stokes shifts where parasitic matrix losses take over[13].

Reabsorption can be diminished by increasing the Stokes shift of the emitting chromophore[14], or through separating the absorbing and emitting chromophores and minimizing the concentration of the latter[15–17]. Increasing Stokes shift directly is typically pursued for inorganic emitters such as quantum dots, where varying composition and size, and the use of core-shell structures, allow the absorption and emission properties to be controlled[18,19]. For organic molecules where the Stokes shift may be considered intrinsic, the donor-acceptor strategy is prevalent, and many LSCs using donor-acceptor systems based on Förster resonance energy transfer (FRET) have been reported[20–24]. FRET permits efficient radiationless energy transfer between donors and acceptors, but only if the coupled molecules are within ≈ 5 nm of each other[16,25–27]. This degree of proximity in molecules containing large π-systems often leads to aggregation and decreased photoluminescence quantum efficiencies (PLQEs)[28–32], which hinder LSC performance. Combining the donor and acceptor species into one supramolecule can avoid this problem, albeit at the price of increased synthetic complexity[16,33]. One of the best examples of a donor-acceptor supramolecular system is the bacterial phycobilisome (Figure 4-1 (b)). Phycobilisomes are highly organized complexes of different protein chromophores and linker peptides arranged to produce rapid and directional energy migration to a central core emitter[34]. Indeed phycobilisomes have been used directly in novel LSCs[16].

Boron-dipyrromethene (BODIPY) conjugated systems are a popular class of organic dyes that show high fluorescence yields and absorptivity, good photostability, and solubility in common solvents[35–38]. BODIPY dyes have been used as biological labels[39–41], laser dyes[42–44], monomer units in low- polymers[45–47], and in LSCs[15,48]. Due to aggregation, achieving efficient emission from a BODIPY dye in the solid state is difficult, but this can be remedied by incorporating the BODIPY core into a larger molecular scaffold[49–52]. In this work, we investigate LSCs containing a novel donor-acceptor system based on a central BODIPY emitter with three covalently-bound oligofluorene donor side units arranged in a star configuration (OFBMs, Figure 4-1(a))[33]. The oligofluorene side units absorb light and transfer energy via FRET to the BODIPY core, where it is emitted. We study the effect of a systematic increase in the number of fluorene units per molecule.

The emission peak of the BODIPY core used in this work, at 610 nm (Figure 4-2 (a)), would not produce an effective LSC based on silicon PV cells. However, many proposed photo-bioreactors for the cultivation of microalgae are too expensive for practical applications due to the high cost of providing artificial illumination[53]. Further, it has been shown that spectral tuning can be used to improve growth efficiency for certain strains of microalgae and plants[54,55]. Thus LSCs based on OFBMs represent potentially useful candidates for lighting systems used in bioreactors[56]. Optimizing LSC efficiency is still important in this application. Through a concerted device and raytracing study, we find that interplay between the different effects of extending the oligofluorene donor arms mean simple heuristics for optimizing LSC efficiency are inadequate. Extending the OFBM structure through simulated spectra, we find that this family of donor-acceptor molecules holds promise for low-reabsorption LSC applications.

4.3 Methods

Synthesis of Oligofluorenes molecules: The oligofluorenes molecules used in this study were synthesized with a modified Suzuki coupling using K_3PO_4[33]. Synthetic yields were between 29-58%. All molecules showed good thermal stability with decomposition temperatures above 400°C.

Steady-state spectral measurements: Absorption spectra were measured using a HP 8453 spectrophotometer. Dye samples were dispersed in toluene at a concentration of ca. 1 mg ml^{-1} and a 1 mm path length was used. Film absorption spectra were measured using off-cuts from the produced LSCs. LSCs containing no active molecules were used as the blank. Photoluminescence measurements of solutions (1 mg ml^{-1} in toluene in a 1 mm cuvette) and films (thin off-cuts of the fabricated LSCs) including two-dimensional scans were measured on an Edinburgh Instruments FLS90 fluorimeter. The two-dimensional scans were normalized to the excitation intensity at each excitation wavelength

LSC fabrication: LSCs were formed by dissolving the chosen OFBM at ≈0.015 mM in a 4:1 solution of lauryl methacrylate (LMA) and ethylene glycol dimethacrylate (EGDM). The 4-methoxyphenol inhibitor, supplied with the monomers, was removed by passing the monomer solution over basic aluminum oxide. 2,2-dimethoxy-2-phenyl acetophenone (1 wt.%) was added as an initiator and stirred until completely dissolved. The solution was placed in a mold made by two sheets of glass clamped together with a 0.3 cm thickness o-ring in-between. The o-ring in the mold sets the thickness of the LSCs to 0.3 cm. Polymerization occurred by exposure to 365 nm radiation for 5 hours. LSCs were cut and polished into 10 x 10 x 0.3 cm slabs.

LSC measurements: The LSCs were coupled to four 10 x 0.3 cm silicon PV cells (Sunpower, Slimfast C60E M 135, cut to size and connected in series, 0.55 % PCE) and current–voltage characteristics, and thus efficiency, were measured under AM 1.5G conditions using an Abet Sun 2000 solar simulator, at an intensity equivalent to 100 mW cm^2 after correcting for spectral mismatch, using a Keithley 2635 source measure unit. Current–voltage characteristics using a transparent LSC matrix without chromophores was also recorded to account for direct illumination of the PV cells by scattering of the excitation source; this contribution was subtracted.

LSC spatially-resolved EQE: For the spatial EQE measurements the LSC was illuminated by a 2x2 mm square of AM 1.5G solar radiation and overall current of the photodiodes was recorded at each (x, y) coordinate.

LSC edge emission: Spectral emission as function of depth measurements were performed using a 523 nm laser pointer as the excitation source and edge emission was measured using a Labsphere CDS-610 spectrometer.

LSC spectrally-resolved EQE: A 100-W tungsten halogen lamp (400–1,500 nm) dispersed through a monochromator (Oriel Cornerstone 260) and a set of silicon diodes (ThorLabs SM05PD1A) was used for EQE measurements. A Keithley 2635 source measurement unit was used to measure the short-circuit current as a function of wavelength. The incident light was focused to a spot size of ca. 1 mm^2 using a set of lenses to illuminate the photodiode or LSC. For the LSC measurements the silicon photodiode was placed on the edge of the LSCs. The excitation position was in the center of the LSC, 5 mm from the edge.

Simulations: The LSC ray trace model was constructed in Matlab and has been previously reported[57]. LSC geometry was modelled as a square planar slab with a depth of 0.3 cm. The side length and dye concentration could be varied. In the simulation, unpolarized light, either drawn from the AM1.5G spectrum or at a specific wavelength, arrived on the upper face of the LSC at normal incidence. The absorption of sunlight and reabsorption of photoluminescence was determined probabilistically using the Beer–Lambert law. Wavelengths of incident and emitted photons were selected using the interpolation of a random unit scalar onto the relevant cumulative distribution function. Fresnel reflections and total internal reflection were simulated assuming a waveguide refractive index, $n = 1.5$, and air cladding ($n = 1.0$). The simulated LSCs had a uniform dye distribution throughout the matrix, corresponding with the calculated concentration of the fabricated LSC devices. Each LSC was simulated with 10^6 incident photons; current was counted by logging photons traversing output apertures (the slab edges).

4.4 Results

4.4.1 Light harvesting antenna complexes

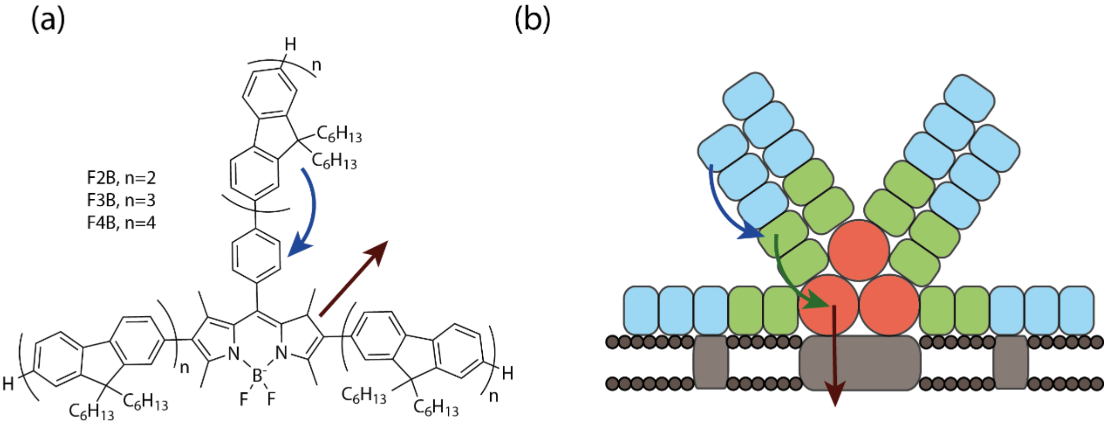

Figure 4-1: Light harvesting antenna complexes. (a) The structures of the star-shaped oligofluorenes with BODIPY cores, FnB (n= 2-4). Arrows indicate energy transfer from the fluorene donors and emission from the BODIPY acceptor. (b) Structure of a phycobilisome with arrows showing transfer of excitons through the phycoerythrins (blue), phycocyanins (green) and allophycocyanis (red) to the thylakoid membrane (grey).

4.4.2 Steady-state optical properties of OFBMs

The OFBM molecules are named by the convention FnB, where n is the number of 9,9-dihexylfluorene units per arm. Molecules with n = 2, 3 and 4 were used (Figure 4-1 (a)), corresponding to 6, 9 and 12 fluorene units per BODIPY core. The OFBMs have a molar absorptivity of ≈ 80,000 $M^{-1}cm^{-1}$ in the BODIPY region and ≈ 30,000 $M^{-1}cm^{-1}$ per fluorene unit in the donor absorption region (Figure 4-2).

Moving from F2B through to F4B increases the intensity of the 350 nm absorption peak, due to the increased number of fluorene units, while the BODIPY peak intensity is unchanged. The position of the absorbance peak associated with the fluorene units undergoes a bathochromic shift of 13 nm per fluorene unit added to an arm (Figure 4-3). This is due to extension of π conjugation through the oligofluorene arms[33].

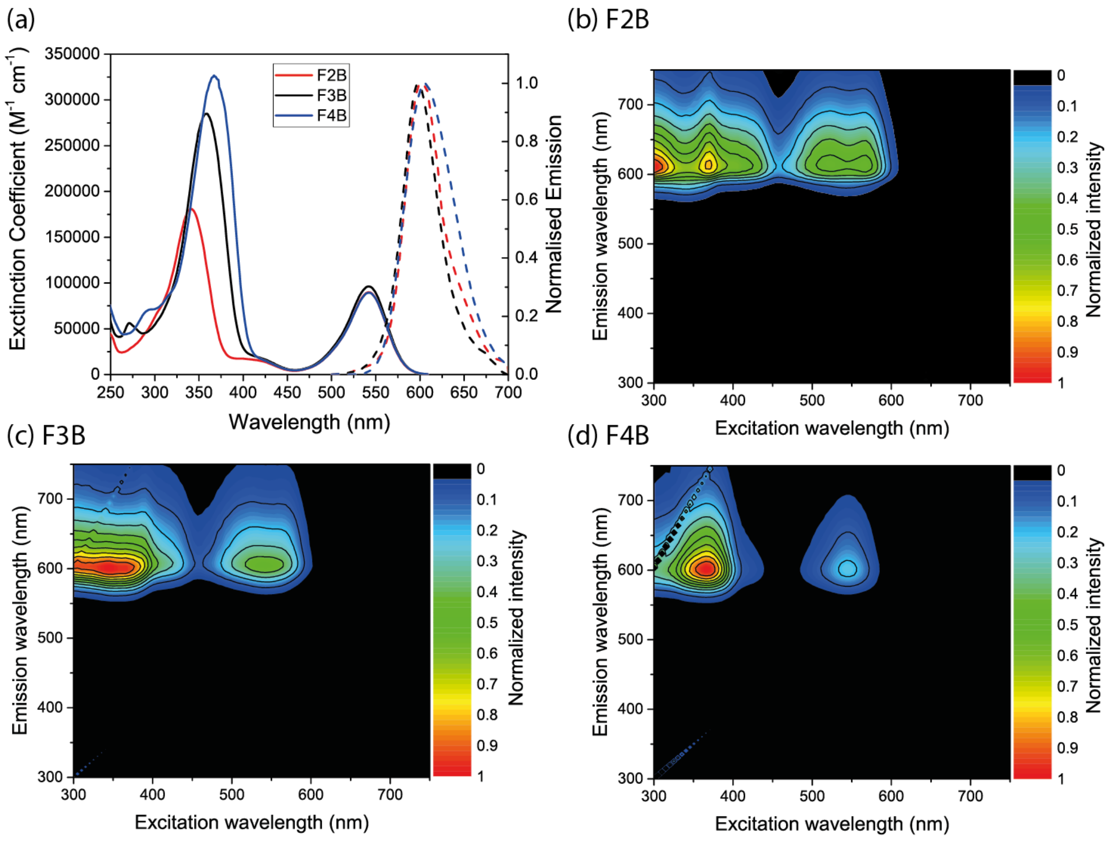

Figure 4-2: Photophysical properties of OFBMs in solution. (a) Extinction and emission spectra of OFBMs in solution. (b)-(d) Two-dimensional emission/excitation spectra clearly showing that, under any excitation, emission occurs from the BODIPY core at 610 nm.

Two-dimensional excitation-emission fluorescence spectra of the OFBMs (Figure 4-2 (b-d)) were collected at low optical density to minimize the inner filter effect. The spectra show that fluorescence occurs solely from the BODIPY core, much like in a phycobilisome. This suggests a high donor-acceptor energy transfer efficiency, which is in agreement with previous reports[33,58]. The increase in emission intensity for excitation at 360 nm compared to 540 nm correlates with the number of fluorene units. PLQEs were 0.70, 0.75 and 0.66 for F2B, F3B and F4B respectively, measured using a standard quinine disulfate reference[58].

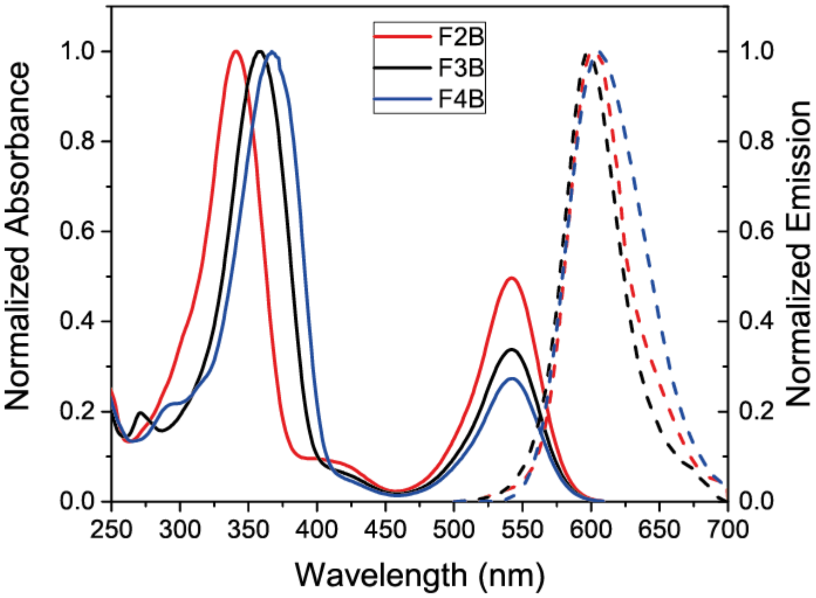

Figure 4-3: Normalized absorbance and emission of the oligofluorene molecules in toluene.

4.4.3 LSC fabrication

Three LSCs were fabricated using a polymer matrix of lauryl methacrylate (LMA):ethylene glycol dimethacrylate (EGDM) (4:1 by volume) doped with OFBM, prepared as described in the Methods section to give 10 cm × 10 cm × 0.3 cm waveguides. EGDM is a cross-linker that minimizes volume change during polymerization, producing a rigid blend that is transparent in the visible[13,18,59–61]. The LSCs showed pronounced light emission from the narrow edges when excited with 365 nm and 532 nm illumination (Figure 4-4 (a) and Figure 4-5). No changes in the dye absorption spectra were seen upon incorporation into the polymer matrix. Emission spectra showed a blue-shift relative to solution for all OFBMs (F2B ≈ 15 nm, F3B ≈ 10 nm, F4B ≈ 20 nm) (Figure 4-4 (b)-(d)). We attribute this to a change in the microenvironment of the BODIPY center, which is known to shift the emission spectrum[62]. The concentration of OFBM in the LSCs was 0.0130 mM, 0.0176 mM and 0.0126 mM for F2B, F3B and F4B respectively, as determined by absorption measurements.

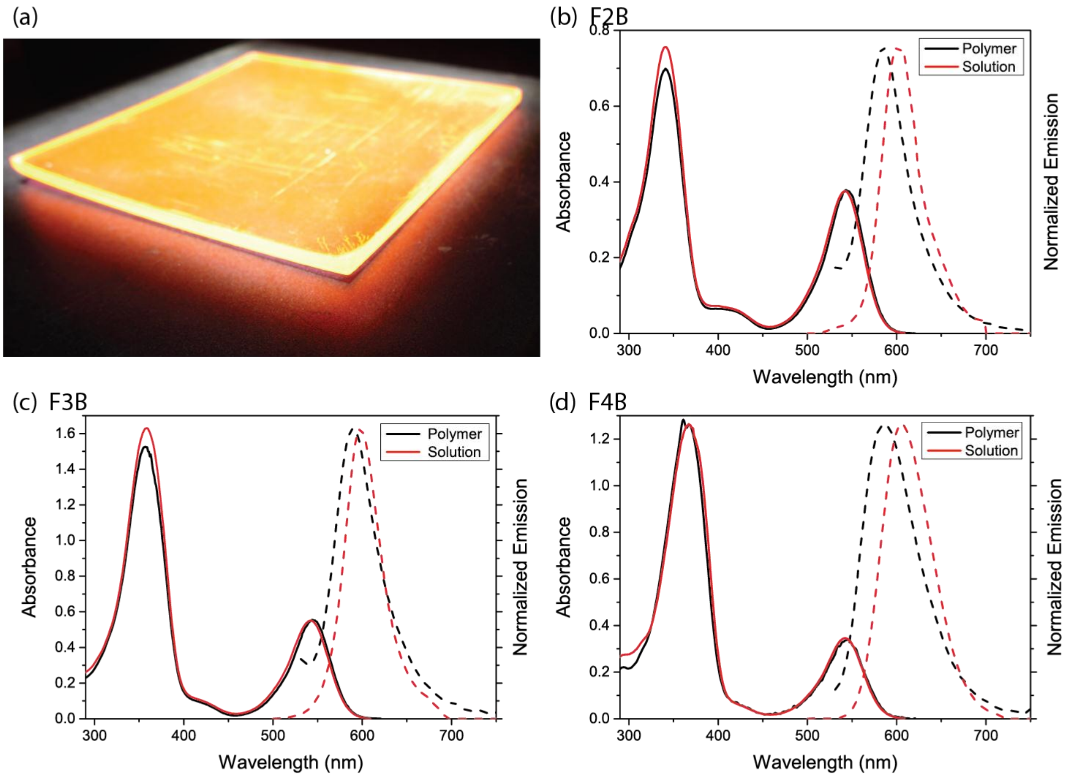

Figure 4-4: Fabricated LSCs. (a) LSC (F2B) photoexcited at 365 nm. Measured absorption and normalized emission of the LSCs (b) F2B, (c) F3B and (d) F4B.

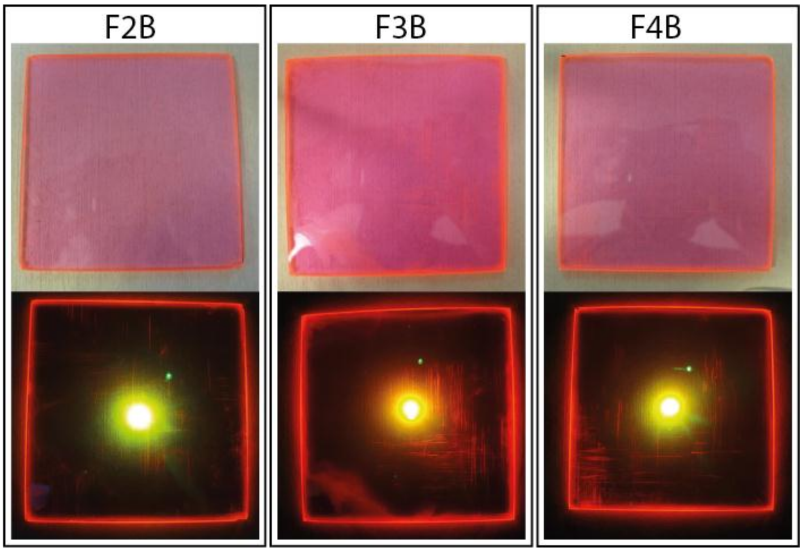

Figure 4-5: Images of the fabricated LSC devices and the devices under 523 nm excitation. Bright spot in the center of the bottom image is the excitation spot.

4.4.4 LSC external quantum efficiency and flux gain

While the application of LSCs using the OFBMs studied is not anticipated to be in PV power generation, PV cells were used as convenient photodetectors in most of our device characterizations. Here, each LSC was coupled to four 10 x 0.3 cm silicon PV cells. No index matching between the LSC and PV cells was carried out. The current–voltage (I-V) characteristic of each LSC-PV system under AM 1.5G illumination was measured and used to calculate the external quantum efficiency (EQE), the ratio between the number of photons leaving the output aperture and the number of incident photons entering the input aperture. Using the measured absorption spectrum, we also calculated the internal quantum efficiency (IQE), the ratio of edge-emitted photons to photons absorbed by the LSC. EQEs and IQEs were simulated using the LSC raytrace program (see Methods section) with the experimental parameters of concentration, absorbance and emission spectra, PLQY and device geometry as inputs. Measured and simulated EQEs and IQEs are shown in Table 4.

Using the simulation results, we calculated the flux gain, a detection-agnostic metric given by the ratio of photons leaving the output aperture to photons arriving over an equivalent area of the input aperture, for photons with energy exceeding a threshold value. For the three OFMBs measured, we chose a threshold of 700 nm, amenable to photobioreactors or some thin-film PV cells[53,63]. The flux gain at 700 nm (denoted F700) is shown in Table 4.

Table 4: Measured and simulated external and internal quantum efficiencies, and the calculated flux gain at 700 nm.

Sample	Measured EQE (%)	Simulated EQE (%)	Measured IQE (%)	Simulated IQE (%)	F700
F2B	1.69±0.15	1.71±0.02	36.4±3.3	37.6±0.3	0.47±0.02
F3B	2.44±0.33	2.73±0.03	38.2±5.2	42.8±0.2	0.76±0.04
F4B	1.82±0.17	1.91±0.02	34.7 ±3.2	36.5±0.4	0.53±0.04

The relatively narrow absorption bandwidth of the OFBMs means that much of the solar spectrum is not absorbed, thus it is unsurprising that the maximum measured

EQE is only 2.44%, for F3B. F2B and F4B have EQEs of 1.69% and 1.82%, respectively. However, IQE values, which are not sensitive to incomplete absorption, are relatively high. F3B has an IQE of 38.4%, while F2B and F4B have IQEs of 36.4% and 34.7% respectively. There is good agreement between measurement and simulation results, which suggests raytracing can clarify the overlapping effects of changing PLQEs and emission spectrum blue-shifts among the three FnB materials. The calculated F700 values show a similar spread, peaking at 0.76 for F3B. We note that a sub-unity flux gain is unsurprising for the small size of the devices produced (G=8.3), and we show later that positive flux gain is predicted at a slightly larger G.

These results demonstrate that to understand the effect of oligofluorene length on LSC performance, it is necessary to consider not just the influence of increasing donor relative to acceptor oscillator strength as the arms are lengthened, but also the effects of spectral shifts and changes in PLQE.

4.4.5 **Spatially-dependent external quantum efficiency**

Spatially-dependent EQE was measured by scanning a 2 x 2 mm square of AM 1.5G radiation across the surface of each LSC-PV device while measuring short-circuit photocurrent. 121 points were measured per device and then averaged over the four quadrants. EQE(x,y) was then calculated by dividing the total detected photocurrent, in units of e, by the incident photon flux. Simulations were conducted by spatially constraining the excitation source in the raytracer to mimic the grid of measurement points, and calculating EQE for each grid point. Measured and simulated results are presented in Figure 4-6 (a) and (b), respectively, and a one-dimensional comparison is shown in Figure 4-6 (c). A more detailed comparison between the measurements and simulations is presented in Figure 4-7.

The low EQEs measured are again largely due to the high proportion of AM1.5G photons that are not absorbed by the OFBMs; our analysis therefore focuses on relative changes to the EQE with respect to excitation position, with the aim of clarifying the extent of reabsorption in these three devices. EQE (x,y) was found to decrease for all three devices as the excitation source was moved further from the edges, reflecting the greater likelihood of photon loss through reabsorption-driven nonradiative decay, outcoupling, and parasitic matrix processes as the average path length to reach the edge is increased. The simulation results agree reasonably well with the measurements, over-estimating the measured result by 5.2±1.5% at the outside corner positions. This difference is ascribed to an imperfect fabricated waveguide and PV cell optical coupling which is not accounted for in the simulations. The simulated and measured EQEs from the middle of the device differ by 9.2±0.7%, relative to each other; the additional difference seen here between experiment and simulation is accounted for by parasitic matrix losses which increase with path length and are not included in the simulations.

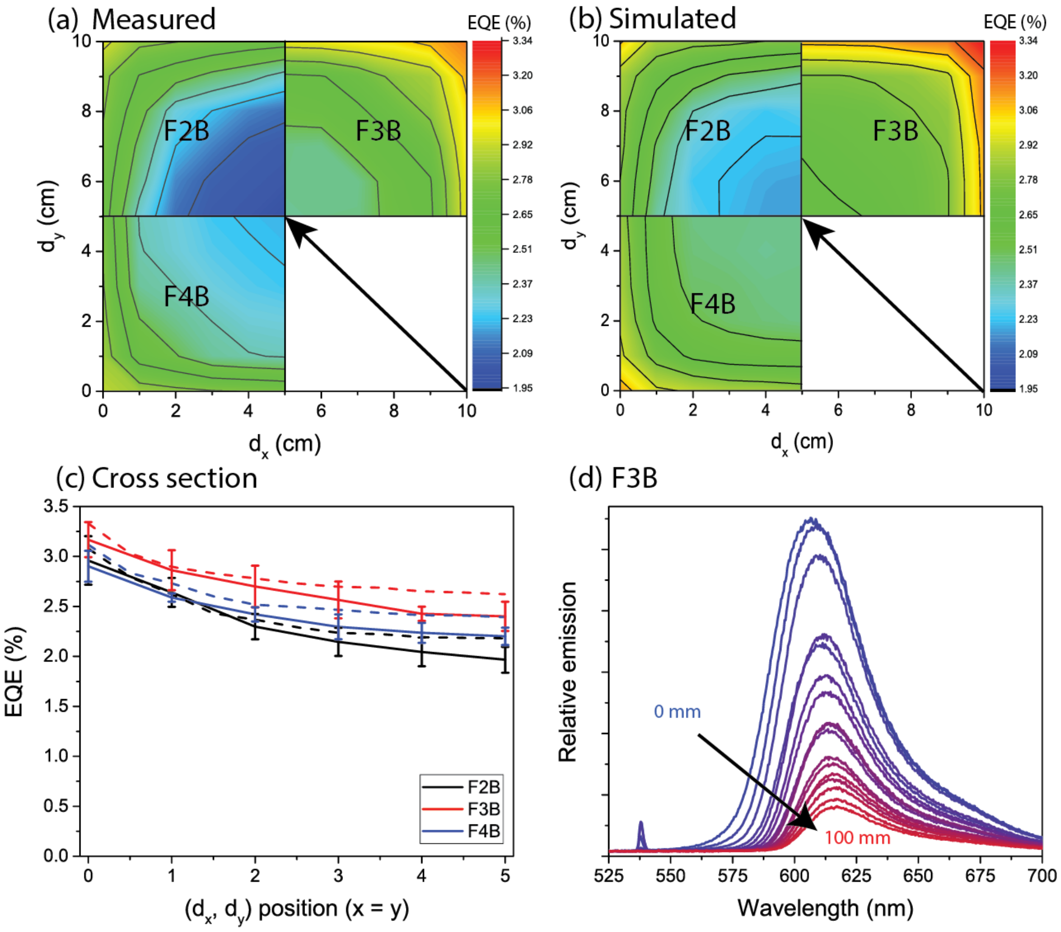

Figure 4-6: Spatially dependent EQEs and edge emission from the fabricated LSCs. (a) Spatial maps of LSC EQE, reflecting the probability of incident sunlight generating emission from an LSC edge. Excitation was from a 2x2 mm square of AM 1.5G solar radiation. (b) Simulated results. Data represent counts collected from 10^6 incident photons. (c) EQE moving along a diagonal line drawn from the corner of the device to the center, for the measured data (solid line) and simulated data (dashed line). (d) Spectral changes in LSC edge emission spectra with excitation distance for the F3B LSC device. The peak at 532 nm is an artefact from the excitation spot

The relative drop in EQE for excitation in the middle of the LSC (x = y = 5 cm) compared to excitation directly adjacent to a corner is 32.1±3.4% for F2B, 24.2±2.0% for F3B and 24.2±1.6% for F4B. Although the F3B LSC has a higher OFBM concentration than the others, this is counteracted by the slightly greater PLQE and smaller emission spectrum blue-shift of the molecule. The measured waveguide propagation losses are smaller than those reported for some simple nanocrystal devices, such as standard PbS (70% loss for a length of 8 cm[64]), and are approaching those of recently-reported core/shell CuInSexS2-x/ZnS nanocrystals (30% loss at 12 cm[18]). Given the clear sensitivity of BODIPY core reabsorption loss to emission blue-shift and changes in PLQE, small improvements in both properties, which should be achievable by modifying the matrix material, will yield a very effective LSC emitter.

The degree of reabsorption associated with increased propagation length is determined by the spectral overlap between the luminophore emission and its absorbance spectrum. The spectrum of the emission from the output aperture was recorded as the propagation length increased. Excitation was by a 532 nm laser beam. All three LSCs showed a red shift in emission and a decrease in intensity with increasing distance (Figure 4-6 (d)) and Figure 4-8 (a) (c) and (e)). These shifts stabilized at long path lengths as bluer photons were selectively eliminated by reabsorption. We simulated these results (Figure 4-8 (b) (d) and (f)), mimicking the narrow detection aperture and excitation source in the raytrace. The simulation results reproduce the experimental data to a large degree, showing the same trends in red-shift and intensity with increasing propagation length.

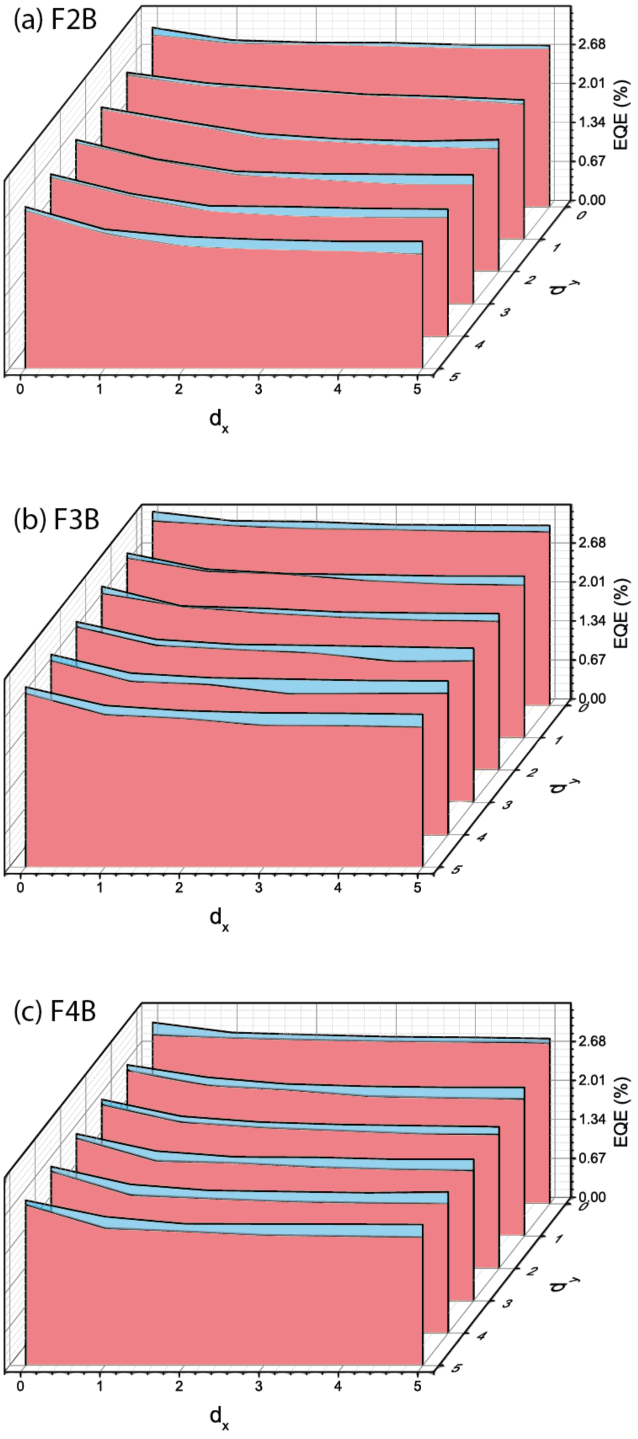

Figure 4-7: Comparison between measured (red) and simulated (blue) EQE for x,y coordinates. (a) F2B, (b) F3B and (c) F4B.

(a) F2B - Measured (b) F2B - Simulated

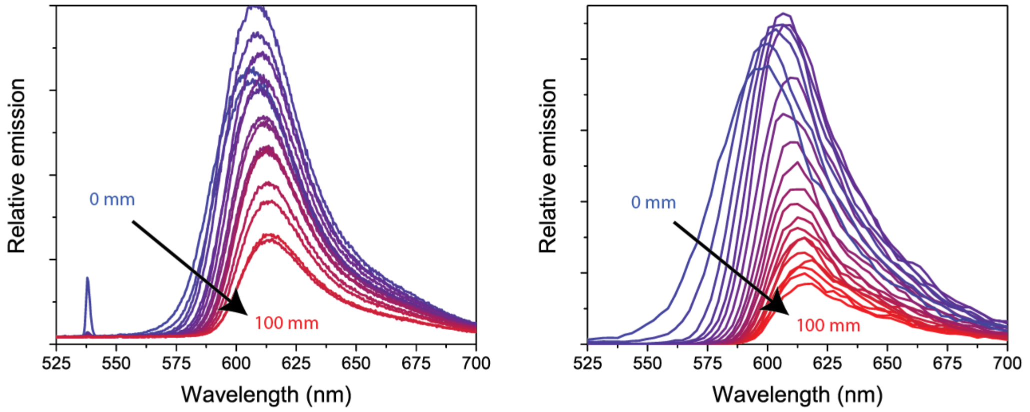

(c) F3B - Measured (d) F3B - Simulated

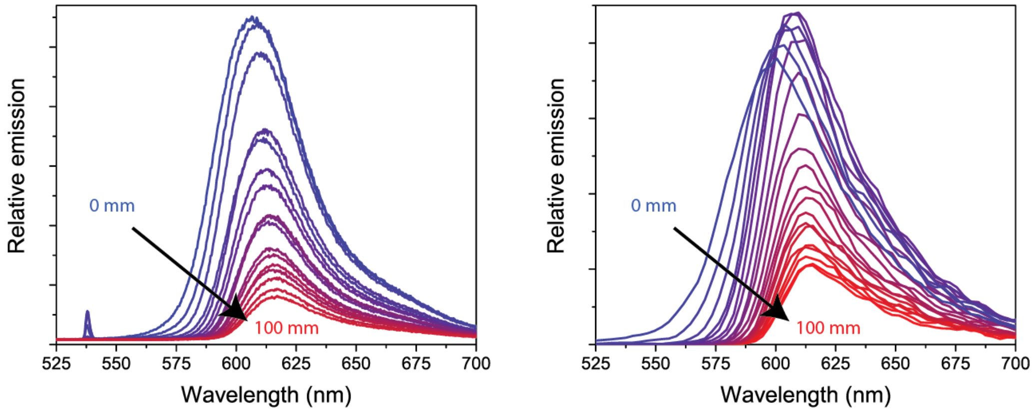

(e) F4B - Measured (f) F4B - Simulated

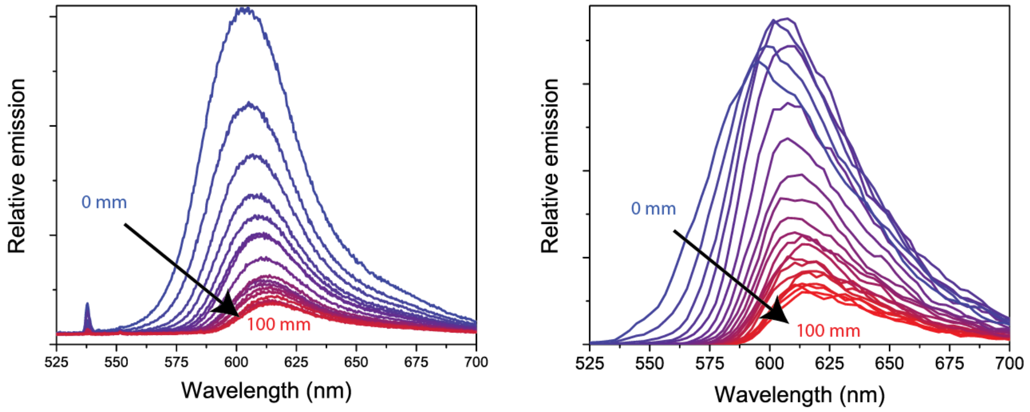

Figure 4-8: Spectral edge emission changes with excitation depth. (a) (c) and (e) spectral changes in LSC edge emission with excitation distance for all LSC devices. The peak at 532 nm is an artefact from the excitation spot. (b) (d) and (f) simulated spectral change in edge emission with excitation distance for all LSC devices. Data represent histograms collected from 10^6 incident photons.

4.4.6 **Spectrally-resolved external quantum efficiency**

Spectrally-resolved EQE of the three LSCs was measured by affixing a small high-efficiency silicon PV cell to one edge of the LSC, and scanning the wavelength of a small monochromatic excitation spot held stationary near the attached cell. It is worth noting that the magnitude of the EQE is determined by the position of both the excitation spot and the PV cell. Simulations were conducted by constraining the excitation position and wavelength to match the experimental conditions. The measured and simulated EQEs are shown in Figure 4-9. The measurements are well-matched by the simulated results, when we allow for a non-zero baseline due to excitation source scatter and imperfect LSC-PV cell coupling.

The EQE in the ultraviolet increases as the oligofluorene length increases, although the increase is not linear with fluorene count since the absorbed fraction scales logarithmically with optical density. The red-shifting of the oligofluorene feature accords with the measured absorption spectra. As expected, the EQE of the BODIPY feature is essentially constant across the three devices, with small differences ascribed to the PLQE and emission blue-shift differences of the three.

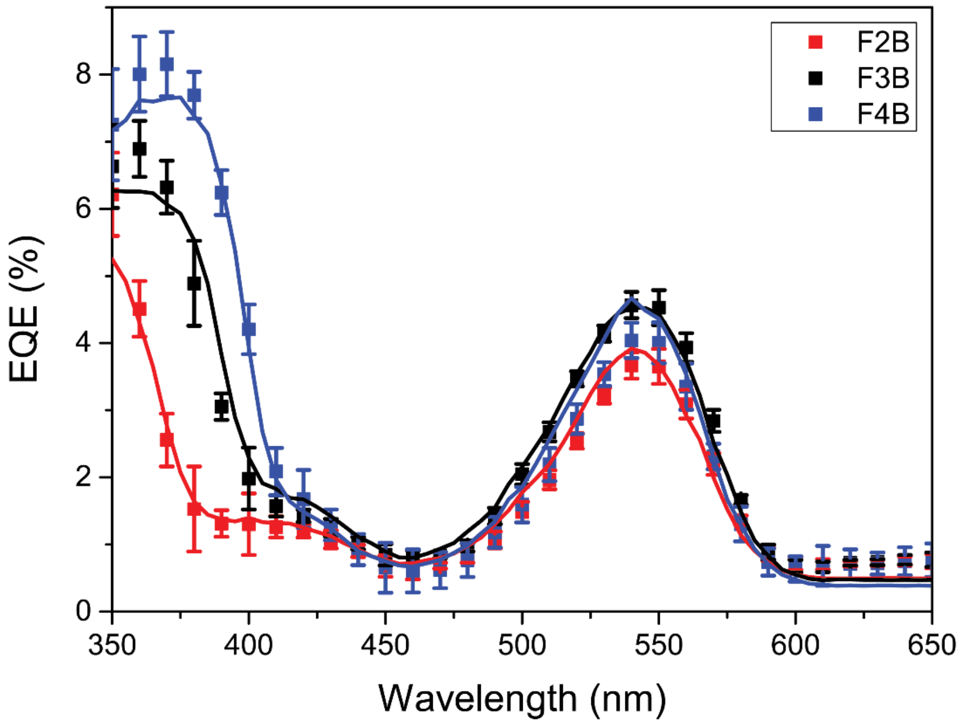

Figure 4-9: Spectrally-resolved external quantum efficiency of the fabricated LSC-PV system (squares) and simulated data (lines). Error bars represent the deviation in multiple EQE measurements.

4.4.7 Study of optimized devices using raytracing

As the simulation results accord with our experiments, we turn to simulations to predict the performance of optimized LSCs based on the three OFBMs studied. First, we repeated the EQE simulations presented in Table 4, maintaining the device geometry and PV cell characteristics, but stepping through dye concentration to find the optimum performance. Results are shown in Figure 4-10 (a). A maximum EQE of 5.6% was found for F3B, roughly doubling the measured value, at a concentration of 0.25 mM. F2B and F4B both reached maximum EQEs of about 4.2% at similar concentrations. We note that the additional fluorene chromophores on F4B do not outweigh the penalties of increased emission blue-shift and decreased PLQE, and the EQE is on par with that of F2B for the device geometry studied.

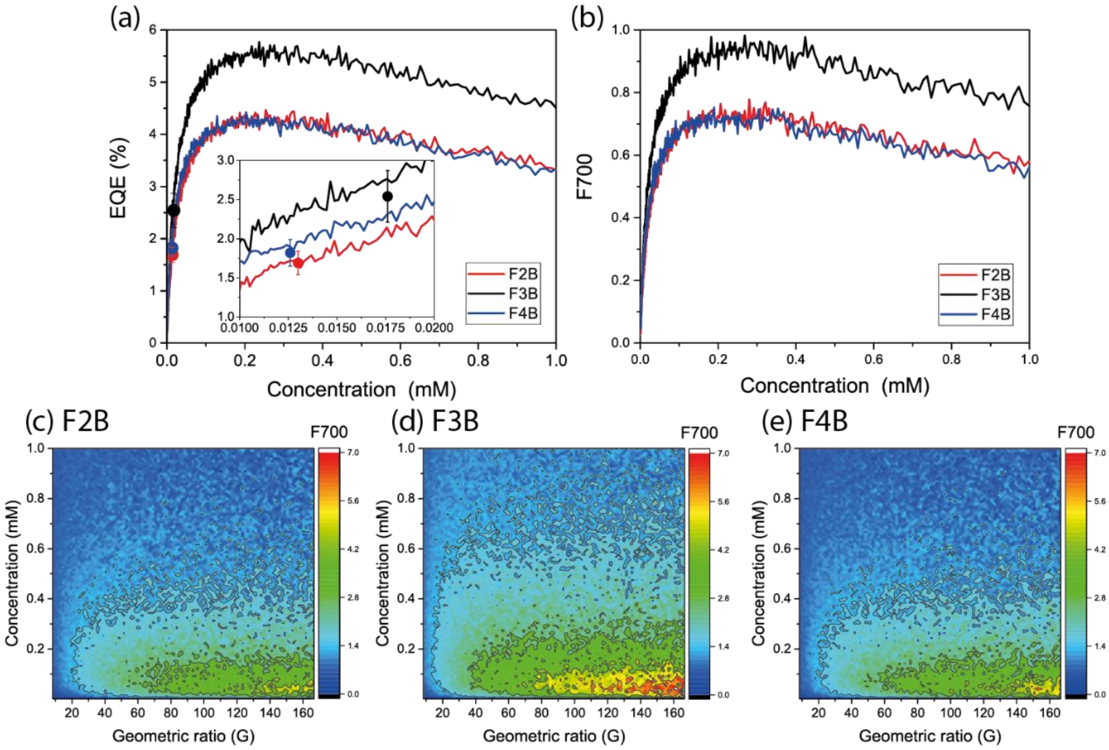

Figure 4-10: Results of Monte Carlo ray trancing simulations of the three OFMBs studied. (a) EQEs using the same geometry and PV cell detectors utilized in actual measurements, as a function of dye concentration. Insert shows the low concentration region. Colored circles represent our measurements of the fabricated LSCs. (b) Flux gain at 700nm as a function of concentration, for the same LSCs. Flux gain at 700 nm with changing concentration and geometric ratio for (c) F2B, (d) F3B and (e) F4B.

Calculated F700 results are shown in Figure 4-10 (b). Much like the EQE results, F3B is the superior material, with flux gain approaching 1.0, while F2B and F4B show similar trends with concentration, peaking at 0.6. In our final simulation of these devices, we show that appreciable flux gains are possible: conducting a two-dimensional parameter sweep of geometric ratio and concentration (Figure 4-10 (c)-(e)), we find that the simulated flux gain of F3B exceeds 1.0 for a G of 9.9 (G of 14.7 for F2B and F4B), and plateaus at F = 7.1 at a G of 128 (F = 4.9 at a G of 138 for F2B and F4B). These flux gains are comparable to LSCs based on CdSe/CdS, $Cd_{0.999}Cu_{0.001}Se$ and Mn^{2+}-doped ZnSe/Zn core-shell quantum dots[13,63]. Large improvements to flux gain are anticipated if the absorption gap between the fluorene donor and the BODIPY core can be filled, which we approach in the next section.

4.4.8 Simulations of extended dye structures

The potential applications of the LSCs studied above are inherently limited by solar flux in the UV region, low absorption coefficients in the visible region of the spectrum and an emission which is too high in energy. It is known that chromophores made from BODIPY cores and extended chromophore π-systems are highly versatile[65–67] and can be conveniently tailored to span the entire visible spectrum[68–70]. We present hypothetical structures that overcome these shortcomings by generating plausible absorption and emission spectra and testing their behavior in simulated LSCs. The BODIPY-fluorene systems presented in this study are synthesized without linker sections between the separate chromophores, allowing efficient energy transfer into the BODIPY core. We thus expect that this donor-acceptor scheme can be extended to larger structures with improved spectral coverage without significantly impairing energy transfer to the central emitter. Three hypothetical structures were studied: an OFBM containing 8 fluorenes per arm (F8B) (Figure 4-11 (a)); an OFBM with a new chromophore of intermediate energy inserted between the fluorene and the BODIPY (F8GB) (Figure 4-11 (c)); and two F8GB molecules connecting to a central deep-red emitter molecule (2(F8GB)D) (Figure 4-11 (e)). The hypothesized extinction and fluorescence spectra of these structures are shown in Figure 4-11 (b), (d) and (f). The PLQE of the hypothetical molecules was set to 0.8, and all emission was assumed to occur from the core. Additional details on the likely reaction schemes that yield these structures are given in Figure 4-12. We simulated EQE for each LSC using the same device geometry as the measured systems, and then simulated flux gain as a function of dye concentration and geometric ratio.

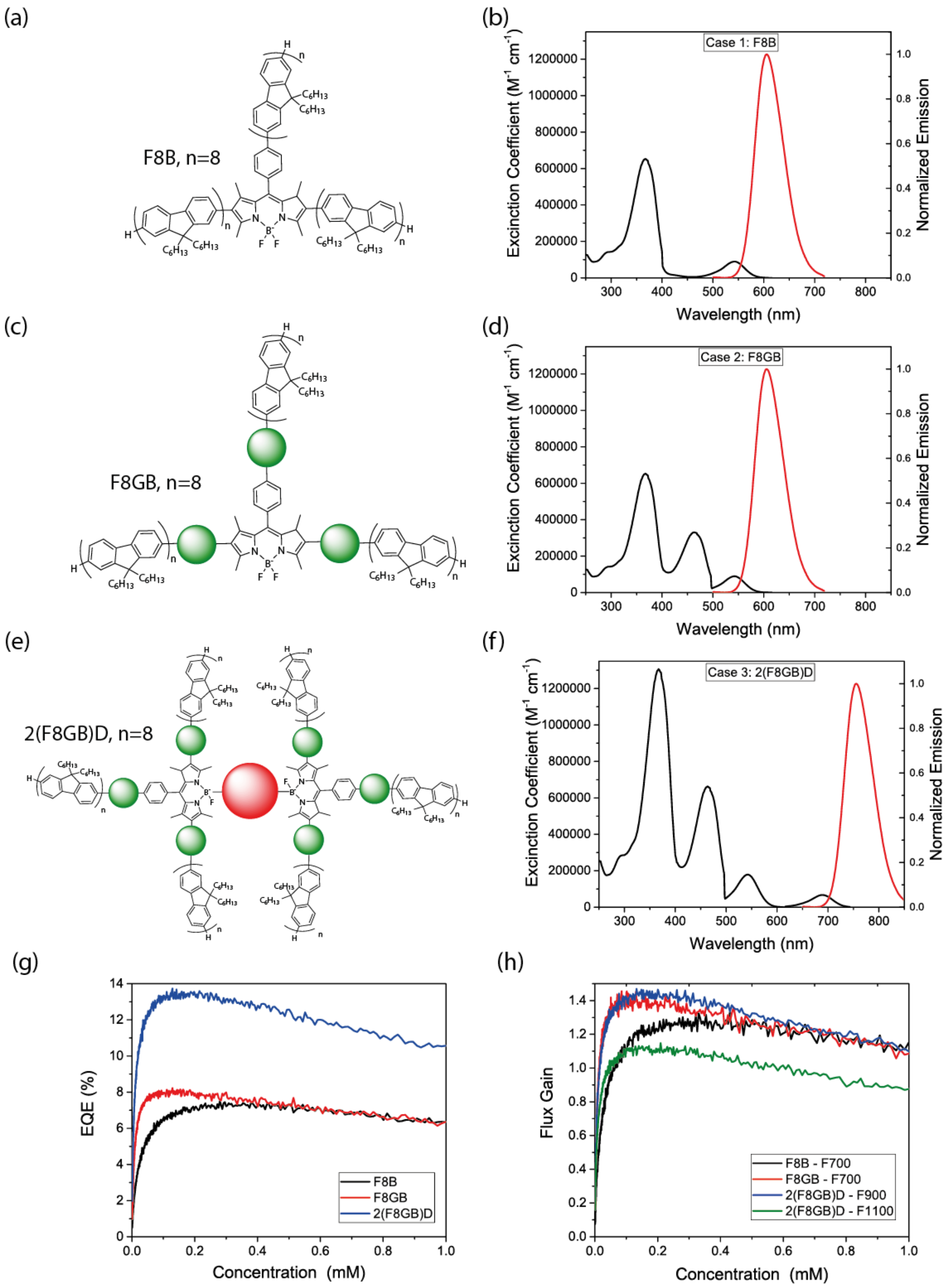

Figure 4-11. Molecular structures, steady-state optical spectra and results of Monte Carlo ray trancing simulations of the hypothetical OFBMs. a), c) and e) Molecular structure of F8B, F8GB and 2(F8GB)D, respectively. B), D) F), Extinction and fluorescence spectra of the respective materials. (g) EQE simulations for 10 x 10cm devices, (h) flux gain simulations for the same LSC geometry.

Simulated peak EQEs increased through the F8B, F8GB and 2(F8GB)D LSCs, and broadly followed the same trend with dye concentration (Figure 4-11 (g)). If these hypothetical molecules were used in our experimental set up they would produce peak EQEs of 7.2%, 8.0% and 13.4% respectively, which is a considerable gain over the molecules studied. This is due to the improved absorption of incident sunlight by the extended dye structures. Flux gains under specific thresholds for the 10 cm side-length devices (Figure 4-12 (h)) exceeded unity for all three materials, peaking at 1.30 and 1.43 for F8B and F8GB respectively at 700 nm, with concentration optimized. Considering that 2(F8GB)D has a redder emission than the other OFBMs studied, flux gains were calculated at 900 nm and 1100nm thresholds. Peak flux gains were found to be 1.45 and 1.13 respectively.

Two-dimensional flux gain simulations (Figure 4-13) showed that F8B and F8GB reach F700 values of ≈ 10 and 16 at G = 160, while 2(F8GB)D has peak F900 and F1100 values of ≈ 15 and 12 respectively. While simulated flux gain continues to increase as we simulate yet-larger LSCs, in reality absorption in the matrix (an effect not included in the model) may start to dominate. For comparison, at G=160 recently synthesized CuInS2/CdS core-shell quantum dots, which are reportedly the best-performing nanocrystalline emitters to date[63], show a projected flux gain of ~21 at the crystalline silicon bandgap, while those of $Cd_{0.999}Cu_{0.001}Se$ and CdSe/CdS core-shell dots are projected to be ~7 and ~5, respectively[63]. These findings demonstrate that the potential of OFBMs and their analogues to achieve effective light concentration in LSCs is on a par with contemporary nanocrystalline materials. This warrants the synthesis and characterization of these larger donor-acceptor structures. With the addition of redder-emitting chromophores, OFBMs may even function effectively with silicon PV cells, assuming a moderately high PLQE can be maintained.

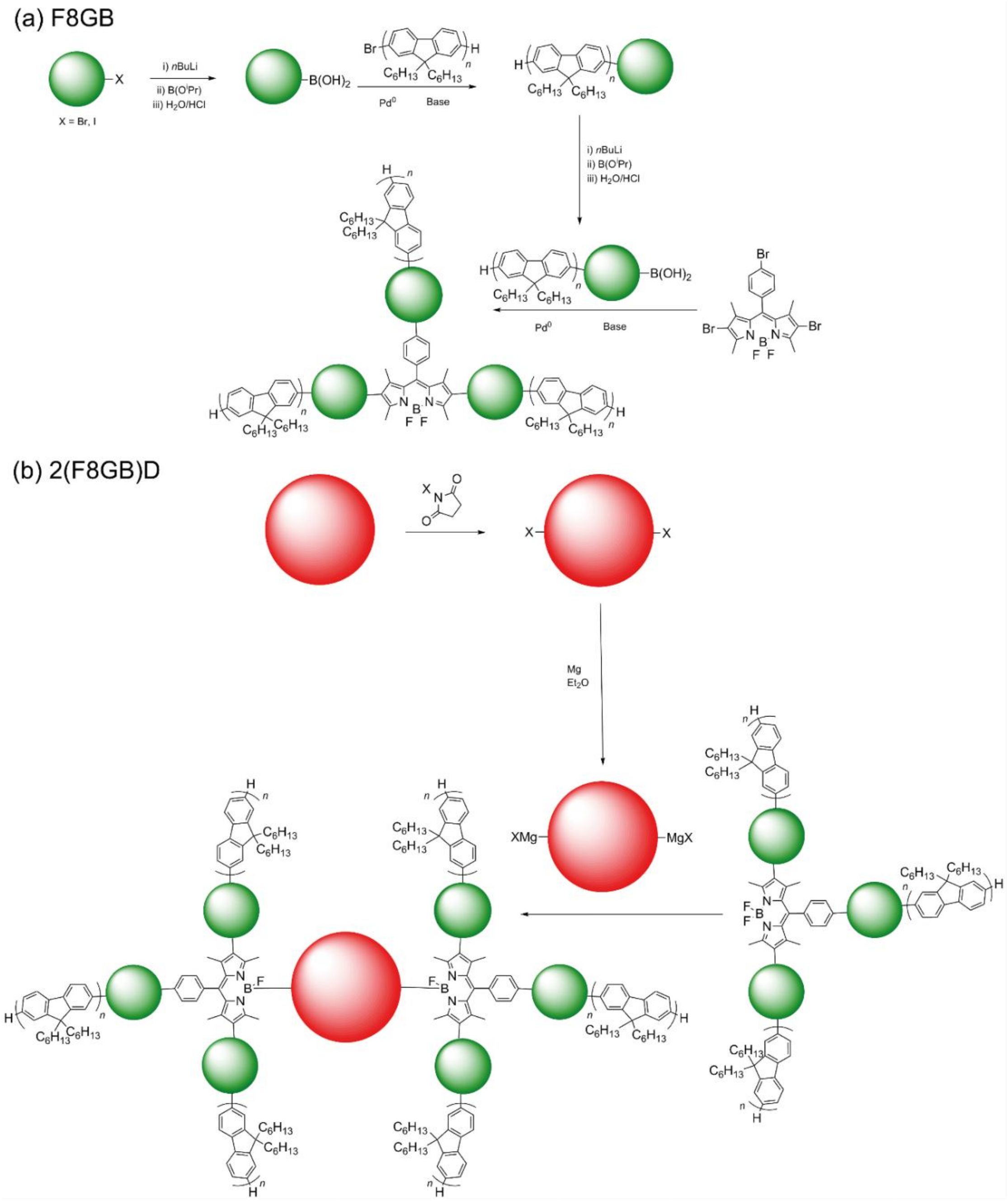

Figure 4-12: Proposed synthetic scheme for (a) F8GB and (b) 2(F8GB)D. Examples of units with chromophores suitable for use in place of the spherical placeholders include: dithienylbenzothiadiazole units with peripheral carbazole moieties[71] or star shaped diketopyrrolopyrrole centered oligofluorenes[72] (red sphere) and 2,1,3-benzothiadiazole units[73] (green spheres)

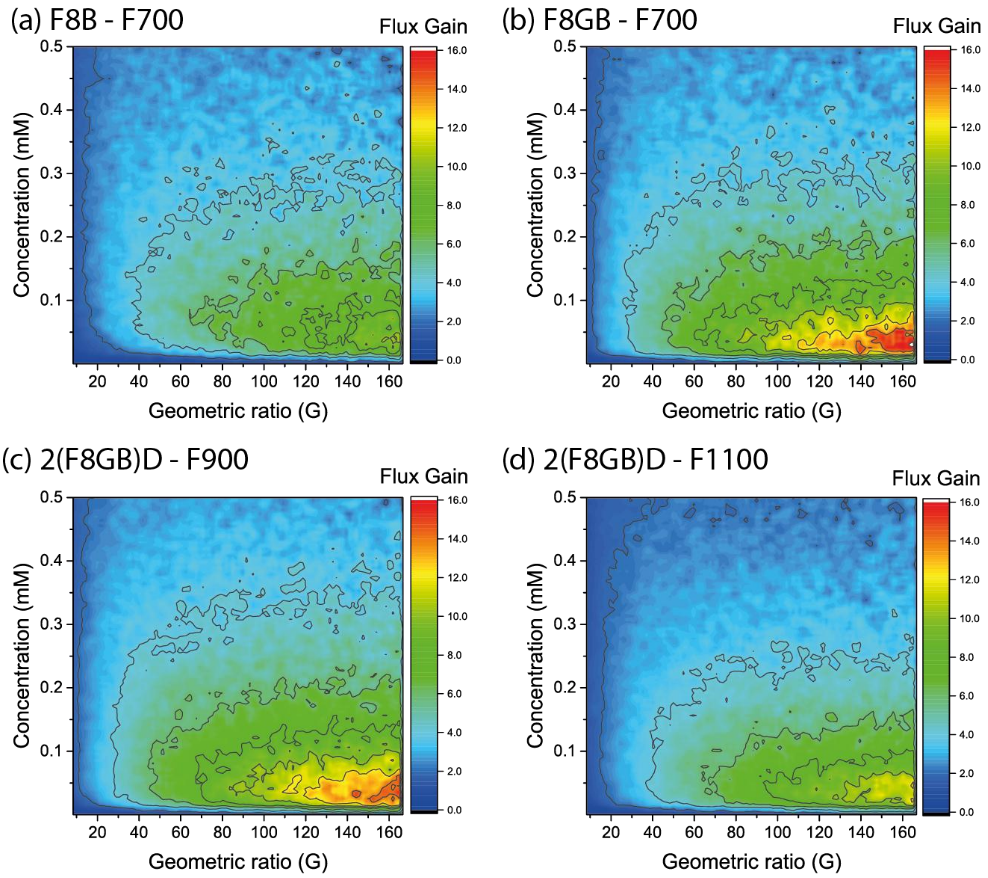

Figure 4-13: Results of Monte Carlo ray tracing simulations on hypothetical OFBM molecules, with PLQEs of 0.80. Flux gain with changing concentration and devices size for (a) F8B, (b) F8GB and ((c) and (d)) 2(F8GB)D.

4.5 Conclusions

Oligofluorene-BODIPY donor-acceptor molecules represent attractive candidates for luminescent solar concentrators due to their synthetic versatility, high absorption coefficients, high PLQEs and efficient energy transfer to the BODIPY core. LSCs containing three different OFBMs were fabricated and characterized using a variety of optical measurements. A Monte Carlo raytracing simulation was used to successfully replicate these results. We subsequently used this simulation to study optimized LSCs based on the three starting compounds, along with three hypothetical OFBM structures which extended the donor-acceptor functionality in a plausible fashion. We found that in optimized conditions, the proposed OFBM molecules perform on-par with leading nanocrystalline emitters, warranting further investigation into the synthesis of these extended antennae complexes and their incorporation into LSCs.

4.6 On Going Research

The oligofluorenes used represented a model system to study synthetic antenna complexes, however they are not ideal for PV application. This is due to their main absorbance and emission features being too high in energy for most solar cells. Ideally the proposed molecules presented in this chapter could be synthesized and used in LSCS. By including a new chromophore that absorbs in the blue-green region absorbance over the solar spectrum could be increased. If it were possible to maintain the energy transfer from the fluorene arm units through a variety of lower energy chromophores into the central chromophore, which should be significantly red shifted, these molecules would be some of the best materials for LSCs.

Peter Skabara's group at The University of Strathclyde has synthesized other types of oligofluorenes which may be more suitable for LSC application[33]. While the T-series was used in the report, the Y series (Figure 4-14 a)) has a broader absorption spectrum and has an emission further to the red (Figure 4-14 b)), although the PLQEs of the Y-series are lower than those of the T-series (Figure 4-15)[33].

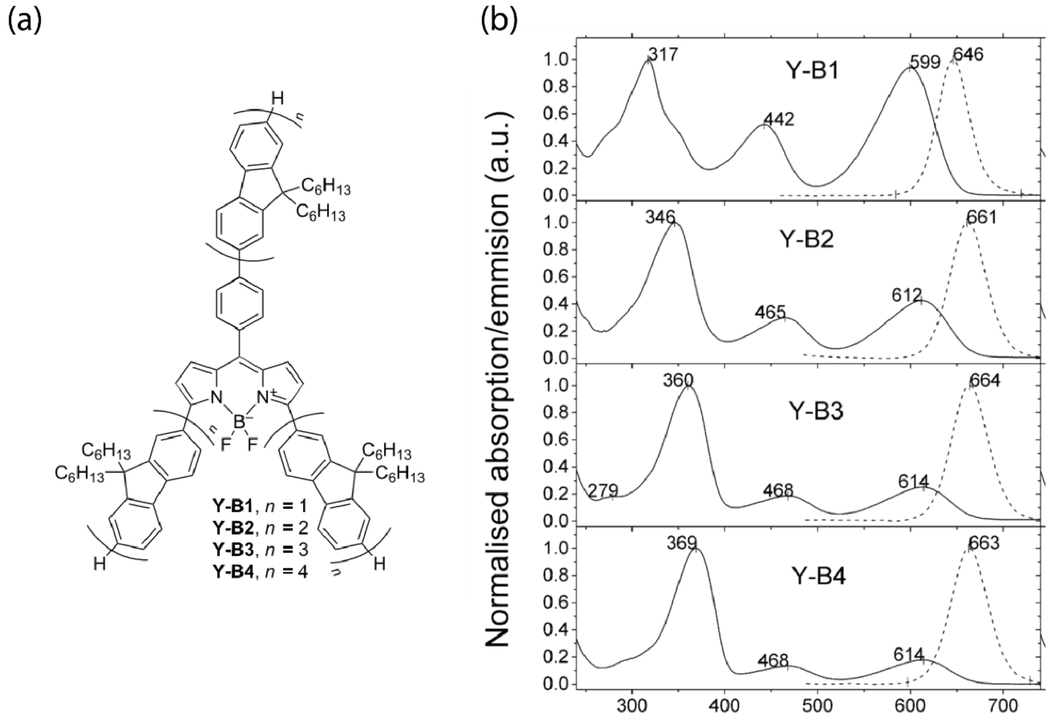

Figure 4-14: Y-series oligofluorenes. a) The structure of the Y-series star-shaped oligofluorenes with BODIPY cores. b) The normalized absorption (solid lines) and emission (dash lines) spectra of Y-Bn (n = 1–4)[33].

Briefly, LSC devices (10 × 10 × 0.3 cm) were simulated using these molecules at various concentrations (Figure 4-15). A maximum EQE of 4.0% was found for Y3-B, at a concentration of 0.07 mM and Y1-B reached 2.7% at similar concentrations. We find the additional fluorene chromophores in Y4-B do not outweigh the penalties of decreased PLQE, and the EQE is on par with that of F2B, being 3.5%, for the device geometry studied. Although these molecules were predicted to lead to improved LSC performances, the decreased PLQE, which is a fundamental parameter of an LSC, inhibits this. As PLQE is dependent on molecular structure, this result further emphasizes the need for specific control over the bonding arrangement in chromophores used in antenna complexes. Further synthetic analysis could be done to systematically study the effect of different bonding positions around the BODIPY core. This analysis could further be extended to look at the effect of different linking groups between the fluorene units in the arms and the fluorene BODIPY linkage. The emphasis should focus on isolating the relative chromophores while ensuring efficient energy transfer to the central core.

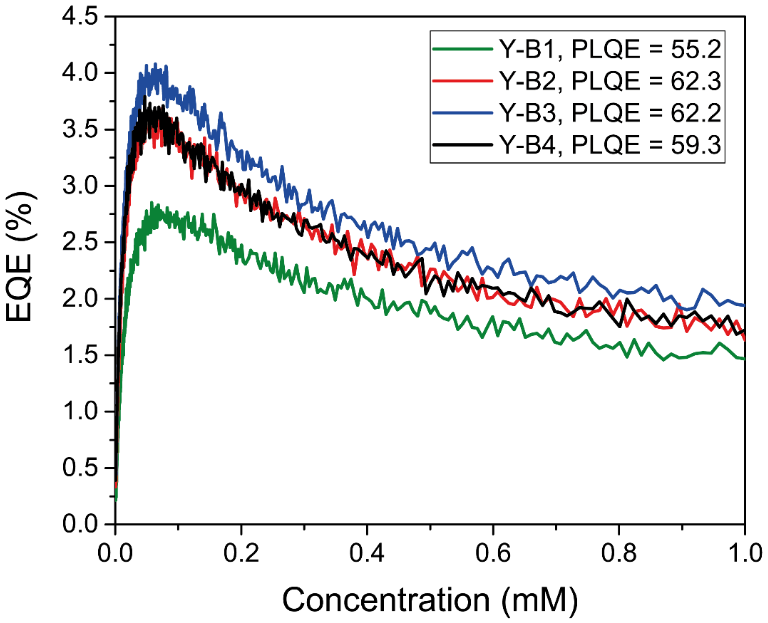

Figure 4-15: Monte Carlo ray trancing simulations of Y-series oligofluorenes. EQEs were calculated using the same geometry utilized in results section (10 × 10 × 0.3 cm).

This chapter looked at the use of oligofluorenes in LSCs. Since improvements were shown by increasing the number of fluorine units in the arms, it is worth exploring the ideal number of units required for minimal reabsorption. Considering a 0.3 × 100 × 100 cm device. We set the absorbance through the thin plane of the LSC at 375nm, corresponding to peak fluorine absorption, to 2 as such 99% of the incident light (at 375 nm) is absorbed. As we calculated an extinction coefficient of ≈ 30,000 M^{-1} cm^{-1} per fluorene unit and 80,000 M^{-1} cm^{-1} in the BODIPY region we can work out the required concentrations for our devices to have an absorbance of 2. Now we can calculate the transmission of light with a pathlength of 1 m along the plane of the LSC at different wavelengths corresponding to peak BODIPY absorption, peak BODIPY emission and peak absorption and emission overlap. This allows us explore the number of fluorene units required to give close to 100% transmittance or emitted light (Figure 4-16).

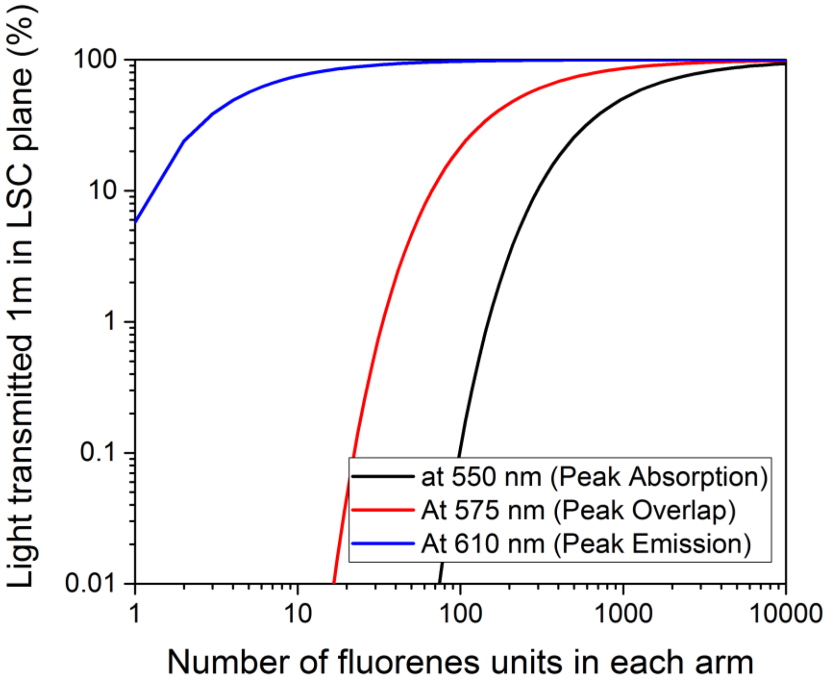

Figure 4-16: Ideal olgiofluorene molecules for minimal reabsorption in a 0.3 × 100 × 100 cm device.

From Figure 4-16 we find that in the worst case scenario, just considering the peak absorption of the BODIPY region, we require 10,000 fluorene units to reach ≈ 100% transmission i.e. a F10,000B. When comparing the absorption and emission overlap of the BODIPY center we require a F1,000B. Finally, when we consider just peak emission the values approach something more synthetically reasonable of less than 100 fluorene units per arm. It is worth nothing that the above calculation represent pessimistic values as rarely in 1 × 1 m devices would a photon have to travel 1 m reach the output edge. Thus in reality minimizing reabsorption should be able to be achieved with more reasonable values then presented above.

4.7 References

(1) Debije, M. G.; Verbunt, P. P. C. *Adv. Energy Mater.* **2012**, *2*, 12–35.

(2) Batchelder, J. S.; Zewail, A. H.; Cole, T. *Appl. Opt.* **1979**, *18*, 3090–3110.

(3) van Sark, W. G. J. H. M. *Renew. Energ.* **2012**, 1–4.

(4) van Sark, W. G. J. H. M.; Barnham, K. W. J.; Slooff, L. H.; Chatten, A. J.; Buechtemann, A.; Meyer, A.; McCormack, S. J.; Koole, R.; Farrell, D. J.; Bose, R.; Bende, E. E.; Burgers, A. R.; Budel, T.; Quilitz, J.; Kennedy, M.; Meyer, T.; De, M. D. C.; Meijerink, A.; Vanmaekelbergh, D. *Opt. Express* **2008**, *16*, 21773–21792.

(5) Delavari Amrei, H.; Ranjbar, R.; Rastegar, S.; Nasernejad, B.; Nejadebrahim, A. *J. Appl. Phycol.* **2014**, 67–74.

(6) Earp, A. A.; Smith, G. B.; Franklin, J.; Swift, P. *Sol. Energy Mater. Sol. Cells* **2004**, *84*, 411–426.

(7) Manousiadis, P. P.; Rajbhandari, S.; Mulyawan, R.; Vithanage, D. A.; Chun, H.; Faulkner, G.; O'Brien, D. C.; Turnbull, G. A.; Collins, S.; Samuel, I. D. W. *Optica* **2016**, *3*, 702–706.

(8) Giebink, N. C.; Wiederrecht, G. P.; Wasielewski, M. R. *Nat. Photonics* **2011**, *5*, 694–701.

(9) Farrell, D.; Yoshida, M. *Prog. Photovoltaics Res. Appl.* **2012**, *20*, 93–99.

(10) Roncali, J.; Garnier, F. *Appl. Opt.* **1984**, *23*, 2809–2817.

(11) Olson, R. W.; Loring, R. F.; Fayer, M. D. *Appl. Opt.* **1981**, *20*, 2934–2940.

(12) Wilson, L. R.; Rowan, B. C.; Robertson, N.; Moudam, O.; Jones, A. C.; Richards, B. S. *Appl. Opt.* **2010**, *49*, 1651–1661.

(13) Erickson, C.; Bradshaw, L. *ACS Nano* **2014**, 3461–3467.

(14) Wilson, L. R.; Richards, B. S. *Appl. Opt.* **2009**, *48*, 212–220.

(15) Bailey, S. T.; Lokey, G. E.; Hanes, M. S.; Shearer, J. D. M.; McLafferty, J. B.; Beaumont, G. T.; Baseler, T. T.; Layhue, J. M.; Broussard, D. R.; Zhang, Y.-Z.; Wittmershaus, B. P. *Sol. Energy Mater. Sol. Cells* **2007**, *91*, 67–75.

(16) Mulder, C. L.; Theogarajan, L.; Currie, M.; Mapel, J. K.; Baldo, M. A.; Vaughn, M.; Willard, P.; Bruce, B. D.; Moss, M. W.; McLain, C. E.; Morseman, J. P. *Adv. Mater.* **2009**, *21*, 3181–3185.

(17) Davis, N. J. L. K.; MacQueen, R. W.; Roberts, D. A.; Danos, A.; Dehn, S.; Perrier,

S.; Schmidt, T. W. *J. Mater. Chem. C* **2016**, *4*, 8270–8275.

(18) Meinardi, F.; McDaniel, H.; Carulli, F.; Colombo, A.; Velizhanin, K. A.; Makarov, N. S.; Simonutti, R.; Klimov, V. I.; Brovelli, S. *Nat. Nanotechnol.* **2015**, *10*, 878–885.

(19) Meinardi, F.; Colombo, A.; Velizhanin, K. A.; Simonutti, R.; Lorenzon, M.; Beverina, L.; Viswanatha, R.; Klimov, V. I.; Brovelli, S. *Nat. Photonics* **2014**, *8*, 392–399.

(20) Balaban, B.; Doshay, S.; Osborn, M.; Rodriguez, Y.; Carter, S. A. *J. Lumin.* **2014**, *146*, 256–262.

(21) Tummeltshammer, C.; Taylor, A.; Kenyon, A. J.; Papakonstantinou, I. *J. Appl. Phys.* **2014**, *116*.

(22) Banal, J. L.; Ghiggino, K. P.; Wong, W. W. H. *Phys. Chem. Chem. Phys.* **2014**, *16*, 25358–25363.

(23) Banal, J. L.; Soleimaninejad, H.; Jradi, F. M.; Liu, M.; White, J. M.; Blakers, A. W.; Cooper, M. W.; Jones, D. J.; Ghiggino, K. P.; Marder, S. R.; Smith, T. A.; Wong, W. W. H. *J. Phys. Chem. C* **2016**, *120*, 12952–12958.

(24) Kaniyoor, A.; Mckenna, B.; Comby, S.; Evans, R. C. *Adv. Opt. Mater.* **2016**, *4*, 444–456.

(25) Förster, T. *Discuss. Faraday Soc.* **1959**, *27*, 7–17.

(26) Roberts, D. V; Wittmershaus, B. P.; Zhang, Y.-Z.; Swan, S.; Klinosky, M. P. *J. Lumin.* **1998**, *79*, 225–231.

(27) Fennel, F.; Lochbrunner, S. *Phys. Chem. Chem. Phys.* **2011**, *13*, 3527–3533.

(28) Calzaferri, G.; Meallet-Renault, R.; Bruhwiler, D.; Pansu, R.; Dolamic, I.; Dienel, T.; Adler, P.; Li, H.; Kunzmann, A. *Chem. Phys. Chem* **2011**, *12*, 580–594.

(29) Braslavsky, S. E.; Fron, E.; Rodríguez, H. B.; Román, E. S.; Scholes, G. D.; Schweitzer, G.; Valeur, B.; Wirz, J. *Photochem. Photobiol. Sci.* **2008**, *7*, 1444–1448.

(30) Bruehwiler, D.; Calzaferri, G.; Torres, T.; Ramm, J. H.; Gartmann, N.; Dieu, L.-Q.; Lopez-Duarte, I.; Martinez-Diaz, M. V. *J. Mater. Chem.* **2009**, *19*, 8040–8067.

(31) Eisfeld, A.; Briggs, J. S. *Chem. Phys.* **2006**, *324*, 376–384.

(32) Neuteboom, E. E.; Meskers, S. C. J.; Meijer, E. W.; Janssen, R. A. J. *Macromol. Chem. Phys.* **2004**, *205*, 217–222.

(33) Orofino-Pena, C.; Cortizo-Lacalle, D.; Cameron, J.; Sajjad, M. T.; Manousiadis, P. P.; Findlay, N. J.; Kanibolotsky, A. L.; Amarasinghe, D.; Skabara, P. J.; Tuttle, T.; Turnbull, G. A.; Samuel, I. D. W. *Beilstein J. Org. Chem.* **2014**, *10*, 2704–2714.

(34) MacColl, R. *J. Struct. Biol.* **1998**, *124*, 311–334.

(35) Loudet, A.; Burgess, K. *Chem. Rev.* **2007**, *107*, 4891–4932.

(36) Ziessel, R.; Ulrich, G.; Harriman, A. *New J. Chem.* **2007**, *31*, 496–501.

(37) Ulrich, G.; Ziessel, R.; Harriman, A. *Angew. Chemie - Int. Ed.* **2008**, *47*, 1184–1201.

(38) Benniston, A. C.; Copley, G. *Phys. Chem. Chem. Phys.* **2009**, *11*, 4124–4131.

(39) Courtis, A. M.; Santos, Sofia, A.; Guan, Y.; Hendricks, J. A.; Ghosh, B.; Szantai-kis, D. M.; Reis, S. A.; Shah, J. V; Mazitschek, R. *Bioconjug. Chem.* **2014**, *25*, 1043–1051.

(40) Moriarty, R. D.; Martin, A.; Adamson, K.; O'Reilly, E.; Mollard, P.; Forster, R. J.; Keyes, T. E. *J. Microsc.* **2014**, *253*, 204–218.

(41) Ni, Y.; Wu, J. *Org. Biomol. Chem.* **2014**, *12*, 3774–3791.

(42) Duran-Sampedro, G.; Agarrabeitia, A. R.; Garcia-Moreno, I.; Costela, A.; Banuelos, J.; Arbeloa, T.; Lopez Arbeloa, I.; Chiara, J. L.; Ortiz, M. J. *European J. Org. Chem.* **2012**, 6335–6350.

(43) Bañuelos, J.; Martín, V.; Gómez-Durán, C. F. A.; Córdoba, I. J. A.; Peña-Cabrera, E.; García-Moreno, I.; Costela, Á.; Pérez-Ojeda, M. E.; Arbeloa, T.; Arbeloa, Í. L. *Chem. - A Eur. J.* **2011**, *17*, 7261–7270.

(44) Ortiz, M. J.; Garcia-Moreno, I.; Agarrabeitia, A. R.; Duran-Sampedro, G.; Costela, A.; Sastre, R.; Lopez Arbeloa, F.; Banuelos Prieto, J.; Lopez Arbeloa, I. *Phys. Chem. Chem. Phys.* **2010**, *12*, 7804–7811.

(45) Cortizo-Lacalle, D.; Howells, C. T.; Gambino, S.; Vilela, F.; Vobecka, Z.; Findlay, N. J.; Inigo, A. R.; Thomson, S. A. J.; Skabara, P. J.; Samuel, I. D. W. *J. Mater. Chem.* **2012**, *22*, 14119.

(46) Popere, B. C.; Della Pelle, A. M.; Poe, A.; Balaji, G.; Thayumanavan, S. *Chem. Sci.* **2012**, *3*, 3093.

(47) Popere, B. C.; Della Pelle, A. M.; Thayumanavan, S. *Macromolecules* **2011**, *44*, 4767–4776.

(48) Altan Bozdemir, O.; Erbas-Cakmak, S.; Ekiz, O. O.; Dana, A.; Akkaya, E. U. *Angew. Chemie - Int. Ed.* **2011**, *50*, 10907–10912.

(49) Kanibolotsky, A. L.; Perepichka, I. F.; Skabara, P. J. *Chem. Soc. Rev.* **2010**, *39*, 2695–2728.

(50) Adronov, A.; Fréchet, J. M. J. *Chem. Commun.* **2000**, 1701–1710.

(51) Guliyev, R.; Coskun, A.; Akkaya, E. U. *J. Am. Chem. Soc.* **2009**, *131*, 9007–9013.

(52) Yilmaz, M. D.; Bozdemir, O. A.; Akkaya, E. U. *Org. Lett.* **2006**, *8*, 2871–2873.

(53) Chen, C. Y.; Yeh, K. L.; Aisyah, R.; Lee, D. J.; Chang, J. S. *Bioresour. Technol.* **2011**, *102*, 71–81.

(54) Mohsenpour, S. F.; Richards, B.; Willoughby, N. *Bioresour. Technol.* **2012**, *125*,

75–81.

(55) Johkan, M.; Shoji, K.; Goto, F.; Hahida, S.; Yoshihara, T. *Environ. Exp. Bot.* **2012**, *75*, 128–133.

(56) Mohsenpour, S. F.; Willoughby, N. *Bioresour. Technol.* **2013**, *142*, 147–153.

(57) MacQueen, R. W.; Tayebjee, M. J. Y.; Webb, J. E. A.; Falber, A.; Thordarson, P.; Schmidt, T. W. *J. Opt.* **2016**, *18*, 064010.

(58) Sajjad, M. T.; Manousiadis, P. P.; Orofino, C.; Cortizo-Lacalle, D.; Kanibolotsky, A. L.; Rajbhandari, S.; Amarasinghe, D.; Chun, H.; Faulkner, G.; O'Brien, D. C.; Skabara, P. J.; Turnbull, G. A.; Samuel, I. D. W. *Adv. Opt. Mater.* **2015**, *3*, 536–540.

(59) Bomm, J.; Büchtemann, A.; Chatten, A. J.; Bose, R.; Farrell, D. J.; Chan, N. L. A.; Xiao, Y.; Slooff, L. H.; Meyer, T.; Meyer, A.; van Sark, W. G. J. H. M.; Koole, R. *Sol. Energy Mater. Sol. Cells* **2011**, *95*, 2087–2094.

(60) Bomm, J.; Büchtemann, A.; Fiore, A.; Manna, L.; Nelson, J. H.; Hill, D.; van Sark, W. G. J. H. M. *Beilstein J. Nanotechnol.* **2010**, *1*, 94–100.

(61) Bronstein, N.; Li, L.; Xu, L.; Yao, Y. *ACS Nano* **2014**, *8*, 44–53.

(62) Yang, X.; Zhang, X. F.; Lu, X.; Yu, C.; Jiao, L. *J. Photochem. Photobiol. A Chem.* **2015**, *297*, 39–44.

(63) Knowles, K. E.; Kilburn, T. B.; Alzate, D. G.; McDowall, S.; Gamelin, D. R. *Chem. Commun.* **2015**, *51*, 9129–9132.

(64) Shcherbatyuk, G. V.; Inman, R. H.; Wang, C.; Winston, R.; Ghosh, S. *Appl. Phys. Lett.* **2010**, *96*, 191901.

(65) Li, L.; Han, J.; Nguyen, B.; Burgess, K.; Li, L.; Han, J.; Nguyen, B.; Burgess, K. *J. Org. Chem.* **2008**, *73*, 1963–1970.

(66) Ozdemir, T.; Atilgan, S.; Kutuk, I.; Yildirim, L. T.; Tulek, A.; Bayindir, M.; Akkaya, E. U. *Org. Lett.* **2009**, *11*, 2105–2107.

(67) Erbas, S.; Gorgulu, A.; Kocakusakogullari, M.; Akkaya, E. U. *Chem. Commun.* **2009**, 4956–4958.

(68) Wang, D.; Fan, J.; Gao, X.; Wang, B.; Sun, S.; Peng, X. *J. Org. Chem.* **2009**, *74*, 7675–7683.

(69) Rurack, K.; Kollmannsberger, M.; Daub, J. *Angew. Chemie - Int. Ed.* **2001**, *40*, 385–387.

(70) Umezawa, K.; Nakamura, Y.; Makino, H.; Citterio, D.; Suzuki, K. *J. Am. Chem. Soc.* **2008**, *130*, 1550–1551.

(71) Wang, Z.; Lu, P.; Xue, S.; Gu, C.; Lv, Y.; Zhu, Q.; Wang, H.; Ma, Y. *Dye. Pigment.* **2011**, *91*, 356–363.

(72) Kanibolotsky, A. L.; Vilela, F.; Forgie, J. C.; Elmasly, S. E. T.; Skabara, P. J.;

Zhang, K.; Tieke, B.; McGurk, J.; Belton, C. R.; Stavrinou, P. N.; Bradley, D. D. C. *Adv. Mater.* **2011**, *23*, 2093–2097.

(73) Belton, C. R.; Kanibolotsky, A. L.; Kirkpatrick, J.; Orofi, C.; Elmasly, S. E. T.; Stavrinou, P. N.; Skabara, P. J.; Bradley, D. D. C. *Adv. Funct. Mater.* **2013**, *23*, 2792–2804.

5 PHOTON REABSORPTION IN LIGHT-EMITTING DIODES

5.1 Abstract

Cesium lead halide nanocrystals, $CsPbX_3$ (X = Cl, Br, I), exhibit photoluminescence quantum efficiencies approaching 100% without the core-shell structures usually used in conventional semiconductor nanocrystals. These high photoluminescence efficiencies make these crystals ideal candidates for light-emitting diodes (LEDs). However, due to the large surface area to volume ratio, halogen exchange between perovskite nanocrystals of different compositions occurs rapidly, which is one of the limiting factors for white-light applications requiring a mixture of different crystal compositions to achieve a broad emission spectrum. Here, we report significantly reduced halide exchange between chloride and iodide $CsPbX_3$ (X= Cl, I) perovskite nanocrystals. We investigate samples containing mixtures of perovskite nanocrystals with different compositions, and study the resulting optical and electrical interactions. We report excitation transfer from $CsPbCl_3$ to $CsPbI_3$ in solution and within a polymethylmethacrylate (PMMA) matrix via photon reabsorption, which also occurs in electrically excited crystals in bulk heterojunction LEDs.

This work was published in the Journal of Physical Chemistry C: Photon Reabsorption in $CsPbCl_3$ and $CsPbI_3$ Perovskite Nanocrystal Polymer Films and Light-Emitting Diodes. Authors: Davis, N. J. L. K.**;** de la Peña Manchon, F.; Tabachnyk, M.; Richter, J.; Lamboll, R. D.; Booker, E. P.; Wisnivesky-Rocca-

Rivarola, F.; Griffiths, J. T.; Ducati, C.; Menke, S. M.; Deschler, F.; and Greenham, N. C. DOI: 10.1021/acs.jpcc.6b12828.

All the below work was carried out by myself except where stated. Mr. Maxim Tabachnyk and Mr. Johannes M. Richter performed the transient photo-measurements. Mr. Edward P. Booker performed the XRD measurements. Dr S. Matthew Menke performed the PLQE measurements. Dr Francisco J. de la Peña performed the TEM measurements. Mr. Robin D. Lamboll carried out the Monte Carlo simulation.

5.2 Introduction

Low-cost solution-processable metal halide perovskite semiconductors[1–4] have seen encouraging development as inexpensive absorber layers in solar cells, and show high mobility[5–7], bright emission[8], tunable [9–11] and photon recycling[12]. Power conversion efficiencies for perovskite solar cells have exceeded 20%[13–16]. While the majority of research has focused on thin-film and bulk materials[4,13–15,17,18], perovskite nanocrystals have recently been synthesized. These include hybrid organic-inorganic $MAPbX_3$ (MA = methylammonium, X = Cl, Br, I) nanocrystals and nanostructures[19] as well as all-inorganic cesium lead halide $CsPbX_3$ (X = Cl, Br, I) and cesium tin halide $CsSnX_3$ (X = Cl, Br, I) nanocrystals and nanostructures[20–22]. The move to colloidal semiconductor quantum dots not only improves solution processability of these materials but also allows tunabilty due to 3D confinement effects[19,21], and creates a material that is readily miscible with other optoelectronic materials e.g. polymers, fullerenes and other nanomaterials. Hybrid organic-inorganic lead halide perovskite nanostructures have been used in detectors for the visible, ultraviolet and X-ray regions of the electromagnetic spectrum[23–27], as gain media for optically pumped lasers[10,28–32], and as emission layers for light-emitting diodes (LEDs)[8,33–35].

It has been reported that in perovskites ABX_3 (A = MA, Cs; B = Pb, Sn; X= Cl, Br, I) the ratios of the different halide components have a strong influence on the electronic properties of the material [36,37]. The ability of the halide ions to migrate within bulk perovskite has been reported both for $MAPbX_3$[38,39] and for $CsPbX_3$[40,41], which has specifically been identified as a halide-ion conductor[42]. The high ion mobility within perovskite crystals has been recognized as a possible source for the hysteresis in the current–voltage curves seen in photovoltaic devices[35,43]. In $CsPbX_3$ nanocrystals, which have a high surface area to volume ratio, halide exchange quickly incorporates new sources of excess halides, resulting in a shift of the optical. This is also the case when crystals with different halide compositions are mixed, resulting in the formation of crystals with an averaged total halide composition[40,41]. Halide exchange has been shown to be possible in both $MAPbX_3$ and $CsPbX_3$ when moving between periodically adjacent halides. e.g. from $CsPbCl_3$ to $CsPbBr_3$ and $CsPbBr_3$ to $CsPbI_3$ and vice versa[40,41].

Although recently there has been an increase in the application of $CsPbX_3$ nanocrystals[28,44–51] the inability of $CsPbX_3$ nanocrystals with different compositions to coexist as discrete semiconductors in one sample without rapid halide exchange significantly limits their use in applications where multiple bandgaps are required, such as white-light LEDs and exciton concentration systems. Recently Palazon et al.[52] showed that crosslinking the surface ligands in neat nanocrystal films improves stability, prevents film lift-off and limits halogen exchange. It has also been shown that wrapping clusters of $CsPbX_3$ nanocrystals in polyhedral oligomeric silsesquioxane cages can prevent halogen exchange[53]. However, neither of these methods allows the formation of films where the nanocrystals are mixed on the sub-micron scale.

Energy transfer from high-bandgap to low-bandgap nanocrystals has been demonstrated between $CsPbBr_3$ particles of different sizes[54]. Interactions between $CsPbCl_3$ and $CsPbI_3$ nanocrystals have previously been reported to lead to dissolution of the nanocrystals[55]. We find that when the crystals are synthesized and kept in an oxygen- and water-free environment this is not the case. We report significantly reduced halide exchange between chloride and iodide in $CsPbX_3$ (X= Cl, I) perovskite nanocrystals, due to the unfavorable crystal lattice tolerance factor for iodide-chloride exchange in this system. This allows us to investigate films and solutions containing nanocrystals of differing compositions, and to study the resulting optical and electronic interactions. Efficient excitation transfer from $CsPbCl_3$ to $CsPbI_3$ is found to proceed by a radiative process. Excitation transfer also occurs in electrically pumped crystals forming the active layer of a bulk heterojunction LED. $CsPbCl_3$ emission can efficiently be reabsorbed by the $CsPbI_3$ nanocrystals and reemitted in the red region.

5.3 Methods

All chemicals were purchased from Sigma-Aldrich, and were used as received.

Synthesis of CsPbX3 (X = Cl, I) Nanocrystals: Perovskite nanocrystals were synthesized using previously reported procedures[21]. Cs_2CO_3 (0.814g, 99.9%) was loaded into 100 mL three-neck flask along with octadecene (ODE, 30 mL, 90%) and oleic acid (2.5 mL, OA, 90%), the mixture was dried for 2 h at 120°C under N_2. The solution temperature was then lowered to 100°C. ODE (75 mL), oleylamine (7.5 mL, OLA, 90%), and dried OA (7.5 mL) and PbX_2 (2.82 mmol) such as PbI_2 (1.26 g, 99.99%), $PbCl_2$ (0.675g, 99.99%), were loaded into a 250 mL three-neck flask and dried under vacuum for 2 h at 120°C. After complete solubilization of the PbX_2 salt, the temperature was raised to 170°C and the Cs-oleate solution (6.0 mL, 0.125 M in ODE, prepared as described above) was quickly injected. After 10 s, the reaction mixture was cooled in an ice-water bath. For $CsPbCl_3$ synthesis, 5 mL of trioctylphosphine (TOP, 97%) was added to solubilize $PbCl_2$. The nanocrystals were transferred to an argon gloved box (H_2O and $O_2 < 1$ ppm) precipitated from solution by the addition of equal volume anhydrous butanol (BuOH, 99%) (ODE:BuOH = 1:1 by volume). After centrifugation, the supernatant was discarded and the nanocrystals were redispersed in anhydrous hexane (99%) and precipitated again with the addition of BuOH (hexane:BuOH = 1:1 by volume). These were redispersed in hexane. The nanocrystal dispersion was filtered through a 0.2 μm PTFE filter and diluted to 10 mg mL^{-1} in hexane before use.

Continuous wave measurements: Absorption spectra of solutions were measured on nanocrystals samples dispersed in hexane at a concentration of ca. 1 mg mL^{-1} in a 1 cm × 1 cm cuvette using a HP 8453 spectrometer. Film absorption spectra were measured on HP 8453 spectrometer, the samples were prepared on quartz glass by spin coating from a 10 mg mL^{-1} solutions at 2000 rpm for 15 sec or for polymer samples a 10 mg mL^{-1} perovskite nanocrystal dispersion in PVK 10 mg mL^{-1} in toluene was spin-coated at 2000 rpm for 60 s. Photoluminescence was measured on an Edinburgh Instruments FLS90 fluorimeter. Solution samples were measured in a 1 cm × 0.3 cm cuvette excited in the 1cm direction and imaged in the 0.3 cm direction. Film samples were excited by front face illumination at 45° to the surface, detection was at 90° degrees to excitation also at 45° to the surface.

Monte Carlo Simulations: A Monte Carlo simulation of the expected PL was constructed, using only the measured emission and absorption spectra of the constituent species. Photons are generated, travelling in random directions from the middle axis. The model is 2-dimensional, allowing light to leave the system in either the small or large axis, with dimensions 0.3 or 3 cm. Photon travel lengths are randomly generated, consistent with the concentration- and wavelength-dependent absorption lengths arising from the two species in the mix. The travel distance is then the shorter of these two distances. If this length takes the photon outside the container, it is counted towards the final spectrum if it leaves via the small axis and ignored if it leaves via the large axis. Otherwise it has a chance equal to the pure substance PLQE of being re-emitted by the species that absorbed it, in a new random direction and according to that species' emission spectrum. All values required can be measured from the single-species solutions, and the so the model contains no fitted parameters.

TCSPC measurements: The samples were prepared on quartz glass by spin coating from a 10 mg mL^{-1} perovskite nanocrystal dispersion in PVK 10 mg mL^{-1} in toluene at 2000 rpm for 60 sec. The nanocrystal films were encapsulated by affixing a glass coverslip on the nanocrystal layer using carbon tape as spacer unit and epoxy glue as sealant. The samples were excited by front face illumination at 45^o to the surface, detection was at 90^o degrees to excitation also at 45^o to the surface.

TEM: TEM samples were prepared by drop casting a ca. 40 mg mL^{-1} perovskite crystals solution in octane on a TEM Grid (200 Mesh Cu, Agar Scientific) in a argon-filled glove box. HAADF-STEM and EELS analysis were also conducted on a FEI Tecnai Osiris TEM/STEM 80-200 microscope, operating at 80 kV, using a liquid nitrogen holder, and equipped with a Gatan Enfinium ER 977 spectrometer with Dual EELS. The convergence and collection angles used were 8.5 and 34 mrad, respectively. The EELS spectral images were analyzed using principal component analysis and the elemental maps with the absolute quantification were obtained through the use of the integration method proposed by R. Egerton[56]. The EELS data analysis and elemental quantification were performed using the open source software package HyperSpy[57] toolbox.

XRD: Perovskite nanocrystals films were prepared by drop casting a 10 mg mL^{-1} nanocrystals solution in hexane on silicon wafers. X-ray diffraction experiments were carried out on a Brucker X-ray diffractometer using a CuKα radiation source (λ = 1.5418 Å). The measurements were taken from 2θ of 10° to 70° with a step size of 0.0102° in 2θ.

Film thickness: Film thicknesses were measured using a DEKTAK profilometer and a Digital Instruments/Veeco Dimension 3100 atomic force microscope (AFM).

PLQE measurements: Nanocrystal films were placed in an integrating sphere and were photo-excited using a 405 nm continuous-wave laser. The laser and the emission signals were measured and quantified using a calibrated Andor iDus DU490A InGaAs detector for the determination of PL quantum efficiency. PLQE was calculated as per de Mello, et al.[58].

LED Device Fabrication: Poly(3,4-ethylenedioxythiophene) polystyrene sulfonate (Pedot:PSS) was spin-coated onto an ITO-coated glass substrate at 6000 rpm for 45s, followed by annealing at 140°C for 30 min in a nitrogen-filled glovebox. A 10 mg mL-1 perovskite nanocrystal dispersion in PVK 10 mg mL^{-1} in toluene was spin-coated at 2000 rpm for 60 s in an argon filled glove box to give a 50–60 nm film. The samples were then transferred into a thermal evaporator and calcium (Ca; 20 nm) and silver (Ag; 80 nm) were deposited through a shadow mask at 3×10^{-6} mbar or better. The LEDs were encapsulated by affixing a glass slide on top of the contacts using transparent UV epoxy glue.

LED Characterization: Current versus voltage characteristics were measured using a Keithley 2400 source measure unit. Photon flux was measured simultaneously using a calibrated silicon photodiode centered over the light-emitting pixel. Luminance in cd m^{-2} was calculated based on the emission spectrum of the LED, weighted against the standard luminosity function and on the known spectral response of the silicon photodiode. External quantum efficiency was calculated assuming a Lambertian emission profile. Electroluminescence spectra were measured using a Labsphere CDS-610 spectrometer.

5.4 Results

5.4.1 Photo-physical and structural characterization of mixed CsPbCl3:CsPbI3 samples

$CsPbX_3$ (X = Cl, I) nanocrystals were prepared as previously reported by Protesescu et al.[21] (details in methods section). We find that $CsPbCl_3$ and $CsPbI_3$ nanocrystals co-exist in solution without undergoing halogen exchange. To investigate the optical properties of this system we prepared solutions of $CsPbCl_3$ and $CsPbI_3$ at an overall crystal concentration of ≈ 1 mg mL^{-1} (Figure 5-1 (a)).

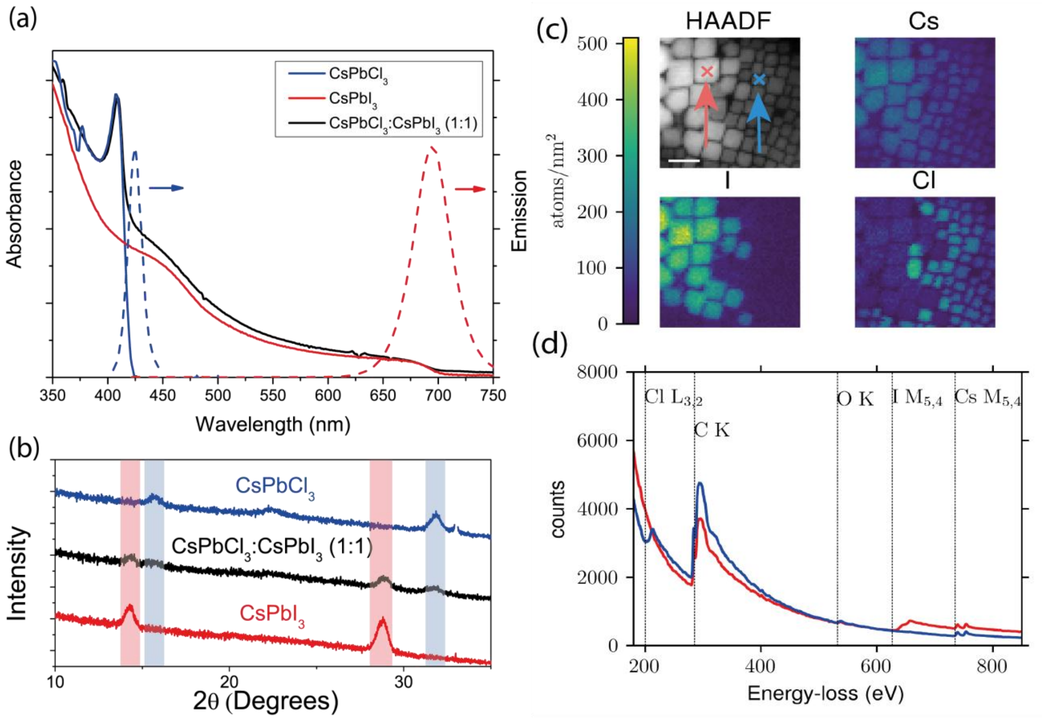

Figure 5-1: Photo-physical and structural characterization of mixed $CsPbCl_3$:$CsPbI_3$ samples. (a) Absorption spectra (left) of pure $CsPbCl_3$, $CsPbI_3$ and a 1:1 nanocrystal blend and emission spectra (right) of pure $CsPbCl_3$ and $CsPbI_3$ in hexane (concentration ≈ 1 mg mL^{-1}). (b) Powder XRD patterns of $CsPbCl_3$, $CsPbI_3$ and 1:1 nanocrystal blend solid films with distinctive peak highlighted. (c) HAADF TEM images and EELS TEM maps for Cs, I and Cl. Scale bar = 20 nm. (d) EELS TEM spectrum for $CsPbCl_3$:$CsPbI_3$ (1:1) samples taken at the positions of the red and blue crosses in (c). Lines indicate atomic absorption edges.

The respective absorbance spectra are shown in Figure 5-1 (a). We find absorbance onsets of 425 nm and 690 nm for the $CsPbCl_3$ and $CsPbI_3$ samples respectively. The $CsPbCl_3$ nanocrystals show a sharp peak close to the absorption onset, which likely arises from excitonic effects. Mixed solutions show a combination of the characteristic features of the pure nanocrystal solutions without any spectral shifting. By fitting the absorbance spectrum of the mixed solution with a sum of the pure sample spectra, we calculate the ratio of the different crystals in a nominally 1:1 mixed solution sample to be 1:0.957 ($CsPbCl_3$:$CsPbI_3$) (Figure 5-2).

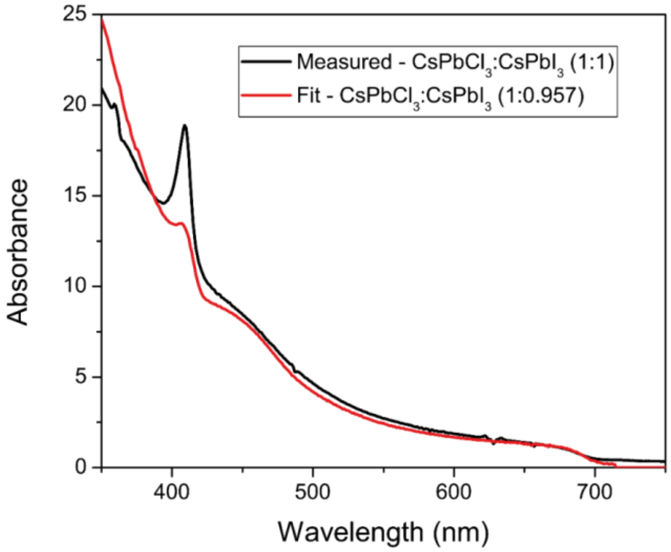

Figure 5-2: Measured absorbance and modelled absorbance spectrum of the mixed 1:1 solutions.

To investigate the structural and physical properties of the mixed system by powder X-ray diffraction (XRD) and transmission electron microscopy (TEM), neat films of the crystals were drop cast from a 10 mg mL-1 solution respectively onto silicon and onto carbon-coated copper substrates. The XRD pattern (Figure 5-1 (b)) shows peaks at 16° and 32.5° corresponding to those found in pure CsPbCl3 crystals reported by Protesescu et al.[21] and similarly at 14° and 28° in the pure CsPbI3 crystals. The XRD pattern of the $CsPbCl_3$:$CsPbI_3$ (1:1) sample is a superposition of the $CsPbCl_3$ and $CsPbI_3$ nanocrystal XRD patterns. The presence of both $CsPbCl_3$ and $CsPbI_3$ peaks in the blends, without any shifts or additional peaks, indicates that these crystal structures exist in parallel in our NC blend films. High-angle annular dark field (HAADF) TEM imaging (Figure 5-1 (c)) shows two distinct types of nanocrystals with slightly different contrasts and sizes, suggesting two different nanocrystal populations. Electron energy loss spectroscopy (EELS) and scanning transmission electron microscopy (STEM) was then used to further assign these crystal populations and obtain an absolute quantification of each element. The individual elemental maps with number of atoms per nm^2, shown in Figure 5-1 (c), indicate that the iodide is localized on the larger crystals while the chloride is localized on the smaller crystals. The amount of I and Cl in the nanocrystals maintains a 3:1 stoichiometric ratio with Cs. The EELS spectra measured at the two locations in Figure 5-1 (c) show two distinct traces for different nanocrystal populations and are shown in Figure 5-1 (d). The blue trace, corresponding to EELS measurements at the blue cross, is assigned to a $CsPbCl_3$ nanocrystal with edges seen for Cs, C, Cl and O, and the red trace, corresponding to EELS measurements at the red cross, is assigned to a $CsPbI_3$ nanocrystal with edges seen for Cs, C, I and O. The sizes of the $CsPbCl_3$ and $CsPbI_3$ nanocrystals were measured at 7.0±2.8 nm and 12.0±3.9 nm respectively. These data confirm that the $CsPbCl_3$ and $CsPbI_3$ nanocrystals are intimately mixed but remain discrete entities with insignificant halide mixing between them. The data in Figure 5-1 support our conclusion that $CsPbCl_3$ and $CsPbI_3$ do not undergo significant halogen exchange with each other. The lack of halogen exchange in these systems is assigned to the different tolerance factors of the different crystal lattices acting to inhibit halogen exchange[59].

5.4.2 Photoluminescence of mixed CsPbCl3:CsPbI3 samples

The ability of these crystals to exist as discrete entities gives us the unique opportunity to study these crystals and their photo-physical interactions with each other. $CsPbCl_3$ nanocrystals emit in the near-UV at 425 nm, whereas $CsPbI_3$ nanocrystals emit in the red at 695 nm (Figure 5-1 (a)). When excited at 365 nm, nanocrystals dispersed in a PMMA matrix at a total nanocrystal:polymer ratio of 1:1 by weight (film thickness $\approx$ 20 nm) (Figure 5-3 (a)) and neat mixed nanocrystal films spun from toluene (Figure 5-3 (b)), clearly show emission from both types of nanocrystals. Spectral tuning of the separate crystals was also achievable by incorporating a small (weight fraction $\leq$ 10%) amount of CsPbBr3 nanocrystals in a solution of $CsPbCl_3$ and $CsPbI_3$ nanocrystals. As there is not enough $CsPbBr_3$ to represent a majority, the $CsPbBr_3$ is incorporated into the $CsPbCl_3$ and $CsPbI_3$ crystals resulting in a $CsPbCl_{(3-x)}Br_x$ and $CsPbI_{(3-x)}Br_x$ blend (Figure 5-3 (c)).

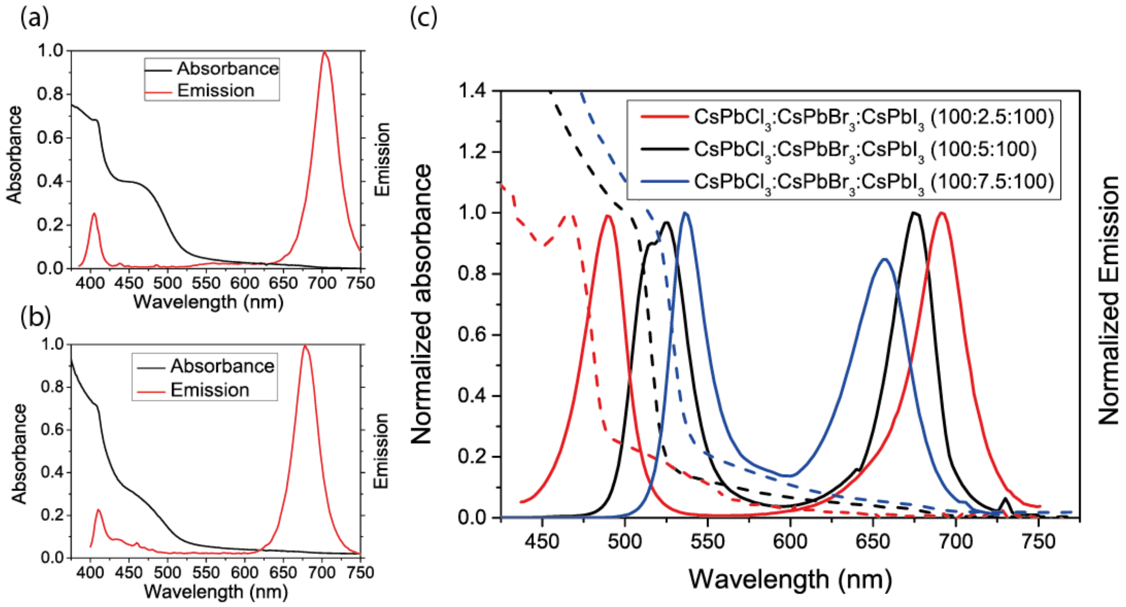

Figure 5-3: Mixed cesium lead halide perovskite photoluminescence. (a) Solid state absorbance and emission spectra of $CsPbCl_3$:$CsPbI_3$ (1:1) in PMMA, film thickness ≈ 20 nm (10 mg mL^{-1} nanocrystals and 10 mg mL^{-1} PMMA in toluene, spun at 6000 rpm) (b) Solid state absorbance and emission in neat mixed crystal films (10mg mL^{-1} in toluene, spun at 2000 rpm. (c) Absorbance and emission of ≈ 0.1 mg mL^{-1} nanocrystal in toluene) with different $CsPbCl_3$:$CsPbBr_3$:$CsPbI_3$ ratios.

When excited directly at 550 nm, the overall photoluminescence quantum yield (PLQE) of the $CsPbI_3$ crystals decreased with increasing $CsPbCl_3$ ratios (Figure 5-4 (a)). Despite there being no change in XRD (Figure 5-4 (b)) or the emission spectrum, TEM images show a small amount of migration of chloride ions into the $CsPbI_3$ crystals (Figure 5-1 (c) and Figure 5-5). We attribute this decrease in PLQE to small amounts of chloride migration which increases the amount of non-radiative decay within the crystals. This is consistent with time-correlated single-photon counting (TCSPC) measurements (Figure 5-6), which show the $CsPbI_3$ fluorescence decay lifetimes are shortened for ratios greater that 1:1. We are still able to achieve high PLQEs in the $CsPbI_3$ nanocrystals at a 1:1 ratio.

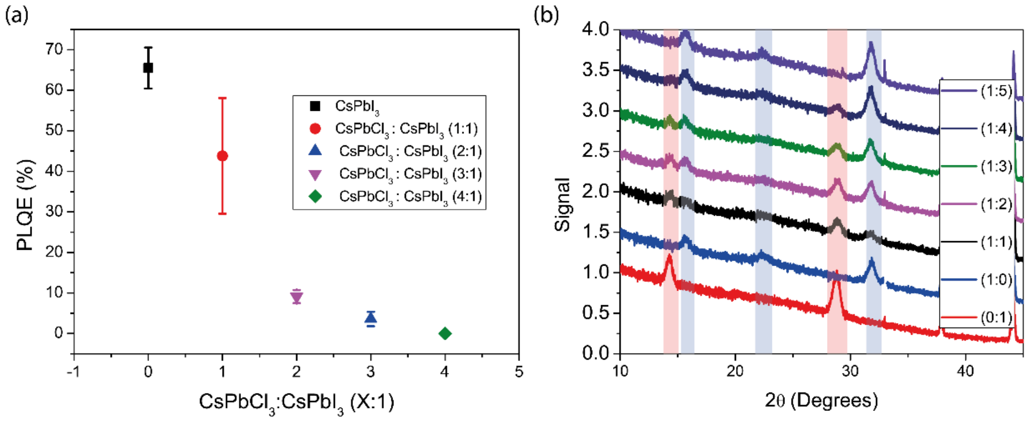

Figure 5-4: PLQE and XRD measurements. (a) Photoluminescence quantum efficiency of different CsPbCl$_3$:CsPbI$_3$ blend ratios in PMMA.(b) Powdered X-ray diffraction pattern of different CsPbCl3:CsPbI3 (x:y) blend ratios in PMMA. Highlighted region denote peaks associated with CsPbI3 nanocrystals (red) and CsPbCl3 nanocrystals (blue).

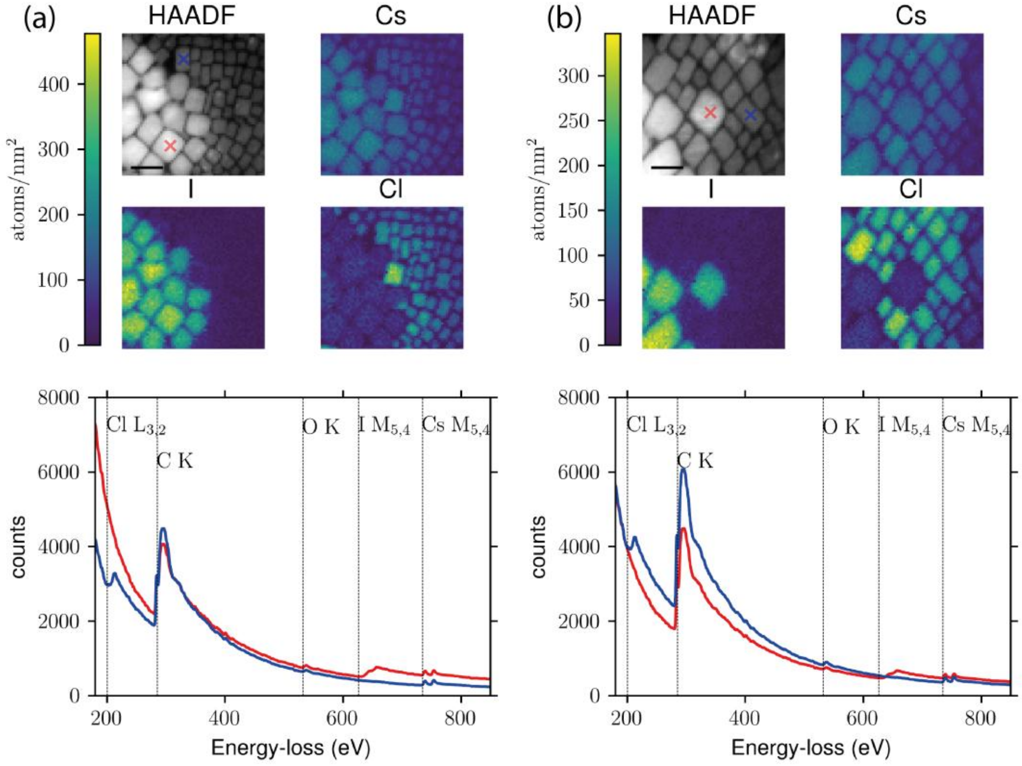

Figure 5-5: Two different ((a) and (b)) HAADF and EELS TEM scans of different regions. Both samples show CsPbCl$_3$ and CsPbI$_3$ nanocrystals are not homogenously mixed. Lines indicated atom absorption edges.

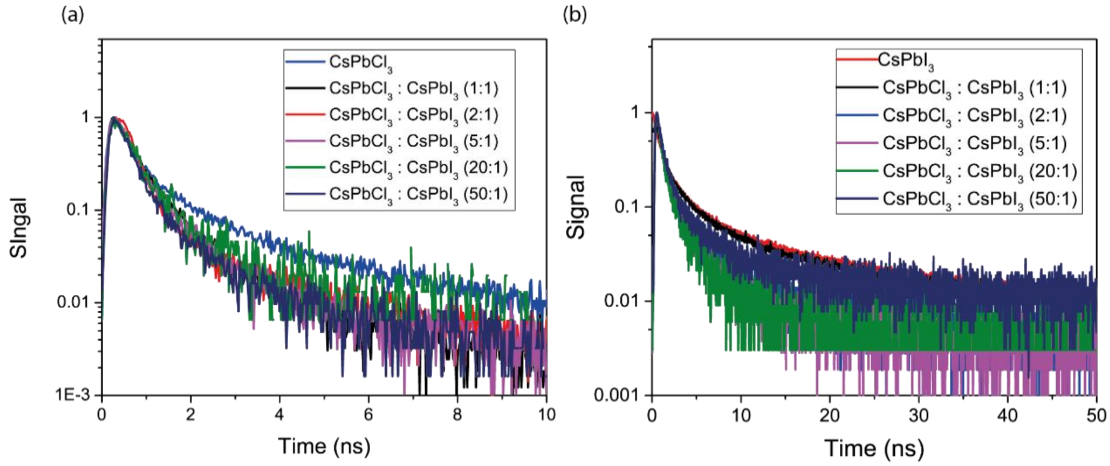

Figure 5-6: Transient decays for different nanocrystal polymer films excited at 405 nm and measured at 450 nm (a) and 670 nm (b).

The above spectra (Figure 5-3 (a) and (b)) showed emission from both $CsPbCl_3$ and $CsPbI_3$ nanocrystals, however when $CsPbCl_3$ and $CsPbI_3$ nanocrystals are mixed in a 1:1 ratio at higher solution concentrations and in thicker polymer matrices, the emission was found to be predominantly at 695 nm under 405 nm excitation. Solutions of $CsPbCl_3$ and $CsPbCI_3$ nanocrystals showed emission solely from the $CsPbI_3$ crystals up until a 20-fold excess of $CsPbCl_3$ (Figure 5-7).

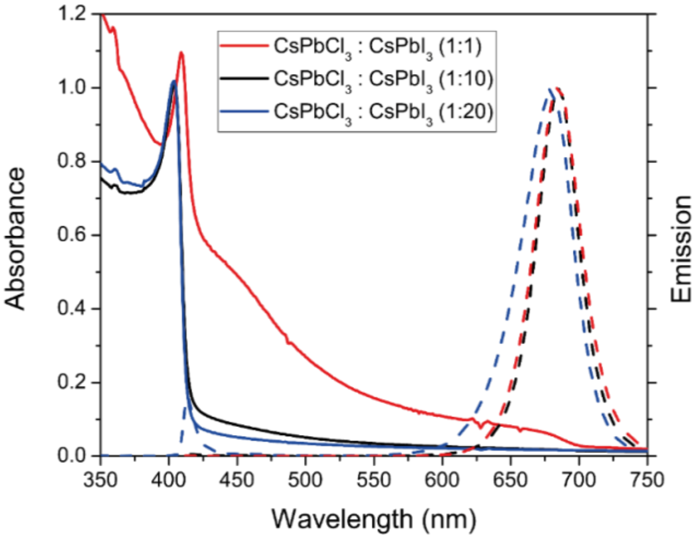

Figure 5-7: Solution absorbance (solid) and emission (dashed) of CsPbCl3:ClPbI3 blends in hexane. While the concertation of CsPbI3 remained constant at 0.021 mg mL^{-1}, the concretion of $CsPbCl_3$ was 0.021 mg mL^{-1}, 0.21 mg mL^{-1} and 0.42 mg mL^{-1} for the 1:1, 1:10, 1:20 blends respectively.

Emission solely from the low-energy particles was also seen for nanocrystals dispersed in a PMMA matrix at a total nanocrystal:polymer ratio of 1:1 by weight and film thickness ≈ 75 nm, Figure 5-8 (a). These results indicate that there is efficient energy transfer to the low-energy nanocrystals.

5.4.3 Transient photoluminescence measurements

The interaction responsible for this energy transfer in solid films was investigated through transient spectroscopy techniques. For mixed samples with a 1:1 ratio $CsPbCl_3$:$CsPbI_3$ by weight, the $CsPbI_3$ nanocrystals show an increased lifetime when excited at 405nm compared to pure $CsPbI_3$ samples (Figure 5-8 (b)). Consistent with steady state measurements, there was no emission from the $CsPbCl_3$ nanocrystals in the mixed samples. An extended luminescent lifetime in the lower-energy particle is consistent with excitation transfer.

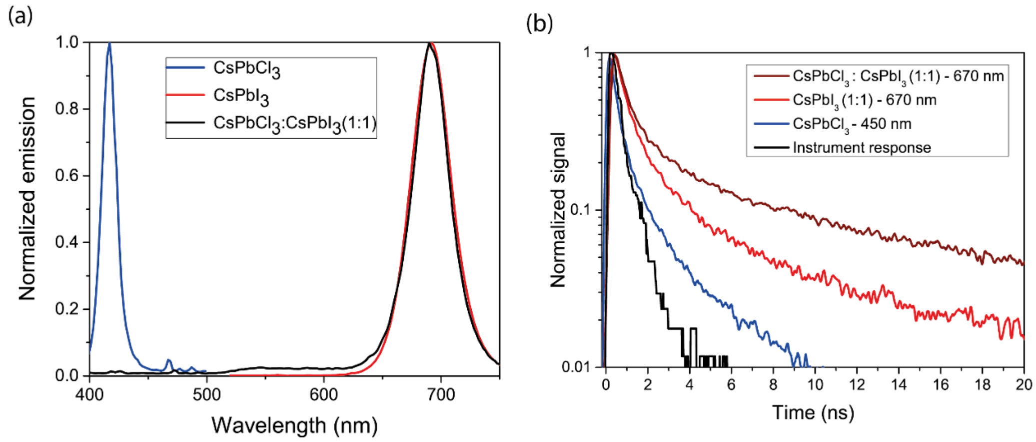

Figure 5-8: Photoluminescence measurements. (a) Luminescence of $CsPbCl_3$, $CsPbI_3$, $CsPbCl_3$:$ClPbI_3$ blends in PMMA matrix at a total nanocrystal:polymer ratio of 1:1 by weight and film thickness ≈ 75 nm. (b) Transient luminescence decays excited at 405 nm with measurements at 450 nm or 670 nm.

One possible mechanism for this energy transfer is Förster resonance energy transfer (FRET). We calculate the Förster radius R_o, the distance at which 50% of all excitations lead to energy transfer from the donor to the acceptor[60], using measured absorption, emission and PLQE data to be 6.8±0.3 nm. This value is comparable to the size of the nanocrystals so the point dipole approximation stipulated in FRET calculations is not entirely appropriate. It is also worth noting that the large aliphatic ligands that offer colloidal stability are still attached to these crystals. This combined with the apparent slight phase separation of the two crystals in neat films (Figure 5-1

(c) and Figure 5-5) and the fact that the crystals are supported in a polymer matrix means that the distance between a $CsPbCl_3$ and $CsPbI_3$ particle is generally greater than 6.8 nm. We cannot completely rule out FRET playing a role in energy transfer, but crucially the fact that energy transfer is more complete in thick films, with the same inter-particle spacing, suggests that another mechanism is dominating. We therefore ascribe the dominant emission from $CsPbI_3$ nanocrystals in $CsPbCl_3$:$CsPbI_3$ blends to efficient reabsorption of photons emitted from $CsPbCl_3$ nanocrystals. A Monte Carlo algorithm allowing for multiple absorption and re-emission events gives an accurate replication of the measured emission in concentrated solutions and shows the measured down-conversion of the blue emission to red (Figure 5-9).

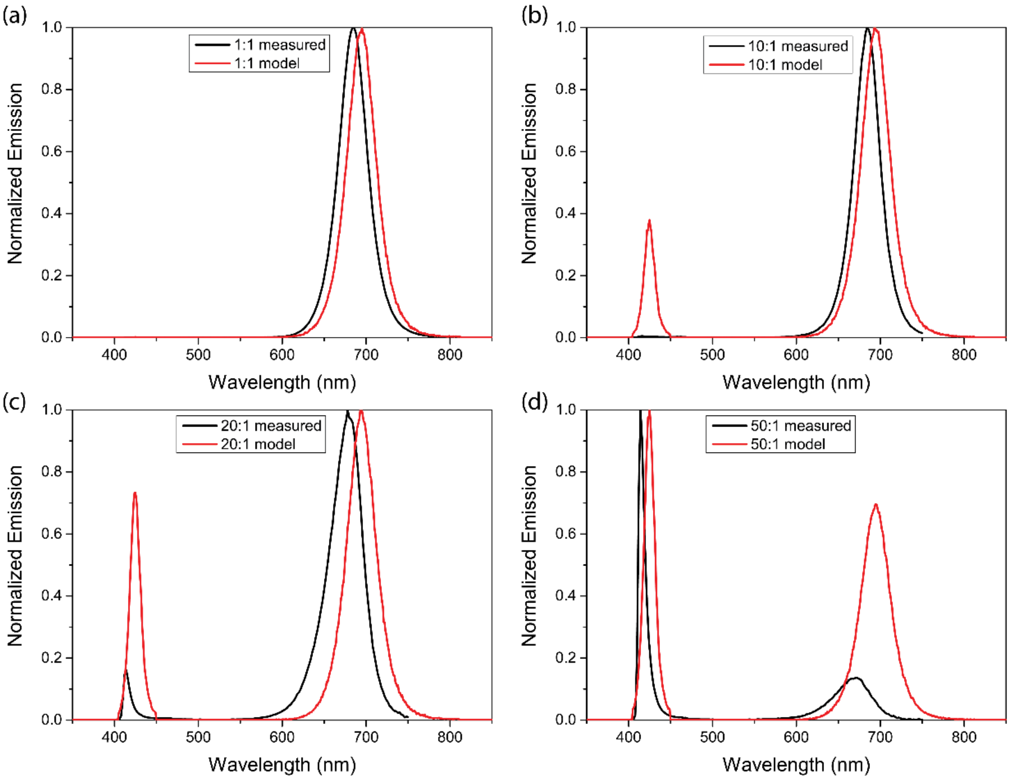

Figure 5-9: Monte Carlo simulations of emission spectra from different nanocrystal solutions with different $CsPbCl_3$:$CsPbI_3$ ratios ((a)-(d)). The results of these simulations show that we expect there to only be a red peak visible from the 1:1 $PbCsCl_3$:$PbCsI_3$ mixture, but that a blue peak should grow as the $PbCsCl_3$ fraction increases, becoming larger than the red peak when we have a 50:1 ratio. This is qualitatively consistent with the measured behavior.

5.4.4 LED device fabrication and characterisation

To use the potential of this efficient photon reabsorption between different $CsPbX_3$ (X = Cl, I) nanocrystals, we incorporated them into bulk heterojunction polymer/$CsPbX_3$ nanocrystal LEDs. The LEDs were made by spin coating poly(3,4-ethylenedioxythiophene):polystyrene sulfonate (PEDOT:PSS) on an indium-tin oxide (ITO) glass substrate. A toluene solution containing 10 mg mL^{-1} nanocrystal and 10 mg mL^{-1} poly(9-vinylcarbazole) (PVK) was further spun on top, giving a 50-60 nm film, and a calcium and silver electrode was deposited by thermal evaporation (Figure 5-10 (a)). Devices of $CsPbCl_3$, $CsPbI_3$, $CsPbCl_3$:$CsPbI_3$ (1:1) (all in PVK matrices), and pure PVK were produced.

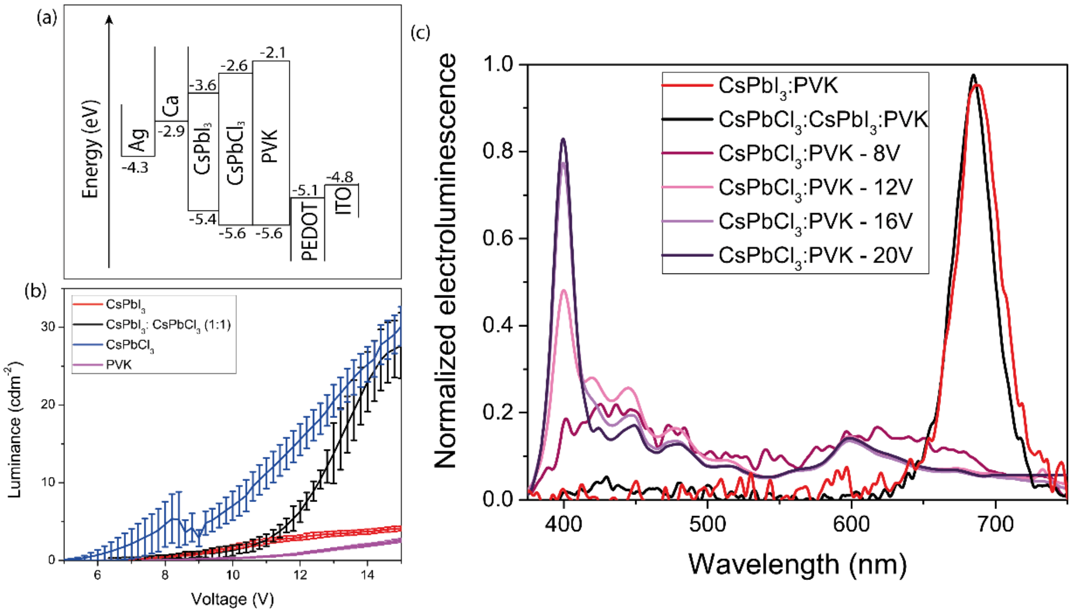

Figure 5-10: Bulk heterojunction LEDs. (a) Band diagram and structure of the bulk heterojunction LEDs. (b) Change in luminance with voltage in the bulk heterojunction LEDs. (c) Electroluminescence spectra of $CsPbI_3$:PVK, $CsPbCl_3$:$CsPbI_3$:PVK and $CsPbCl_3$:PVK at different voltages. The electroluminescence spectra of the $CsPbI_3$:PVK and $CsPbCl_3$:$CsPbI_3$:PVK remain constant with voltage (not shown).

All devices were inefficient, with quantum efficiencies less than 0.04% (Figure 5-11 (a)), and relatively high voltages were required to achieve significant luminances (Figure 5-10 (b)). Devices containing PVK showed broad emission, consistent with previous reports[61,62], and had the highest current densities (Figure 5-11 (b)). Adding $CsPbCl_3$ particles had only a minor effect on the current density (Figure 5-11 (b)), but at high voltages led to a clear emission peak around 400 nm (Figure 5-10 (c)), consistent with charge capture and recombination occurring on the particles. With $CsPbI_3$ particles, the emission was solely from the particles, centered around 695 nm (Figure 5-10 (c)), but the current density was reduced by an order of magnitude (Figure 5-11 (b)), consistent with trapping of one or both carriers on the particles. Mixed $CsPbCl_3$:$CsPbI_3$/PVK devices maintain the high current densities comparable to that of the PVK and $CsPbCl_3$/PVK devices but show emission solely from the $CsPbI_3$ nanocrystals (Figure 5-10 (c) and Figure 5-11 (b)). This suggests that transport is dominated by the $CsPbCl_3$ particles but that any emission occurring from the $CsPbCl_3$ particles is converted to $CsPbI_3$ emission through photon reabsorption as demonstrated in the optical measurements described above. Devices containing mixed nanoparticles therefore show the best device performance. It would be attractive to obtain a mixture of blue and red emission in LEDs, which would require thinner films of mixed nanoparticles to avoid complete reabsorption of the blue emission as demonstrated optically in Figure 5-3. Unfortunately, though, we have not yet been able to fabricate working LEDs with active layer thicknesses below 40 nm.

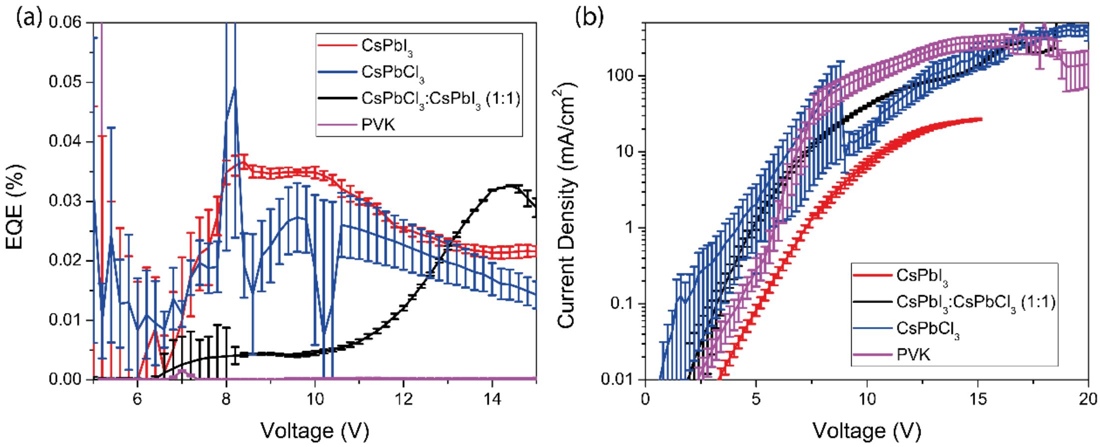

Figure 5-11: LED device characteristics. (a) External quantum efficiencies of LED devices. (b) Current density/voltage characteristic of LED devices.

5.5 Conclusion

In conclusion we present the study of interactions in blends films with mixtures of different $CsPbX_3$ (X = Cl, I) perovskite nanocrystals. We find that $CsPbCl_3$ and $CsPbI_3$ nanocrystals can exist as discrete entities in solution, embedded in a polymer matrix and as neat films. The $CsPbCl_3$ emission can be reabsorbed by the $CsPbI_3$

nanocrystals due to the large absorption coefficient of the $CsPbI_3$ nanocrystals in the range of the $CsPbCl_3$ emission. This phenomenon can be utilized in bulk heterojunction LEDs where the luminance of devices emitting in the 695 nm region can be improved by the incorporation of $CsPbCl_3$ nanocrystals. This causes the devise to operate at a higher current density with photon reabsorption transfer occurring from the $CsPbCl_3$ nanocrystals to the $CsPbI_3$ crystal for efficient reemission.

5.6 On Going Research

In the LEDs presented, it was difficult to accurately clarify what was happening in the devices in terms of charge transport and charge recombination. Creating field effect transistors similar to the described LEDs would enable measurements of the electron and hole motilities within the devices to further clarify their operation.

The concentration of excitations into $CsPbI_3$ nanocrystals was also shown in the LEDs. This could be further extended by increasing the relative concentration of $CsPbCl_3$. Currently the decrease in PLQE with increased $CsPbCl_3$ component in mixed samples inhibits this approach, but if this could be over-come it opens up a variety of applications including optically and electrically pumped lasers, which would take advantage of the high excitation densities on the $CsPbI_3$ nanocrystal. Indeed it might be possible to create visibly transparent LSCs suitable for windows operating through transfer from high concentrations of $CsPbCl_3$ to minimal $CsPbI_3$ nanocrystals.

Throughout this project I tried to prevent halogen exchange through a number of different ways. Prevention methods which showed little success included attempts at creating semiconductor shells around the perovskite nanocrystals, usually this lead to the removal of the ligands that offered colloidal stability, which are known to be dynamic in cesium lead halide perovskite nanocrystals[63], leading to aggregation of the nanocrystals (Figure 5-12). It is worth nothing that as the explored shells were usually formed by cation exchange, even in aggregated samples, halogen exchange was still found to occur.

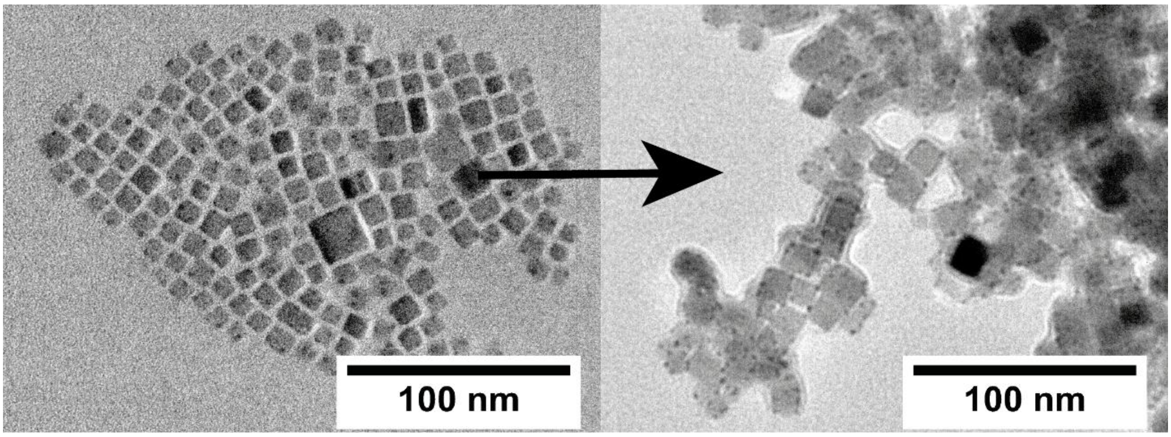

Figure 5-12: Attempted core shell experiments using Cd olate. Note the aggregation in the second picture.

One way of preventing halogen exchange and possibly the degradation described was recently published by Huang et al.[53]. In this publication the researchers wrap individual and aggregates of $CsPbX_3$ nanocrystals with polyhedral oligomeric silsesquioxane (POSS) (Figure 5-13). By preventing halogen exchange numerous optoelectronic applications now become feasible with $CsPbX_3$ nanocrystals, specifically white light phosphors and LEDs which require incorporation of different crystal colors into a single active layer. Although the polymer shell could prevent charge injection, theoretically it should be possible to totally prevent halogen exchange and preserve charge transfer though the use of inorganic shell structures or possibly short chain polymeric ligand shells.

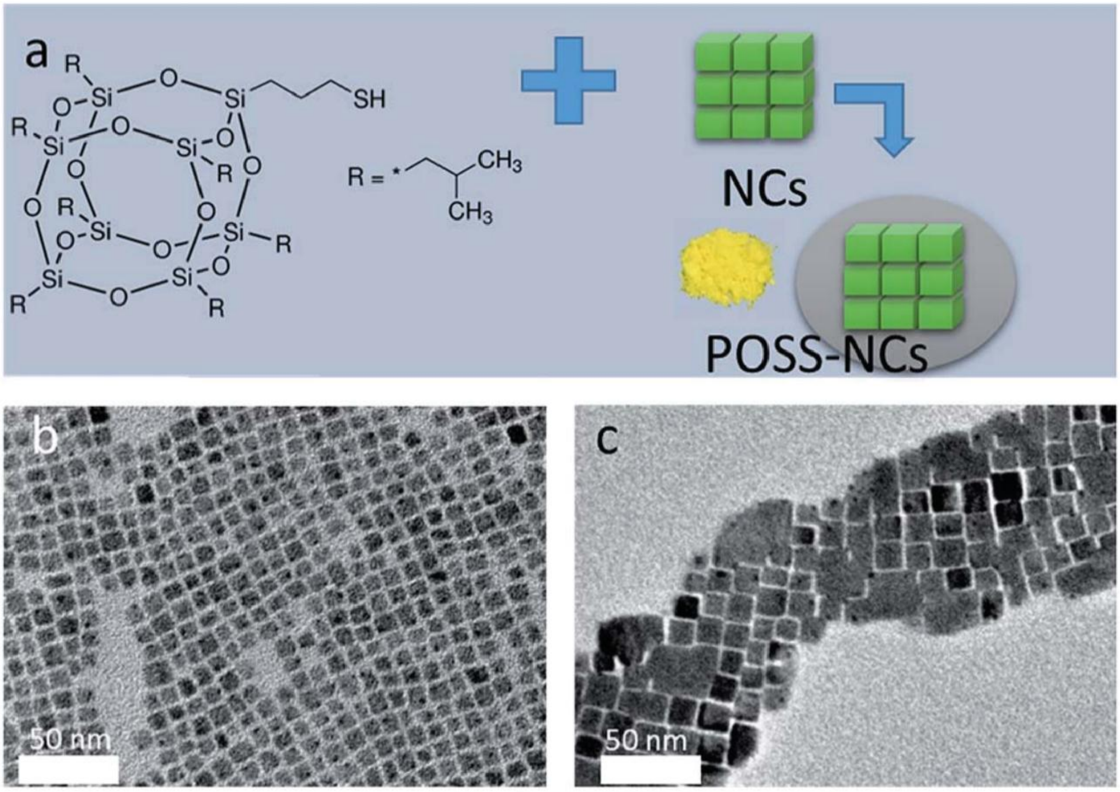

Figure 5-13: Results from Huang *et al.*[53] (a) Structure of a thiol-functionalized POSS, with a schematic diagram illustrating the POSS coating process for preparation of perovskite NC powders. (b and c) TEM images of CsPbBr3 perovskite NCs before and after POSS coating respectively. Figure taken from Huang, et al.: Chem. Sci. 2016, 7, 5699–5703 - Water resistant $CsPbX_3$ nanocrystals coated by polyhedral oligomeric silsesquioxane and their use as solid state luminophores in all-perovskite white light emitting devices.

While investigating the cesium lead halide perovskite nanocrystals I also explored ways to take advantage of the rapid halogen exchange to form $CsPbF_3$ nanocrystals from $CsPbCl_3$ nanocrystals. This work initially showed promise with the formation of what appears to be $CsPbF_3$ nanocrystals, however due to stability issues and time constraints further analysis has not been completed. Briefly, CsF salt was dissolved in water. A solution of $CsPbCl_3$ in hexane was layered on top of the water and left to sit overnight. The hexane solution was then pipetted from the top resulting, in what is believed to be, $CsPbF_3$ nanocrystals. UV-Vis and photoluminescence spectroscopy, in addition to TEM, were measured as these techniques are suitable for analysis of low concentration solutions of nanoparticles (Figure 5-14). The $CsPbF_3$ nanocrystals show similar size distribution to the parent $CsPbCL_3$ nanocrystals (Figure 5-14 (b and c)) but have a blue shifted emission down to 280 nm (Figure 5-14 (a)). This is what would be expected of a halogen exchange to $CsPbF_3$, as it follows the trend of moving to higher energy as you go up along the halogen group on the periodic table. Difficulties arose when the measurement technique required the nanocrystals to be removed from the suspension. Hexane and water are immiscible, but a minimal amount of water does dissolve in the hexane solution. As the perovskite nanocrystals are sensitive to water, when solutions were drop casts the differences in volatility between hexane and water caused the hexane to evaporate first leaving water to degrade the crystals. This meant measurements such as XRD only showed a degraded mixture of CsF and PbF. The solubility of fluoride salts used in the project necessitated the need to include water in the experimental produce. For future experiments I would recommend the development of a procedure of creating the $CsPbF_3$ nanocrystals without the inclusion of water. Possible by using tetrafluorborate or its various analogues which are soluble in organic solvents.

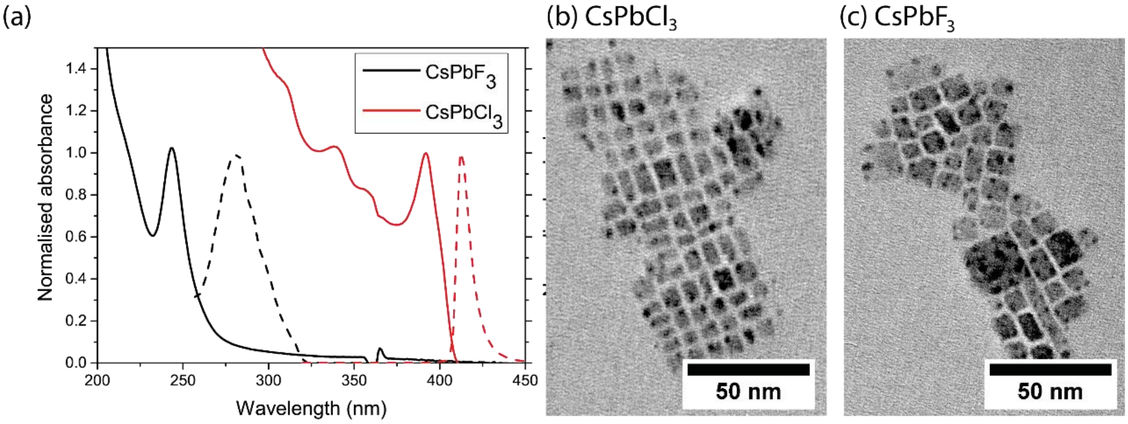

Figure 5-14: $CsPbF_3$ nanocrystals. (a) Normalised absorption (solid) and emission (dashed) spectra of $CsPbCl_3$ and $CsPbF_3$ nanocrystals. TEM images of $CsPbCl_3$ (b) and $CsPbF_3$ (c) nanocrystals.

5.7 References

(1) Kojima, A.; Teshima, K.; Shirai, Y.; Miyasaka, T. *J. Am. Chem. Soc.* **2009**, *131*, 6050–6051.

(2) Lee, M.; Teuscher, J.; Miyasaka, T. *Science* **2012**, *338*, 643–648.

(3) Burschka, J.; Pellet, N.; Moon, S.-J.; Humphry-Baker, R.; Gao, P.; Nazeeruddin, M. K.; Grätzel, M. *Nature* **2013**, *499*, 316–319.

(4) Nie, W.; Tsai, H.; Asadpour, R. *Science* **2015**, *347*, 522–525.

(5) Stranks, S.; Eperon, G.; Grancini, G. *Science* **2013**, *342*, 341–345.

(6) Xing, G.; Mathews, N.; Sun, S.; Lim, S. *Science* **2013**, *342*, 498–500.

(7) Dong, Q.; Fang, Y.; Shao, Y.; Mulligan, P. *Science* **2015**, *347*, 967–970.

(8) Tan, Z.-K.; Moghaddam, R. S.; Lai, M. L.; Docampo, P.; Higler, R.; Deschler, F.; Price, M.; Sadhanala, A.; Pazos, L. M.; Credgington, D.; Hanusch, F.; Bein, T.; Snaith, H. J.; Friend, R. H. *Nat. Nanotechnol.* **2014**, *9*, 687–692.

(9) Zhang, W.; Anaya, M.; Lozano, G.; Calvo, M. E.; Johnston, M. B.; Míguez, H.; Snaith, H. J. *Nano Lett.* **2015**, *15*, 1698–1702.

(10) Xing, G.; Mathews, N.; Lim, S. S.; Yantara, N.; Liu, X.; Sabba, D.; Grätzel, M.; Mhaisalkar, S.; Sum, T. C. *Nat. Mater.* **2014**, *13*, 476–480.

(11) Filip, M. R.; Eperon, G. E.; Snaith, H. J.; Giustino, F. *Nat. Commun.* **2014**, *5*, 5757.

(12) Pazos-Outón, L. M.; Szumilo, M.; Lamboll, R.; Richter, J. M.; Crespo-Quesada, M.; Abdi-Jalebi, M.; Beeson, H. J.; Vrucinic, M.; Alsari, M.; Snaith, H. J.; Ehrler, B.; Friend, R. H.; Deschler, F. *Science* **2016**, *351*, 1430–1433.

(13) Green, M. A.; Ho-Baillie, A.; Snaith, H. J. *Nat. Photonics* **2014**, *8*, 506–514.

(14) Park, N. *J. Phys. Chem. Lett.* **2013**, *4*, 2425–2429.

(15) Zhou, H.; Chen, Q.; Li, G.; Luo, S.; Song, T. *Science* **2014**, *365*, 542–546.

(16) Jeon, N. J.; Noh, J. H.; Yang, W. S.; Kim, Y. C.; Ryu, S.; Seo, J.; Seok, S. Il. *Nature* **2015**, *517*, 476–480.

(17) Grätzel, M. *Nat. Mater.* **2014**, *13*, 838–842.

(18) Shi, D.; Adinolfi, V.; Comin, R.; Yuan, M.; Alarousu, E.; Buin, A.; Chen, Y.; Hoogland, S.; Rothenberger, A.; Katsiev, K.; Losovyj, Y.; Zhang, X.; Dowben, P. A.; Mohammed, O. F.; Sargent, E. H.; Bakr, O. M. *Science* **2015**, *347*, 519–522.

(19) Zhang, F.; Zhong, H.; Chen, C.; Wu, X.; Hu, X.; Huang, H. **2015**, *3*, 4533–4542.

(20) Zhang, D.; Eaton, S. W.; Yu, Y.; Dou, L.; Yang, P. *J. Am. Chem. Soc.* **2015**, *137*, 9230–9233.

(21) Protesescu, L.; Yakunin, S.; Bodnarchuk, M. I.; Krieg, F.; Caputo, R.; Hendon, C. H.; Yang, R. X.; Walsh, A.; Kovalenko, M. V. *Nano Lett.* **2015**, *15*, 3692–3696.

(22) Jellicoe, T. C.; Richter, J. M.; Glass, H. F. J.; Tabachnyk, M.; Brady, R.; Dutton, S. E.; Rao, A.; Friend, R. H.; Credgington, D.; Greenham, N. C.; Böhm, M. L. *J. Am. Chem. Soc.* **2016**.

(23) Dou, L.; Yang, Y. M.; You, J.; Hong, Z.; Chang, W.-H.; Li, G.; Yang, Y. *Nat. Commun.* **2014**, *5*, 5404.

(24) Guo, Y.; Liu, C.; Tanaka, H.; Nakamura, E. *J. Phys. Chem. Lett.* **2015**, *6*, 535–539.

(25) Yakunin, S.; Sytnyk, M.; Kriegner, D.; Shrestha, S.; Richter, M.; Matt, G. J.; Azimi, H.; Brabec, C. J.; Stangl, J.; Kovalenko, M. V.; Heiss, W. *Nat. Photonics* **2015**, *9*, 444–449.

(26) Sutherland, B. R.; Johnston, A. K.; Ip, A. H.; Xu, J.; Adinolfi, V.; Kanjanaboos, P.; Sargent, E. H. *ACS Photonics* **2015**, *2*, 1117–1123.

(27) Maculan, G.; Sheikh, A. D.; Abdelhady, A. L.; Saidaminov, M. I.; Haque, M. A.; Murali, B.; Alarousu, E.; Mohammed, O. F.; Wu, T.; Bakr, O. M. *J. Phys. Chem. Lett.* **2015**, *6*, 3781–3786.

(28) Wang, Y.; Li, X.; Song, J.; Xiao, L.; Zeng, H.; Sun, H. *Adv. Mater.* **2015**, *27*, 7101–7108.

(29) Sutherland, B.; Hoogland, S.; Adachi, M. *ACS Nano* **2014**, *8*, 10947–10952.

(30) Zhang, Q.; Ha, S. T.; Liu, X.; Sum, T. C.; Xiong, Q. *Nano Lett.* **2014**, *14*, 5995–6001.

(31) Deschler, F.; Price, M. *J. Phys. Chem. Lett.* **2014**, *5*, 14.21–1426.

(32) Zhu, H.; Fu, Y.; Meng, F.; Wu, X.; Gong, Z.; Ding, Q.; Gustafsson, M. V; Trinh, M. T.; Jin, S.; Zhu, X.-Y. *Nat. Mater.* **2015**, *14*, 636–642.

(33) Shen, H.; Cao, W.; Shewmon, N. T.; Yang, C.; Li, L. S.; Xue, J. *Nano Lett.* **2015**, *15*, 1211–1216.

(34) Kim, Y.-H.; Cho, H.; Heo, J. H.; Kim, T.-S.; Myoung, N.; Lee, C.-L.; Im, S. H.; Lee, T.-W. *Adv. Mater.* **2015**, *27*, 1248–1254.

(35) Stranks, S. D.; Snaith, H. J. *Nat. Nanotechnol.* **2015**, *10*, 391–402.

(36) Chung, I.; Lee, B.; He, J.; Chang, R. P. H.; Kanatzidis, M. G. *Nature* **2012**, *485*, 486–489.

(37) Hao, F.; Stoumpos, C. C.; Cao, D. H.; Chang, R. P. H.; Kanatzidis, M. G. *Nat. Photonics* **2014**, *8*, 489–494.

(38) Jang, D. M.; Park, K.; Kim, D. H.; Park, J.; Shojaei, F.; Kang, H. S.; Ahn, J.-P.; Lee, J. W.; Song, J. K. *Nano Lett.* **2015**, *15*, 5191–5199.

(39) Pellet, N.; Teuscher, J.; Maier, J.; Grätzel, M. *Chem. Mater.* **2015**, *27*, 2181–2188.

(40) Akkerman, Q. A.; D'Innocenzo, V.; Accornero, S.; Scarpellini, A.; Petrozza, A.; Prato, M.; Manna, L. *J. Am. Chem. Soc.* **2015**, *137*, 10276–10281.

(41) Nedelcu, G.; Protesescu, L.; Yakunin, S.; Bodnarchuk, M. I.; Grotevent, M. J.; Kovalenko, M. V. *Nano Lett.* **2015**, *15*, 5635–5640.

(42) Mizusaki, J.; Arai, K.; Fueki, K. *Solid State Ionics* **1983**, *11*, 203–211.

(43) Tress, W.; Marinova, N.; Moehl, T.; Zakeeruddin, S. M.; Nazeeruddin, M. K.; Grätzel, M. *Energy Environ. Sci.* **2015**, *8*, 995–1004.

(44) Park, Y.; Guo, S.; Makarov, N.; Klimov, V. *ACS Nano* **2015**, *9*, 10386–10393.

(45) Swarnkar, A.; Chulliyil, R.; Ravi, V. K.; Irfanullah, M.; Chowdhury, A.; Nag, A. *Angew. Chem. Int. Ed. Engl.* **2015**, *54*, 15424–15428.

(46) Yakunin, S.; Protesescu, L.; Krieg, F.; Bodnarchuk, M. I.; Nedelcu, G.; Humer, M.; De Luca, G.; Fiebig, M.; Heiss, W.; Kovalenko, M. V. *Nat. Commun.* **2015**, *6*, 8056.

(47) Raino, G.; Nedelcu, G.; Protesescu, L.; Bodnarchuk, M. I.; Kovalenko, M. V; Mahrt, R. F.; Stöferle, T. *ACS Nano* **2016**, *10*, 2485–2490.

(48) Lignos, I.; Stavrakis, S.; Nedelcu, G.; Protesescu, L.; DeMello, A. J.; Kovalenko, M. V. *Nano Lett.* **2016**, *16*, 1869–1877.

(49) Lee, J.-S.; Ramasamy, P.; Lim, D.-H.; Kim, B.; Lee, S.-H.; Lee, M.-S. *Chem. Commun.* **2015**, *52*, 2067–2070.

(50) Song, J.; Li, J.; Li, X.; Xu, L.; Dong, Y.; Zeng, H. *Adv. Mater.* **2015**, 7162–7167.

(51) Li, G.; Rivarola, F. W. R.; Davis, N. J. L. K.; Bai, S.; Jellicoe, T. C.; de la Peña, F.; Hou, S.; Ducati, C.; Gao, F.; Friend, R. H.; Greenham, N. C.; Tan, Z.-K. *Adv. Mater.* **2016**, 1–7.

(52) Palazon, F.; Akkerman, Q. A.; Prato, M.; Manna, L. *ACS Nano* **2016**, *10*, 1224–1230.

(53) Huang, H.; Chen, B.; Wang, Z.; Hung, T. F.; Susha, A.; Zhong, H.; Rogach, A.; Sci, C.; Huang, H.; Chen, B.; Wang, Z.; Hung, T. F.; Susha, A. S.; Zhong, H.; Rogach, A. L. *Chem. Sci.* **2016**, *7*, 5699–5703.

(54) de Weerd, C.; Gomez Navascues, L.; Zhang, H.; Buma, W. J.; Nedelcu, G.; Kovalenko, M. V.; Gregorkiewicz, T. *J. Phys. Chem. C* **2016**, *120*, 13310–13315.

(55) Nedelcu, G.; Protesescu, L.; Yakunin, S.; Bodnarchuk, M. I.; Grotevent, M.; Kovalenko, M. V. *Nano Lett.* **2015**, *15*, 5635–5640.

(56) Egerton, R. *Ultramicroscopy* **1978**, *3*, 243–251.

(57) de la Pena, F.; Burdet, P.; Ostasevicius, T.; Sarahan, M.; Nord, M.; Fauske, V. T.; Taillon, J.; Eljarrat, A.; Mazzucco, S.; Donval, G.; Zagonel, L. F.; Walls, M.; Iyengar, I. *Zenodo* **2015**.

(58) Mello, J. de; Wittmann, H.; Friend, R. *Adv. Mater.* **1997**, *9*, 230–232.

(59) Kieslich, G.; Sun, S.; Cheetham, A. K. *Chem. Sci.* **2015**, *6*, 3430–3433.

(60) Förster, T. *Discuss. Faraday Soc.* **1959**, *27*, 7–17.

(61) Yang, S.; Liu, D.; Jiang, Y.; Teng, F.; Xu, Z.; Hou, Y.; Xu, X. *J. Lumin.* **2007**, *122-123*, 614–616.

(62) Aleshin, A. N.; Sokolovskaya, A. D.; Shcherbakov, I. P.; Brunkov, P. N.; Ulin, V. P. *Phys. Solid State* **2013**, *55*, 675–680.

(63) De Roo, J.; Ibáñez, M.; Geiregat, P.; Nedelcu, G.; Walravens, W.; Maes, J.; Martins, J. C.; Van Driessche, I.; Kovalenko, M. V.; Hens, Z. *ACS Nano* **2016**, *10*,

2071–2081.

6 CONCLUSIONS

6.1 Renewable and Sustainable Energy

This thesis aimed to investigate how improvements could be made to current optoelectronic devices though the employment of specific forms of spectral management, that is:

- The conversion of high energy photons into multiple excitons to overcome the Shockley-Queisser limit in photovoltaic devices.
- The concentration of excitons in antennae complexes for use in luminescent solar concentrators.
- The utilization of energy transfer processes to improve light-emitting diodes.

6.1.1 Photovoltaics

In this thesis I have shown the development of the synthetic techniques required to produce high-quality monodisperse $CdCl_2$-treated PbSe nanorods. These nanorods were incorporated in working photovoltaic devices with EQE values which clearly exceeded 100%, and maximum EQEs of 122%. Estimated IQE values were found to increase rapidly above $2E_g$, reaching values as high as 170% at only 3.5 E_g. This behavior is superior to that seen in solution-based measurements of MEG yields, and indicates potential for substantial efficiency gains in MEG-base solar cells.

6.1.2 Luminescent Solar Concentrators

LSCs containing three different oligofluorenes were fabricated with overall EQEs of $\approx$ 1.5 - 2.5 %. By simulating LSCs using Monte Carlo ray tracing we predicted that three new types of oligofluorene antenna complexes have large potential as the luminophore species used in LSCs. The reaction schemes for the synthesis of these molecules were also proposed.

6.1.3 Light-Emitting Diodes

We found that $CsPbCl_3$ and $CsPbI_3$ nanocrystals can exist as discrete entities in solution, embedded in a polymer matrix and as pure nanocrystal films. The $CsPbCl_3$ emission can be reabsorbed by the $CsPbI_3$ nanocrystals due to the large absorption coefficient of the $CsPbI_3$ nanocrystals in the range of the $CsPbCl_3$ emission. This phenomenon can be utilized in bulk heterojunction LEDs where the luminance of devices emitting in the 695 nm region can be improved by the incorporation of $CsPbCl_3$ nanocrystals. This causes the device to operate at a higher current density with emission transfer from the $CsPbCl_3$ nanocrystals to the $CsPbI_3$ crystal for efficient reemission

6.2 Concluding Remarks

Within this thesis various applications of spectral management in optoelectronic devices were discussed. These applications covered a broad area of research into renewable energy and lighting. The thesis looked specifically at three ways in which control of the absorbed and emitted photons could be used to improve PV, LSC and LED efficiencies. The field of optoelectronics is advancing fast, with improved understanding of the science of materials. Each year challenges in current generation materials are being solved and new materials are being developed. These new materials offer potential solutions to developing cheap and efficient sources of clean energy.